Nuclear Structure Studies near 208Pb and γ-ray Imaging Techniques

Lalovic, Natasa

2017

Citation for published version (APA):
Lalovic, N. (2017). *Nuclear Structure Studies near 208Pb and γ-ray Imaging Techniques*. [Doctoral Thesis (compilation), Faculty of Science]. Lund University, Faculty of Science, Department of Physics, Division of Nuclear Physics.

Total number of authors:
1

Nuclear Structure Studies near ^{208}Pb and γ-ray Imaging Techniques

NATAŠA LALOVIĆ

DEPARTMENT OF PHYSICS | FACULTY OF SCIENCE | LUND UNIVERSITY

Nuclear Structure Studies near ^{208}Pb and γ-ray Imaging Techniques

by Nataša Lalović

LUND UNIVERSITY

Dissertation for the degree of
Doctor of Philosophy

Thesis advisors: Prof. Dirk Rudolph,
Dr. Jürgen Gerl, Dr. Pavel Golubev

Faculty opponent: Dr. Roderick M. Clark

Academic dissertation which, by due permission of the Faculty of Science at Lund University, will be publicly defended on Wednesday, June 21st, 2017 at 13:15 in the Rydberg lecture hall (Rydbergsalen) at the Department of Physics, Sölvegatan 14A, Lund, for the degree of Doctor of Philosophy.

Organization
LUND UNIVERSITY

Department of Physics
Division of Nuclear Physics
Box 118, SE–221 00 LUND
Sweden

Document name
DOCTORAL DISSERTATION

Date of disputation
2017-21-06

Sponsoring organization

Author(s)
Nataša Lalović

Title
Nuclear Structure Studies near ^{208}Pb and γ-ray Imaging Techniques

Abstract

This thesis focuses on a high-resolution γ-ray spectroscopy experiment where the fragmentation of a ^{208}Pb primary beam was used to populate even-mass nuclei around ^{208}Pb. It was conducted in 2012 using the Advanced GAmma-ray Tracking Array (AGATA) while it was placed at GSI Darmstadt, Germany. Projectile-like fragments were selected and identified with the GSI Fragment Separator. The final aim is to study the aforementioned nuclei via Coulomb excitation. Yet, preceding measurements with stopped beams are necessary for reasons detailed here. Another part of this thesis is devoted to Research & Development (R&D) of position-sensitive scintillation detectors. These two different aspects are linked by studies of position sensitivity in devices utilized for detection of γ rays.
Advances in γ-ray tracking algorithms are essential for both applied and basic nuclear physics. Here, the scintillation detector R&D is foreseen to contribute to applications in the realm of medical imaging as well as environmental and safety surveillance, whereas the basic research efforts yield improved nuclear structure information on heavy ions produced in relativistic fragmentation reactions.
Paper I summarizes efforts regarding the image reconstruction algorithm when applied on a simulated data-set. In Paper II the performance of the AGATA sub-array is discussed, outlining the important aspects of the offline data processing and analysis. Paper III presents further treatment of the data partially scrutinized in Paper II using AGATA-tailored algorithms, assessing absolute efficiency and peak-to-total, and the performance of tracking algorithms with respect to different parameter-sets. Paper IV highlights an outstanding physics case from a stopped-beam AGATA measurement. In Paper V all aspects of the data analysis established in this thesis are described. The relevance of isomeric state measurements for both the experimental and theoretical aspect of relativistic fragmentation is emphasized.

Key words
nuclear structure, γ-ray spectroscopy, AGATA, isomeric decays, relativistic projectile fragmentation, Pb isotopes

Classification system and/or index terms (if any)

Supplementary bibliographical information

Language
English

ISSN and key title

ISBN
978-91-7753-287-3 (print)
978-91-7753-288-0 (pdf)

Recipient's notes

Number of pages
169

Price

Security classification

Distribution by Nataša Lalović, Division of Nuclear Physics, Lund University, Box 118, SE–221 00 LUND.

I, the undersigned, being the copyright owner of the abstract of the above-mentioned dissertation, hereby grant to all reference sources the permission to publish and disseminate the abstract of the above-mentioned dissertation.

Signature Lalović Nataša

Date 2017-05-16

Nuclear Structure Studies near ^{208}Pb and γ-ray Imaging Techniques

by Nataša Lalović

LUND
UNIVERSITY

Cover illustration front: Designed by Nataša Lalović. Shows AGATA configuration in 2014 as well as the γ-ray spectra resembling those from Paper V.

Faculty of Science, Department of Physics

ISBN: 978-91-7753-287-3 (print)
ISBN: 978-91-7753-288-0 (pdf)
LUNFD6 / (NFFR - 1040) / 1 - 85 (2017)

Printed in Sweden by Media-Tryck, Lund University, Lund 2017

Mojoj majci, Milici Lalović
Hvala za Sunce

Contents

List of publications and author's contributions

Paper I

Simulations for position-sensitive tracking of γ rays in scintillators: Approach for source reconstruction
GSI Scientific Report 2014 **2014-1**, 123 (2014).
N. Lalović, J. Gerl, D. Rudolph, R. Hoischen, and P. Golubev

I planned and wrote the simulations. I performed the data analysis, proposed the design for a first demonstrator to be built and wrote the report.

Paper II

Analysis of the Response of AGATA Detectors at GSI
EPJ Web of Conferences **93**, 07007 (2015).
N. Lalović, R. M. Perez-Vidal, C. Louchart, C. Michelagnoli, D. Ralet, T. Arici, D. Bazzacco, E. Clément, A. Gadea, J. Gerl, I. Kojouharov, A. Korichi, M. Labiche, J. Ljungvall, A. Lopez-Martens, J. Nyberg, N. Pietralla, S. Pietri, D. Rudolph, O. Stezowski, and the AGATA collaboration

I participated in planning, preparation and conducting the experiment. I performed preliminary data analysis focusing on AGATA-data processing and wrote the paper.

Paper III

Performance of the AGATA γ-ray spectrometer in the PreSPEC set-up at GSI
Nucl. Instr. Meth. Phys. Res. A **806**, 258 (2016).
N. Lalović, C.vLouchart, C. Michelagnoli, R. M. Perez-Vidal, D. Ralet, J. Gerl, D. Rudolph, T. Arici, D. Bazzacco, E. Clément, A. Gadea, I. Kojouharov, A. Korichi, M. Labiche, J. Ljungvall, A. Lopez-Martens, J. Nyberg, N. Pietralla, S. Pietri, O. Stezowski

My contribution to this paper was to participate in preparing and performing the experiment, to analyze the data by first establishing different ways of treating AGATA data and then assessing the AGATA-custom algorithms. I wrote the manuscript and took the main responsibility for editing the manuscript.

Paper IV

Role of the Δ Resonance in the Population of a Four-Nucleon State in the ^{56}Fe $\rightarrow^{54}$ Fe Reaction at Relativistic Energies
Phys. Rev. Lett. **117**, 222302 (2016).
Zs. Podolyák, C. M. Shand, **N. Lalović**, J. Gerl, D. Rudolph, T. Alexander, P. Boutachkov, M. L. Cortés, M. Górska, I. Kojouharov, N. Kurz, C. Louchart, E. Merchán, C. Michelagnoli, R. M. Pérez-Vidal, S. Pietri, D. Ralet, M. Reese, H. Schaffner, Ch. Stahl, H. Weick, F. Ameil, G. de Angelis, T. Arici, R. Carroll, Zs. Dombrádi, A. Gadea, P. Golubev, M. Lettmann, C. Lizarazo, J. Mahboub, H. Pai, Z. Patel, N. Pietralla, P. H. Regan, L. G. Sarmiento, O. Wieland, E. Wilson, B. Birkenbach, B. Bruyneel, I. Burrows, L. Charles, E. Clément, F. C. L. Crespi, D. M. Cullen, P. Désesquelles, J. Eberth, V. González, T. Habermann, L. Harkness-Brennan, H. Hess, D. S. Judson, A. Jungclaus, W. Korten, M. Labiche, A. Maj, D. Mengoni, D. R. Napoli, A. Pullia, B. Quintana, G. Rainovski, P. Reiter, M. D. Salsac, E. Sanchis, and J. J. Valiente Dóbon

My contribution to this paper was to participate in preparations (installation, maintenance of AGATA digitizers, setting up LYCCA and parts of AGATA electronics, pulser calibration of LYCCA prior to the experiment, setting up parts of both AGATA and FRS Data Acquisition), planning the part of the experiment related to the source measurements and performance (AGATA data treatment, nearline and preliminary data analysis, see Papers II and III) of the experiment. I performed the efficiency analysis for this stopped-beam configuration, both based on the source measurements and isomeric yields and wrote parts of the manuscript.

Paper V

Study of Isomeric States in ^{198,200,202,206}Pb and ^{206}Hg Populated in Fragmentation Reactions
J. Phys. G: Nucl. Part. Phys., to be submitted
N. Lalović, D. Rudolph, Zs. Podolyák, L. G. Sarmiento, E. C. Simpson, T. Alexander, M. L Cortés, J. Gerl, P. Golubev, F. Ameil, T. Arici, Ch. Bauer, D. Bazzacco, M. A. Bentley, P. Boutachkov, M. Bowry, C. Fahlander, A. Gadea, J. Gellanki, A. Givechev, N. Goel, M. Górska, A. Gottardo, E. Gregor, G. Guastalla, T. Habermann, M. Hackstein, A. Jungclaus, I. Kojouharov, S. Kumar, N. Kurz, M. Lettmann, C. Lizarazo, C. Louchart, E. Merchán, C. Michelagnoli, Th. Moeller, K. Moschner, Z. Patel, N. Pietralla, S. Pietri, D. Ralet, M. Reese, P. H. Regan, P. Reiter, H. Schaffner, P. Singh, C. Stahl, R. Stegmann, O. Stezowski, J. Taprogge,

P. Thöle, A. Wendt, O. Wieland, E. Wilson, R. Wood, H.-J. Wollersheim and the AGATA Collaboration

My contribution to this paper was to participate in preparations of the experiment: installation, setting up AGATA electronics for the first physics campaign at GSI alongside the adjustments in signal-processing software and performing AGATA energy calibrations prior to the experiment. The analysis I performed was multi-folded, regarding both the half-life determination as well as the extraction of isomeric ratios. Moreover, it relies on the analysis I did earlier and reported in Papers II-IV. Finally, I developed a compact analysis routine which is easily applicable to all stopped-beam experiments facilitating isomeric states. I wrote parts of the manuscript and I am responsible for communicating it to the journal. Due to the publication policy defined within the AGATA Collaboration, submission of the manuscript in its form approved by all the coauthors would require several week-long time for the official Collaboration approval. Therefore, the paper is attached as a manuscript here.

Publications not included in this thesis

Lifetime measurement of neutron-rich even-even molybdenum isotopes
Phys. Rev. C **95** 034320 (2017).
D. Ralet, S. Pietri, T. Rodríguez, M. Alaqeel, T. Alexer, N. Alkhomashi, F. Ameil, T. Arici, A. Ataç, R. Avigo, T. Bäck, D. Bazzacco, B. Birkenbach, P. Boutachkov, B. Bruyneel, A. M. Bruce, F. Camera, B. Cederwall, S. Ceruti, E. Clément, M. L. Cortés, D. Curien, G. De Angelis, P. Désesquelles, M. Dewald, F. Didierjean, C. Domingo-Pardo, M. Doncel, G. Duchêne, J. Eberth, A. Gadea, J. Gerl, F. Ghazi Moradi, H. Geissel, T. Goigoux, N. Goel, P. Golubev, V. González, M. Górska, A. Gottardo, E. Gregor, G. Guastalla, A. Givechev, T. Habermann, M. Hackstein, L. Harkness-Brennan, G. Henning, H. Hess, T. Hüyük, J. Jolie, D. S. Judson, A. Jungclaus, R. Knoebel, I. Kojouharov, A. Korichi, W. Korten, N. Kurz, M. Labiche, **N. Lalović**, C. Louchart-Henning, D. Mengoni, E. Merchán, B. Million, A. I. Morales, D. Napoli, F. Naqvi, J. Nyberg, N. Pietralla, Zs. Podolyák, A. Pullia, A. Prochazka, B. Quintana, G. Rainovski, M. Reese, F. Recchia, P. Reiter, D. Rudolph, M. D. Salsac, E. Sanchis, L. G. Sarmiento, H. Schaffner, C. Scheidenberger, L. Sengele, B. S. Nara Singh, P. P. Singh, C. Stahl, O. Stezowski, P. Thoele, J. J. Valiente Dobon, H. Weick, A. Wendt, O. Wiel, J. S. Winfield, H. J. Wollersheim and M. Zielinska

High-precision mass measurements for the isobaric multiplet mass equation at A = 52
J. Phys. G: Nucl. Part. Phys. **95** 034320 (2017).
D. A. Nesterenko, A. Kankainen, L. Canete, M. Block, D. Cox, T. Eronen, C. Fahlander, U. Forsberg, J. Gerl, P. Golubev, J. Hakala, A. Jokinen, V. S. Kolhinen, J. Koponen, **N. Lalović**, Ch. Lorenz, I. D. Moore, P. Papadakis, J. Reinikainen, S. Rinta-Antila, D. Rudolph, L. G. Sarmiento, A. Voss and J. Äystö

Conceptual design of the AGATA 1π array at GANIL
Nucl. Instr. Meth. Phys. Res. A **855** 1 (2017).
E. Clément, C. Michelagnoli, G. de France, H. J. Li, A. Lemasson, C. Barthe Dejean, M. Beuzard, P. Bougault, J. Cacitti, J.-L. Foucher, G. Fremont, P. Gangnant, J. Goupil, C. Houarner, M. Jean, A. Lefevre, L. Legeard, F. Legruel, C. Maugeais, L. Ménager, N. Ménard, H. Munoz, M. Ozille, B. Raine, J. A. Ropert, F. Saillant, C. Spitaels, M. Tripon, Ph. Vallerand, G. Voltolini, W. Korten, M.-D. Salsac, Ch. Theisen, M. Zielińska, T. Joannem, M. Karolak, M. Kebbiri, A. Lotode, R. Touzery, Ch. Walter, A. Korichi, J. Ljungvall, A. Lopez-Martens, D. Ralet, N. Dosme, X. Grave, N. Karkour, X. Lafay, E. Legay, I. Kojouharov,

C. Domingo-Pardo, A. Gadea, R. M. Perez-Vidal, J. V. Civera, B. Birkenbach, J. Eberth, H. Hess, L. Lewandowski, P. Reiter, A. Nannini, G. de Angelis, G. Jaworski, P. R. John, D. R. Napoli, J. J. Valiente-Dobón, D. Barrientos, D. Bortolato, G. Benzoni, A Bracco, S. Brambilla, F. Camera, F. C. L. Crespi, S. Leoni, B. Million, A. Pullia, O. Wieland, D. Bazzacco, S. M. Lenzi, S. Lunardi, R. Menegazzo, D. Mengoni, F. Recchia, M. Bellato, R. Isocrate, F. J. Egea Canet, F. Didierjean, G. Duchêne, R. Baumann, M. Brucker, E. Dangelser, M. Filliger, H. Friedmann, G. Gaudiot, J.-N. Grapton, H. Kocher, C. Mathieu, M.-H. Sigward, D. Thomas, S. Veeramootoo, J. Dudouet, O. Stezowski, C. Aufranc, Y. Aubert, M. Labiche, J. Simpson, I. Burrows, P. J. Coleman-Smith, A. Grant, I. H. Lazarus, P. S. Morrall, V. F. E. Pucknell, A. J. Boston, D. S. Judson, **N. Lalović**, J. Nyberg, J. Collado, V. González, I. Kuti, B. M. Nyakó, A. Maj, M. Rudigier

Characterization of a gamma-ray tracking array: A comparison of GRETINA and Gammasphere using a ^{60}Co source
Nucl. Instr. Meth. Phys. Res. A **836** 46 (2016).
T. Lauritsen, A. Korichi, S. Zhu, A. N. Wilson, D. Weisshaar, J. Dudouet, A. D. Ayangeakaa, M. P. Carpenter, C. M. Campbell, E. Clément, H. L. Crawford, M. Cromaz, P. Fallon, J. P. Greene, R. V. F. Janssens, T. L. Khoo, **N. Lalović**, I. Y. Lee, A. O. Macchiavelli, R. M. Perez-Vidal, S. Pietri, D. C. Radford, D. Ralet, L. A. Riley, D. Seweryniak, and O. Stezowski

Isomeric Ratios in ^{206}Hg
Acta Phys. Pol. **46** 601 (2015).
T. Alexander, Zs. Podolyák, M.L. Cortés, J. Gerl, D. Rudolph, L.G. Sarmiento, F. Ameil, T. Arici, D. Bazzacco, Ch. Bauer, M.A. Bentley, P. Boutachkov, R. Caroll, C. Fahlander, A. Gadea, J. Gellanki, W. Gelletly, A. Givechev, N. Goel, P. Golubev, M. Górska, A. Gottardo, E. Gregor, G. Guastalla, T. Habermann, M. Hackstein, A. Jungclaus, I. Kojouharov, W. Korten, S. Kumar, N. Kurz, **N. Lalović**, M. Lettmann, C. Lizarazo, C. Louchart, S. Mandal, E. Merchán, C. Michelagnoli, Th. Moeller, K. Moschner, Z. Patel, N. Pietralla, S. Pietri, D. Ralet, M. Reese, P.H. Regan, P. Reiter, H. Schaffner, P. Singh, Ch. Stahl, R. Stegmann, O. Stezowski, J. Taprogge, P. Thoele, P.M. Walker, O. Wieland, A. Wendt, E. Wilson, R. Wood, and H.-J.Wollersheim

Analysis and Results of the the ^{104}Sn Coulomb Excitation Experiment
Journal of Physics: Conference Series **533** 012047 (2014).
G. Guastalla, Douglas Di Julio, M. Górska, J. Cederkäll, P. Boutachkov, P. Golubev, S. Pietri, H. Grawe, F. Nowacki, A. Algora, F. Ameil, T. Arici, A. Ataç, M. A. Bentley, A. Blazhev, D. Bloor, S. Brambilla, N. Braun, F. Camera,

C. Domingo-Pardo, A. Estrade, F. Farinon, J. Gerl, N. Goel, J. Grębosz, T. Habermann, R. Hoischen, K. Jansson, J. Jolie, A. Jungclaus, I. Kojouharov, R. Knoebel, S. Kumar, J. Kurcewicz, N. Kurz, **N. Lalović**, E. Merchán, K. Moschner, F. Naqvi, B. S. Nara Singh, J. Nyberg, C. Nociforo, A. Obertelli, M. Pfützner, N. Pietralla, Zs. Podolyák, A. Prochazka, D. Ralet, P. Reiter, D. Rudolph, H. Schaffner, F. Shirru, L. Scruton, T. Swaleh, J. Taprogge, R. Wadsworth, N. Warr, H. Weick, A. Wendt, O. Wieland, J. S. Winfield, and H.-J. Wollersheim

Coulomb Excitation of ^{104}Sn and the Strength of the ^{100}Sn Shell Closure

Phys. Rev. Lett. **110**, 172501 (2013).

G. Guastalla, Douglas Di Julio, M. Górska, J. Cederkäll, P. Boutachkov, P. Golubev, S. Pietri, H. Grawe, F. Nowacki, K. Sieja, A. Algora, F. Ameil, T. Arici, A. Ataç, M. A. Bentley, A. Blazhev, D. Bloor, S. Brambilla, N. Braun, F. Camera, Zs. Dombrádi, C. Domingo-Pardo, A. Estrade, F. Farinon, J. Gerl, N. Goel, J. Grębosz, T. Habermann, R. Hoischen, K. Jansson, J. Jolie, A. Jungclaus, I. Kojouharov, R. Knoebel, S. Kumar, J. Kurcewicz, N. Kurz, **N. Lalović**, E. Merchán, K. Moschner, F. Naqvi, B. S. Nara Singh, J. Nyberg, C. Nociforo, A. Obertelli, M. Pfützner, N. Pietralla, Zs. Podolyák, A. Prochazka, D. Ralet, P. Reiter, D. Rudolph, H. Schaffner, F. Shirru, L. Scruton, D. Sohler, T. Swaleh, J. Taprogge, Zs. Vajta, R. Wadsworth, N. Warr, H. Weick, P. Thoele, A. Wendt, O. Wieland, J. S. Winfield, and H.-J. Wollersheim

A method to estimate a contribution of Ge(n,n') reaction to the low-energy part of gamma spectra of HPGe detectors

Nucl. Instr. Meth. Phys. Res. A **709**, 8 (2013).

M. Krmar, J. Hansman, N. Jovančević, **N. Lalović**, J. Slivka, D. Joković and D. Maletić

Acknowledgements

Thinking of the thesis work as a reason to celebrate oneself, in what already feels as a climate of acute lack of empathy, would be so very ungrateful, to say the least. That does not go without saying that how the results of my PhD studies have been achieved and formulated is truly my responsibility. Yet, there are so many individuals to whom I owe so much.

Dirk. Thank you for your guidance. Thank you for never failing to align and re-focus my execution of data tasks with the actual goal of this exercise. When many would argue about the relevance of the data and (un)intentionally almost deprive yet another student of the needed motivation, your persuasive points would inspire that student to an immediate action. Your support in all things inevitable administration was, and still is, instrumental.

Jürgen. Thank you for inviting me to be a part of the Gamma Spectroscopy Group at GSI. Thank you for all the useful discussions during my stay at GSI, as well as for being my co-supervisor even when I moved to Lund.

Pavel. Thank you for your willingness to answer all my scintillator-related questions. Thank you for your comprehensive explanations that would actually leave me thinking 'I got this. Let's build it!'.

I am so very grateful to all members of Nuclear Structure Group in Lund. Performing experiments with you was really a pleasure.

Pico, your actions on data-analysis merging software were immensely helpful. And not to forget such a great job you did with cleaning the FRS data. It was so pleasant to simply 'get on board' once the things were working. Thank you!

Ulrika, thank you for your understanding and support! Be it preventing homelessness, or 'just' knowing how during/after long beam times and Thesis writing feels, your help is very much appreciated.

Working with the detector such as AGATA on a daily basis is overwhelming at times, but absolutely amazing. I would not go as far as saying that one (read: myself) identifies with it, but being the only of the kind on the continent does mold your experimental knowledge greatly and puts a bias on your perspective of the field. And it does so, in my humble opinion, in a very positive way. Working with it is equivalent to collaborating with many skilled researchers distributed around the world.

Zsolt. Thank you for answering my countless questions about both S429 and S429_2 and for clarifying the potential of our stopped-beam data. Thank you for being such a great spokesperson, your enthusiasm and patience are always inspiring.

I would like to thank my GSI Summer Student Program mentor, Stephane, for introducing me to AGATA. Thank you for your numerous explanations and including me in the setting up of the AGATA challenging electronics from its

earliest days at GSI.

Special gratitude goes to all the co-authors of Paper III. During our frequent meetings, many more things than those formulated in the Paper were discussed and clarified. I would particularly like to thank the following colleagues, regardless if we are co-authors or not:

Dino. Thank you for sharing your expertise with me. You were so patient with all my assertive questions. My trips to Legnaro were just wonderful.

Waely. Thank you for always being so close to data. Thank you for making me realize how important it is to articulate and ask out loud even the questions that might sound simple to oneself.

Joa. Thank you for always formulating complex aspects in a comprehensible manner. Even very short discussions with you and Waely always make my work more effective.

Caterina. Thank you for, as you sometimes say, being my teacher. You introduced me to AGATA data processing and made me realize how much I like it. Especially when I really see the intended effects.

Corinne. Working with you was so easy. Thank you for your friendship and support.

Olivier. You were so helpful and responsive in data-analysis-software times that seemed so cataclysmic. Thank you so much for everything I learned about GammaWare and ADF.

Andrés. Your positive attitude toward AGATA is contagious. Thank you for all the valuable comments and for nice discussions during various beam times.

Francesco. Thank you for reading the manuscript of Paper III so carefully. Thank you for your excellently formulated questions I learned so much from.

Frederic. You were always so supportive. Thank you for sharing your deep knowledge of the system and for countless coffee breaks and contemplations.

Maria. Our imaging discussions were so constructive. Thank you!

Thank you to my AGATA-PhD-fellow students and friends from various places: Alberto, Riccardo, Rosa, Tayfun, Cesar.

Damian and Giulia. You fall under all of the categories above. You have guided me through my first months as a PhD student and you were the best office mate and the neighbouring-office mate, respectively. Thank you!

I would also like to express my sincere gratitude to the following members of the Division of Nuclear Physics:

Anneli. You took care of everything to make my transition to Lund smooth. Thank you so much!

Charlotta. Thank you for making the teaching experience in Lund so organized. The conversations with you on various subjects were always so comforting.

Yulia. Thank you for your help with all administrative tasks.

Finally..

Jedno veliko hvala:

Mojim divnim prijateljima što nisu dozvolili da usled stalnih promjena mjesta boravišta zaboravimo.

Mom vjereniku Christianu, čiju podršku jedino prevazilazi njegovo istinsko poimanje gradijenta pravca jug(oistok) - sjever(ozapad), kao i posledice koje isti ima na čovječanstvo. A i na dva nomada nejasne svijesti pripadanja. Hvala što si svojim sjajnim algoritamskim pristupom dao značajan doprinos Knjizi Ideja.

Mom tati Milisavu. Ti si jedan od rijetkih pravih intelektualaca koje znam i na kog sam se uvijek ugledala. Nevjerovatno je kako si uvijek umio da usmjeriš moja interesovanja naklonjena misaonom udubljivanju. Mojoj sestri Mirjani. Tvoja posvećenost se nikada ne dovodi u pitanje. Tvojoj (i mojoj) porodici, Danilu, Žarku i Relji... I kad sam mislila da dobro znam kako savršena budu naša ljeta na pravim planinama, pojaviste se vi. Mojoj majci Milici. Ti zaista razumiješ sve. Beskrajno ti hvala na strpljenju sa nama troma i nekada napornom posvećenošću akademskom svijetu. Tvoja kreativnost i logika stimulišu i dobro znaš da nema fraze koja u potpunosti artikuliše moja osjećanja i zahvalnost.

(Thank You:

My amazing friends who did not let our constant relocations make us forget.

My fiancé Christian, whose support is outdone (only) by his fundamental understanding of the south(east)-north(west) gradient and its consequences on humanity. And on a couple of nomads' blurred sense of belonging for that matter. Thank you for your brilliant algorithmic thinking input to the Book of Ideas.

My father Milisav. You are that one of a few intellectuals I know and I've always looked up to. I am so grateful that you were always helping me channel my contemplation-prone interests. My sister Mirjana, because your dedication is unquestionable. And your (and mine) family, Danilo, Žarko and Relja... I thought I knew how amazing our summers in the 'real mountains' get to be, and then you guys appeared. My mother Milica, who really understands everything and puts up with the (sometimes) academia-centred views of the rest of us. Your creativity and logic are stimulating. You know that no phrase can truly embody my emotions and gratefulness.)

Populärvetenskaplig sammanfattning

AGATA är en speciell positionskänslig detektor för gammastrålning. Genom att använda en sådan detektor är det möjligt att rekonstruera den väg som gammastrålningen tar genom detektorn. Det garanterar en mycket högre känslighet för detektion av gamma strålning än vad var möjlig för tidigare typer av detektorer. Detta betyder att vi kan få tillgång till mycket mer information om atomkärnan än vad vi kunde tidigare. Men det är inte bara 'kunskap för kunskapens egen skull' (analog med *l'art pour l'art*) som vi är efter. Detektorer som använder denna teknik är av stor betydelse inom tillämpad kärnfysik och andra olika områden som använder gammastrålning. Några av dessa är biofysik, kärnmedicin och säkerhetskontroller.

I detta arbete förklarar jag vilka ingredienser som behövs för att förstå data som samlats in med en komplex detektor som AGATA. Detta arbete avser den unika kombination av AGATA och flera andra detektorer, som användes när AGATA var belägen vid det tyska laboratoriet GSI i Darmstadt. AGATA är en av två detektorer av det slaget, och GSI är än så länge den enda platsen i världen där man kan producera de partiklar vid de energier som behövs för experimentet som beskrivs i detta arbete. Jag har genom mitt doktorsarbete gradvis kommit fram till den punkt där de data vi samlade in och analyserade är viktiga för de teoretiska modeller som försöker förklara komplexiteten hos atomkärnan.

Självklart hoppas jag att detta bidrag skulle kunna hjälpa till att svara på mycket viktiga frågor inom grundläggande kärnfysik. Men 'vad tjänar jag och alla andra på det...' frågar du kanske. Jag hoppas att jag med denna avhandling kan övertyga dig om att de metoder och algoritmer som säkerställer AGATA möjlighet att spåra gammastrålning faktiskt är relevanta för de tillämpade områden som jag listade ovan. Det är därför som det här arbetet också tar upp möjligheten att observera objekt som är dolda för våra ögon, genom att använda gammastrålning och gammadetektorer Dessutom föreslår jag en enkel apparat som kan fungera som en laboratorieprototyp för att testa vad vi hittills har hittat.

Chapter 1

Introduction

In the realm of fundamental nuclear physics various phenomena of *atomic nuclei*, complex many-body systems of quantum mechanical origin, have been experimentally observed. These comprise different shapes of nuclei, tests of their stability upon the change of nucleon numbers, their seemingly conflicting single-particle and collective nature, to name but a few [1]. Certain theoretical models have made considerable success in explaining many of such phenomena. However, it is very challenging to frame such examples of excellent agreement between experiment and theory as one fundamental overarching nuclear-structure theory which holds true for all aspects of all nuclei. Therefore, experimental data are a valuable input to 'gauge' models for specific regions on the chart of nuclides and essentially to confine, and thus improve, them further.

This work is to provide more information about the direct neighbourhood of the heaviest stable doubly-magic nucleus, ^{208}Pb. Figure 1.1 shows an overview of where in the nuclear chart the nuclei of increased stability (magic nuclei) are positioned.

This nucleus represents one of the doubly-magic cornerstones on the nuclear chart. Moreover, even-even nuclei and their basic properties, the excitation energy of the first $I^{\pi} = 2^{+}$ state, $E_x(2^+)$, and reduced transition strengths between this state and the 0^+ ground state, $B(E2; 2^+ \rightarrow 0^+)$, are recognized as key quantities in nuclear structure physics. Surprisingly, many of these observables are not reliably known in the region of interest around ^{208}Pb. It is an objective of this work to prove that in order to attain the missing experimental input, more comprehensive information about isomeric states is required as well. These isomeric states are also called *metastable* states, for they have significantly longer half-lives and different nuclear properties than other states in the same nucleus [2].

The nuclear reaction scrutinized for the measurement presented in this work is relativistic projectile fragmentation. A primary beam of high energy focussed onto a primary target ensures that the projectile particles have energies far above the Coulomb barrier, allowing the projectile to penetrate target nuclei [1]. Then, a cocktail of reaction products is filtered by means of a series of magnets of the magnetic separator - Fragment Separator (FRS) [4], to select the secondary beam of one species. In this way, a radioactive beam is directed towards the secondary target. At this stage the intended secondary reaction occurs.

Finally, γ-ray spectroscopy is the tool chosen to assess the missing information mentioned earlier. By surrounding the secondary target chamber by an array of germanium crystals, γ rays stemming from the nuclei of interest are detected, allowing a multi-parameter correlation analysis to confirm their origin. In all experiments discussed in the present work, the Advanced GAmma Tracking Array (AGATA) [5] was used within the PreSPEC-AGATA experimental campaign [6].

Having in mind the complexity of AGATA data processing and analysis, a need

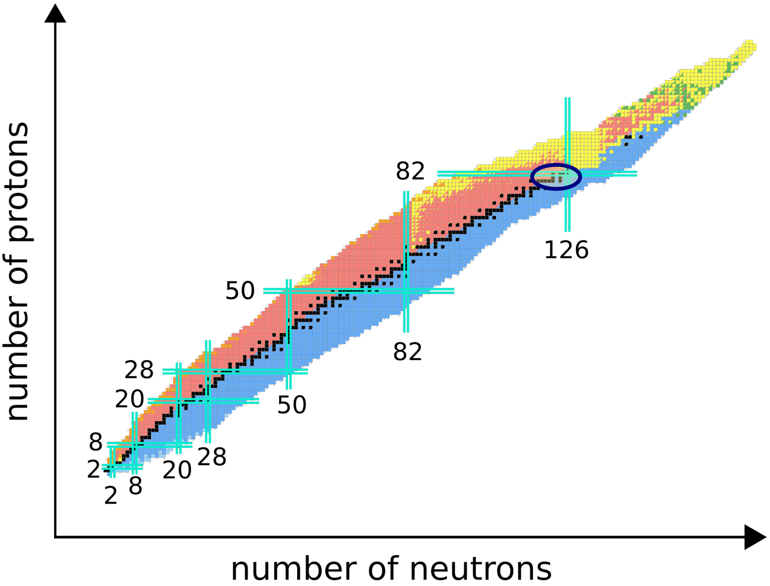

Figure 1.1: Nuclear chart with proton number (Z) plotted against the neutron number (N) for all known chemical elements as of the 2012 evaluation of nuclear properties [3]. The lines in cyan indicate the locations of the magic numbers 2, 8, 20, 28, 50, 82, and 126. Black squares correspond to the stable nuclei. The blocks where these lines for protons and neutrons intersect represent the nuclei comprised of a magic number of both protons and neutrons, i.e. *doubly-magic* nuclei. The encircled region highlights the nuclei which are of relevance to the current study.

for a careful assessment of different data-analysis modes and AGATA-tailored algorithms was recognized. Therefore, a series of calibration runs yielded a consolidated treatment of the data taken with the AGATA sub-array within the PreSPEC set-up. This facilitated the subsequent analysis of isomeric states. The AGATA data collected upon stopping the beam at the place of the secondary target can be coupled to the FRS data in a less complicated manner.

Despite the fact that the isomeric states populated in this work are known, the observable *isomeric ratio* has been deduced for the first time for a number of Pb isotopes. The isomeric ratios describe the fraction of the secondary beam populated in a particular isomeric state during the primary production reaction. This information is absolutely essential for the observables acquired in in-beam γ-ray spectroscopy via Coulomb excitation. For instance, when studying the low-lying states in even-even nuclei, one is often interested in the electromagnetic excitation from the ground state into the first excited 2^+ state. Figure 1.2 shows a schematic illustration of this process. It is thus necessary to account for the beam component populated in isomeric states, as that portion calculated via isomeric ratios prohibits the nucleus to be excited from the ground state.

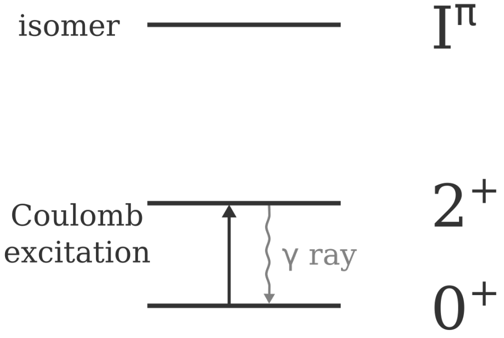

Figure 1.2: Schematic drawing of the electromagnetic excitation (referred to as a 'Coulomb excitation') from the ground state, 0^+ into the first excited state, 2^+. Once the excited state is populated, it is expected to decay back to the ground state by emitting a γ ray, denoted on the illustration. Another excited state is drawn and marked as 'isomer'. Its γ decay is inhibited and is therefore characterized by a relatively long half-life [2].

The importance of the deduced isomeric ratios is not only that spectroscopic information can be precisely normalized, but that nuclear reaction theory can be tested on these experimental examples. The technique presented in this work provides insight in the longitudinal projectile momentum distribution, which (when interpreted within the theoretical formalism [7]), serves as an estimate of the orbital angular momentum of the removed nucleon. A simplified schematic drawing of a two-nucleon removal is shown in Figure 1.3.

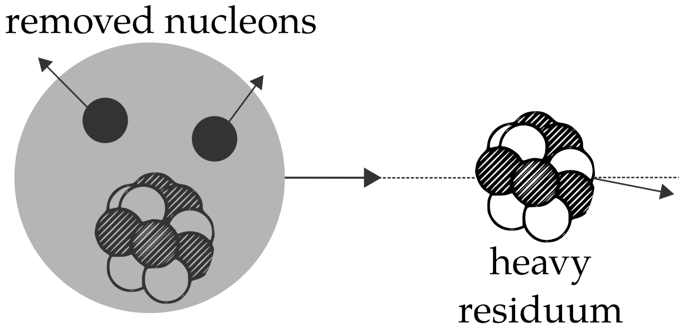

Figure 1.3: Illustration of the simplest case of the multi-nucleon removal considered in the current work. The region marked in grey encompasses the projectile, i.e. two removed neutrons and the residue. The longitudinal momentum is of relevance here, thus it is indicated by an arrow in the direction of the projectile. Adapted from [8].

Another part of the present work is related to the imaging capability of γ radiation detectors. This topic might seem unrelated to the aspects of nuclear-structure studies presented in the rest of this work. Yet, both projects rely on position-sensitive devices utilized for detection of γ rays and the techniques derived from this property, namely γ-ray tracking and imaging algorithms. Therefore, the growing demand for detection schemes with such capabilities is not relevant only for the basic research sector, but even more in societal and industrial applications, such as medical imaging, environmental and safety investigations. For example, in cancer imaging applications a positron emission tomography (PET) camera proved to have unprecedented detection capability. Nevertheless, there are more and more techniques emerging in the field of both imaging and therapy, often making use of ion beams instead of conventional radiation. Both face open questions, for instance regarding radiation interacting with moving tissues, which greatly complicates exact treatment planning. It is very difficult to ensure precise enough position measurement which affects radiation treatment delivery. Therefore, the detectors used need to be understood and knowing their response is an absolute requirement. A convenient way to investigate this thoroughly is by simulating the response of the detectors. In Chapter 7 the underlying scattering principle is briefly presented. This is then applied to the particular detection schemes developed for the study described here. Finally, the Chapter ends with an outline for future experimental tests.

As stated, the main part of this Thesis is related to the PreSPEC-AGATA experimental campaign and its results. This can be inferred from the research output regarding this project, too (see Papers II-V).

The experimental set-up, the relevant observables and details of the experiments performed and analyzed in the course of this work are discussed in Chapters 2 and 3. Chapter 4 provides insight into data analysis routines followed, emphasizing details of AGATA data treatment and corrections. In addition, different analysis steps needed to deduce isomeric ratios are clarified through one example nucleus, followed by the results of the same routine when applied to all Pb isotopes. A theoretical aspect of nuclear structure in Pb isotopes is considered in Chapter 5. First, the adequate model is introduced, followed by the explanation of how its ingredients were adjusted for the particular case presented here. Finally, the results are shown and the agreement obtained with the experiment is investigated in Paper V.

Chapter 2

The PreSPEC-AGATA Set-up

Most of the requirements for performing high-resolution γ-ray spectroscopy with radioactive ion beams at GSI, Darmstadt were met through the ensemble of detector elements or arrays known as the PreSPEC-AGATA set-up [6]. Ion production and identification is ensured by the FRagment Separator (FRS) detectors [4]. The γ-spectroscopy data is collected by the state-of-the-art Advanced GAmma Tracking Array (AGATA) [5], presently employed as a sub-array, and the High Energy γ-ray deteCTOR (HECTOR+) [9]. The residual fragments after the secondary target are identified by the Lund-York-Cologne CAlorimeter (LYCCA) [10].

2.1 The Fragment Separator

Relativistic ion beams are produced by the GSI accelerator complex (UNILAC and SIS-18) [11, 12] and delivered to the entrance of the FRS. This part of the magnetic separator is known as the target area, since the primary target chosen for a particular reaction is placed here. Then, the beam passes through four sections of the FRS (i.e. *focal planes*) each comprising a number of ion-optical elements to select the reaction products of interest and focus them further. The final focal plane, S4, incorporates the PreSPEC-AGATA detector set-up in addition to the FRS detectors essential for the correlation of the selected ions with the products of the secondary nuclear reaction or implantation. Chapter 2.1.1 provides more details. In addition to those situated in the final focal plane, there is a number of FRS detection elements placed in the second focal plane, S2, which are essential for the experiment, hence for the analysis presented in this work, too. The detailed explanation of all FRS components and working principle goes beyond the scope of this thesis. Observables used in the current analysis (see Section 4 for more details) are presented, alongside respective detectors producing the signals. A schematic overview of the FRS is shown in Figure 2.1.

2.1.1 Components Relevant for the Present Analysis

Accentuated regions of Figure 2.1 refer to the middle and the final focal plane of the FRS, seen downstream along the beamline:

- The **S2 section** contains the following elements: pairs of thick metal blocks, *slits*, to restrict the maximum beam width and thus its content by adjusting their position across the x- and y-plane (the measurement presented here made use of the x-plane slits only); two scintillation detectors, the SC21 used in the time of flight (TOF) measurements and the segmented plastic scintillator, SC22, i.e. *finger* detector, for TOF measurements at higher rates [13, 14]; the two scintillators are kept apart by a

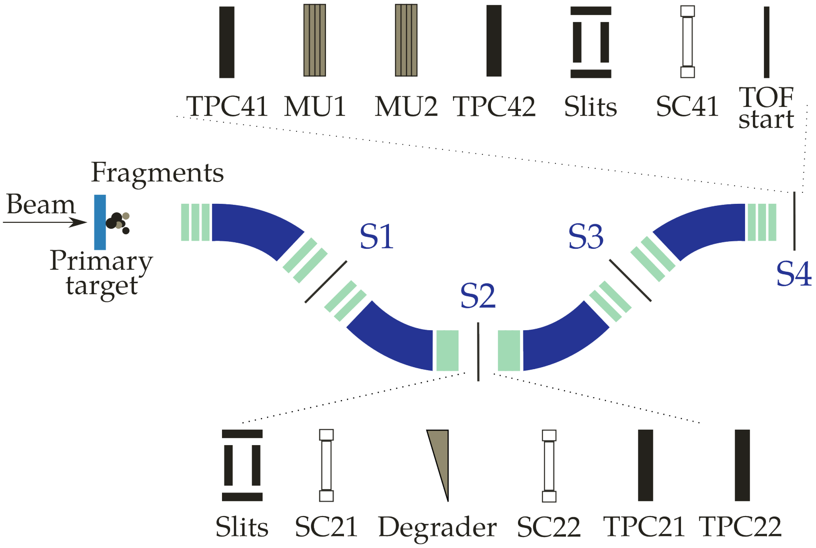

Figure 2.1: Schematic overview of the FRS detector arrangement as deployed in the S429 experiment. Focal planes are labelled S1 - S4 following the beam from the primary target towards the area of the final focal plane where AGATA was situated. The two highlighted regions show all FRS detectors placed in the middle and final focal plane, respectively, needed for detection and identification of ions. The two MUSIC detectors situated in the S4 region are labelled as MU1 and MU2. FRS optical elements are not labelled and are presented as bulk elements coloured in two shades of blue.

wedge-shaped degrader which separates different beam particles depending on their energy loss in its varying-thickness medium; two Time Proportional Chambers (TPC) [15], TPC21 and TPC22, used for position determination and tracking of the incoming ions.

- The **S4 section's** detector arrangement used for particle identification is detailed in Figure 2.1. Several detection element are of the same type as those used in S2: two TPCs (TPC41 and TPC42), and a scintillator SC41. Additionally, there are two MUlti Sampling Ionisation Chambers (MUSIC) [16] for ion's charge or proton number, Z, determination. The last element placed in front of the secondary target chamber (Figure 2.2) is a plastic scintillator detector, *TOF Start*. This gives the first of up to three timing signals needed for the TOF measurement of LYCCA [10, 17].

- The **vacuum chamber** for the secondary target is placed in the S4 area. The arrangement of its elements is subject to change at different stages of the experiment. To ease the discussion it is presented as a separate unity and its schematic overview is shown in Figure 2.2. It entails a 'Target TOF' plastic scintillator, which is a smaller version of the *TOF Start* scintillator [10]. A position sensitive, 0.31 mm thick Double-Sided-Silicon-Strip Detector (DSSSD) is used to determine the interaction position of the beam on the secondary target. Finally, the secondary target could be placed either at the central, *nominal* distance of 23.5 cm from the centre of AGATA or at the *forward* position, 15.0 cm closer to the centre of the array. In Section 3.1 the use of each position is clarified further.

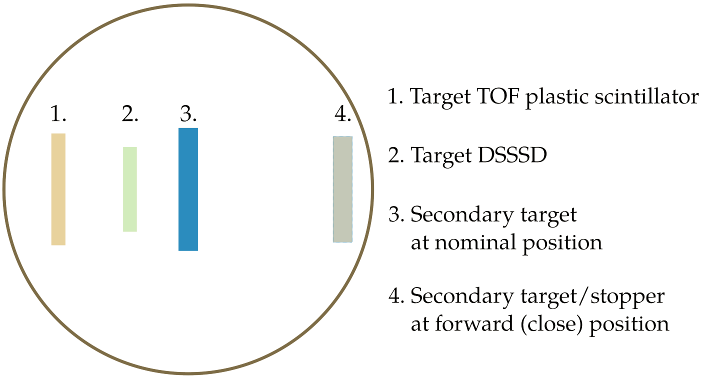

Figure 2.2: Target chamber in the beamline at the final focal plane. The FRS detectors are not shown. Distances between the elements are to scale.

With the detection elements in respective areas explained above, the following list provides an overview of physical observables extracted from those, essential for the analysis of the currently discussed experiment:

- **TPCs in the S2 section** were used in tracking of the ions, precisely in determining the x-position.
- **SC21** provided the *start* signal for the TOF between the S2 and S4 areas.
- **MUSICs in the S4 section** recorded energy loss of fragments, which was then transformed to the Z value of fully stripped ions.
- **SC41** provided the *stop* signal for the TOF measurement. This value was then used to determine the velocity of ions, $\beta = v/c$, between S2 and S4.
- **Target DSSSD** energy loss information (see Figure 2.2) and the one from MUSICs (from the S4 area) were used to select the correct Z value of the ions which would then impinge onto the secondary target or the passive stopper. In this way, any potential losses of ions along the flight path were accounted for.

2.1.2 Simulations

A virtual model of the FRS is featured in the LISE++ simulation package [18]. LISE++ details the beam transportation, reaction mechanism and energy loss of beam particles traversing different materials. In addition to such an implementation, experiment-tailored parameters regarding the FRS ion optics were included to predict production and transport yields for the fragments of interest and unwanted contaminants. It is important to note that very thorough Monte Carlo transmission analyses could be done for each element present in the set-up. This was decisive for isomeric ratio calculation and precise number of ions implanted in the plastic stopper. See Sections 4.3.2 and 4.3.3 for the calculation-specific explanations.

2.2 γ-ray Spectrometer

The foundation of superior AGATA performance in comparison to its predecessors germanium detector arrays lies in the possibility to extract both spatial- and energy information for a single γ-ray interaction. To begin with, it is necessary to access these two pieces of information in order to realize the concept of γ-ray tracking. There are two different approaches to the development of the tracking algorithm. Paper III outlines these two different approaches and arguments to utilize the forward-tracking routine in this work. The same article depicts a retrospective of large γ-ray detector arrays. Therefore, only those aspects exploited in the current analysis or essential for its interpretation, are pointed out here.

The composite detector arrays [19–21] ensured improvements in size of germanium crystals used and higher granularity as opposed to the conventional arrays comprising single germanium crystals. An additional improvement is made in terms of data treatment owing to the 'add-back' approach. The reader is referred to Section 4.2.4 for a concise explanation of this concept.

In experiments with beam particles moving at relativistic velocities, the Doppler effect greatly affects the sensitivity of the spectrometer. Due to the finite opening angle of the detector, the spread in energy on the recorded spectrum is apparent. As a consequence, the energy resolution, which is one of the decisive features of these arrays, is compromised. Therefore, a key for the present generation of large γ-ray arrays is the increase of granularity by means of additional contact segmentation [22, 23]. Besides, the segmentation introduced the idea of position-sensitive Ge detectors.

In order to operate AGATA in the position-sensitive mode, the main requirements are electrical segmentation of the outer contact of the HPGe detector, digital signal processing, and pulse shape analysis (PSA) of the segment signals.

Chapter 3

Experimental Details

This chapter outlines the measurements relevant for this thesis performed using AGATA sub-arrays within the PreSPEC framework at GSI [6]. Summaries of these measurements are presented in a chronological order. In the course of this thesis work, the most important analysis ingredients were to be extracted from the measurements performed last. Therefore, further explanations of analysis methods and the relevant research output very often follow the exact reciprocal time line.

3.1 Overview of PreSPEC-AGATA Experiments

3.1.1 Campaign 2012

The S429 experiment within PreSPEC-AGATA 2012 campaign was conducted in October 2012. It addresses the lack of structural information in the direct vicinity of the heaviest stable doubly-magic nucleus ^{208}Pb, in particular $B(E2; 2^+ \to 0^+)$ values of unstable $Z = 82$ Pb isotopes. Figure 3.1 is an excerpt from the chart of nuclides and reflects the region of interest for both the campaign described here as well as the one which is a subject of Section 3.1.2. The acceleration of primary ^{208}Pb beam was initiated in the UNILAC accelerator [11]. At a second stage, ions reach significantly higher velocities through the SIS-18 synchrotron [12]. Then, the primary beam at 1 GeV/u with all electrons stripped off was delivered to the FRS. Relativistic fragmentation was the reaction chosen to produce lighter isotopes of Pb, Hg, and Pt south-west of ^{208}Pb, i.e. nuclei labelled as '2012 campaign' in Figure 3.1. The beam velocity measured between the second and the final focal plane of the FRS was $\beta = 0.69(1)$. Thereafter, the relativistic Coulomb excitation on the secondary target was the probe for nuclear structure studies via reduced transition strengths, $B(E2; 2^+ \to 0^+)$. Meanwhile, already reported metastable states were used as calibration points

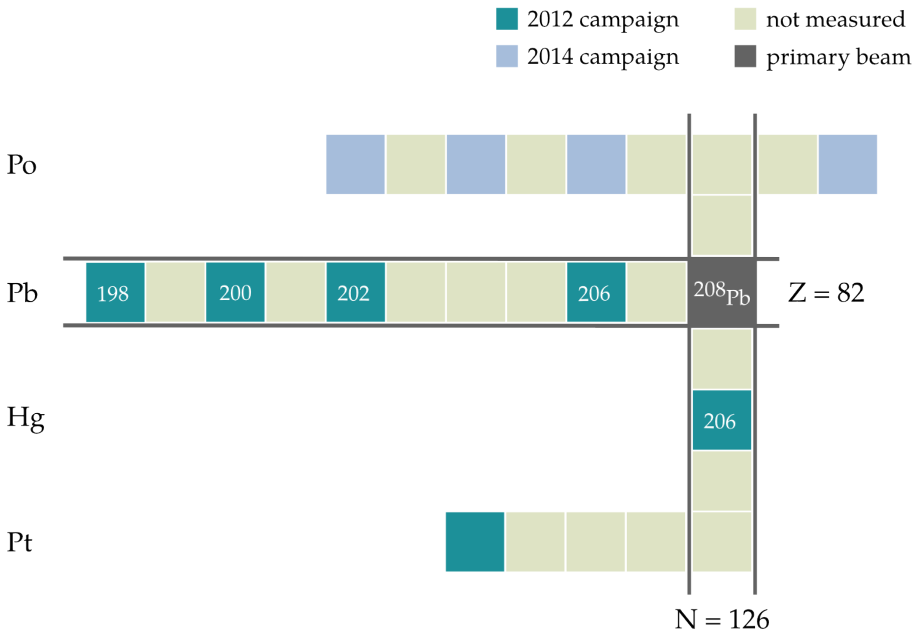

Figure 3.1: Even-even isotopes around ^{208}Pb presented as a section of the chart of nuclides. Horizontal and vertical lines point out the closed proton and neutron shell, respectively. Their intersection correspond to the heaviest doubly-magic nucleus, ^{208}Pb, the primary beam of the S429 experiment performed in 2012. All nuclei labelled with mass numbers are subject of this work. Different colour tags explained in the legend stand for nuclei measured in two different experimental campaigns. Note that the denoted primary beam pertains only to the 2012 campaign. See text for details.

to validate the secondary fragment identification. This was achieved by placing a plastic stopper at the secondary target position. A schematic drawing of the target chamber with placement of the secondary target and the stopper is provided in Figure 2.2. Moreover, the experiment is also able to measure isomeric ratios, hence to corroborate calculations in the realm of reaction theory. To facilitate the measurement, data with the expected metastable states are collected first, followed by the Coulomb-excitation investigations, i.e. shifting always from the *stopped beam* to the *in-beam* experimental setting. The missing information in case of all nuclei studied was planned to be assessed using the integrated detection system described in Chapter 2.

Being the first experiment with AGATA at GSI, S429 had seventeen 36-fold segmented crystals within the AGATA sub-array configuration at the time. To ease the collection of highly-correlated data, measurements were arranged in sequences. For each isotope of interest the isomeric states were studied first, followed by the Coulomb excitation measurement. Analysis of the data was foreseen to follow the same scheme. This decision was further supported by the fact that the observables from the Coulomb excitation measurements need to be corrected for the yield eventually 'lost' by populating isomeric states.

In the context of this work, the isomeric states of the lighter Pb and Hg nuclei were thoroughly studied. They are indicated in Figure 3.1 by their respective mass numbers. The findings of the present analysis help to understand the probability of a multi-nucleon knockout in terms of nuclear reaction theory, as well as certain aspects of the nuclear shell model for this important set of nuclei.

3.1.2 Campaign 2014: In-beam

The continuation of the experiment took place in February 2014 with an upgraded configuration of the AGATA sub-array consisting of twenty one crystals. Target nuclei in the spectroscopic point of view were now those north-west of ^{208}Pb: $^{204-208}$Po populated through the fragmentation reaction of a primary 1 GeV/u ^{238}U beam. Staging of this experiment resembles the scheme outlined in Section 3.1.1, that is to say shifting from the *stopped beam* to the *in-beam* measurement regime sequentially for each nucleus studied.

Because of rather serious difficulties with the restart of the accelerator in early 2014, the measurement was not conducted with the requested beam from the very beginning. Instead, a light ^{56}Fe beam with an energy of $E = 500$ MeV/u was delivered for testing purposes at the start of the 2014 campaign. Nevertheless, this test run facilitating a study of two-neutron knockout in the $^{56}\text{Fe} \rightarrow {}^{54}\text{Fe}$ reaction resulted in an exceptional physics output (Paper IV). Following this commissioning run, the originally planned beam was delivered and those nuclei labelled '2014 campaign' in Figure 3.1 were measured.

The analysis of the $^{56}\text{Fe} \rightarrow {}^{54}\text{Fe}$ case laid the foundation for most of the S429 data evaluation until now. In essence, the decisive observable in this type of studies is the isomeric ratio. Certain metastable states are found at given values of spin, raising the question: Through which reaction mechanism was how much spin imparted to the secondary fragment? For that purpose it is important to examine values of isomeric ratios as a function of spatial distribution of fragments (see, for instance, Figure 3 in Paper IV and Figure 11 in Paper V). Then, these results, compiled with the theoretical predictions, emphasize the relevance of understanding the projectile fragmentation or few-nucleon removal at relativistic energies, namely at 1 GeV/u.

3.1.3 Campaign 2014: Source Measurements

In January 2014 a dedicated measurement was conducted to characterize the set-up by determining photopeak efficiency and peak-to-total (P/T), and to perform a quality assessment of AGATA software algorithms. Although this particular measurement took place between the two campaigns described previously, it is imperative for the data analysis of both of them.

The AGATA sub-array was located at the nominal distance of 23.5 cm from the secondary target. The calibration sources ^{56}Co, ^{60}Co, ^{152}Eu, ^{133}Ba, and ^{166m}Ho were placed in the centre of the target chamber. In order to perform a reliable characterization of the set-up, an external detector – a non-segmented single-crystal Ge detector from a EUROBALL cluster [21] – was implemented in the data-acquisition system as a reference. Each AGATA detector has its respective digitizer, equipped with a flash ADC to digitize the outputs of preamplifiers [24]. The signal from the EUROBALL preamplifier was connected to a spare AGATA digitizer via a converter. The two detector types require somewhat different signal processing. Therefore, only one of the two AGATA digitizer's input ranges was used to handle the EUROBALL signal.

Data recorded with ^{56}Co, ^{60}Co, and ^{152}Eu sources throughout this measurement were analyzed and presented in Papers II and III. The data with the two remaining sources, ^{133}Ba and ^{166m}Ho, is expected to be analyzed within the AGATA collaboration, as it is important for further investigation of high-multiplicity treatment and its effect on low-energy in-beam studies. Moreover, currently there is another study ongoing, regarding assessment of the other tracking code available in the collaboration. Data from this measurement are also scrutinized for the new study [25].

Chapter 4

Data Analysis

In order to utilize enhancements provided by the novel design of AGATA and its realization as AGATA sub-array, there are several corrections which should be performed. Following the related procedures and the terminology of the used AGATA software outlined in Paper II ensures optimized performance of AGATA in the context of the PreSPEC–AGATA campaign. In the current work the effects of these corrections, i.e. fine tunings on the data, will be emphasized. Since the PreSPEC-AGATA campaign comprised experiments performed both in 2012 and 2014, some of these adjustments are exemplified using data from different experiments. For the corrections to be performed, the calibration source data is collected by long (and stable) measurements with the ^{60}Co calibration source. Only once enough data has been recorded for all segments of all crystals, the automatic procedures can be readily applied. Note that potential events in the segments in the back of a crystal are hampered by the absorption depth of a γ ray with typical energies of the ^{60}Co calibration source in germanium. For example, an 1 MeV γ ray penetrates germanium to a depth of approximately 3.5 cm, whereas a typical AGATA crystal has a longitudinal size of 9.0 cm. There are five modes which define how to treat AGATA during data analysis. They are established, explained and contrasted one to another in Paper III. For all S429 experimental data scrutinized within this work, the core common analysis mode was used.

4.1 AGATA Optimization Based on the Source Measurements

4.1.1 Pulse Shape Analysis (PSA)

The PSA algorithm is responsible for decomposing the waveforms, aiming at the information about the γ-ray interaction positions. It essentially compares the recorded waveforms of observed signals with a respective calculated set of reference signals. Within the library of calculated pulses, individual interaction traces for several points of each segment inside the crystal volume have been recorded/simulated [26]. The performance of the PSA relies on those simulations. They therefore consistently implement an understanding of the crystal properties, such as field lines, potentials, space charge, crystal orientation, mobility of electrons and holes, electronic response functions and cross talk (see Section 4.1.3). By means of the available contrasted traces, the PSA algorithm (for the one used in this work see [27]) looks for those that satisfy an agreement condition. For the interaction point to be reliably assessed, contributions from the signal of the central contact, from the segment with the net charge, as well as from the neighbouring segments have to be taken into account. Finally the conversion into position information is performed. The implementation of several PSA algorithms in the available analysis software within the AGATA Collaboration has been asserted and thus they are widely used. In the following text they, alongside some of their operational properties, are listed:

1. *Adaptive Grid Search*: standard PSA-procedure first roughly localizes the interactions on a coarse grid, then refines the grid close to the identified potential interaction positions. This "family" of algorithms has the hard-coded maximum number of hits in one detector set to 12. On-line implementation of the AGATA PSA relies on this approach.
2. *Adaptive Two Interactions*: first the comparison as in algorithm 1 is performed, then two interactions per active segment are considered. How much the experimental signals and simulated traces look alike (or do not) is evaluated by calculating reduced χ^2. Therefore, within this type of algorithm, the reduced χ^2 is calculated for both a one- and two-interaction scenario. Only if the latter is at least 10% better, two interactions in the considered segment are accepted.
3. *Segment Center*: simple procedure as if every interaction took place in the center of the segment. This approach requires files containing pulse shapes for the centres of all segments with respect to three different shapes of AGATA crystals. This PSA could also be performed at a later point,

via the so-called *Post-PSA*. By doing so, the original data is not being compromised, neither are any fine-tunings.

In Paper III Section 5 it is stated that using the two types of Adaptive Grid Search algorithm did not yield different results. However, it is important to note that the algorithm 2 would interpret significantly less interactions as being due to a single hit in a segment. Hence, the performance of tracking in terms of single-interaction contributions depends on whether decomposition of the signal allows for more than one interaction per segment or not [25]. Unlike the online implementation of AGATA PSA, which seeks single interaction within a segment (algorithm 1), GRETINA's decomposition algorithms allow for more then one interaction per segment. This approach is described in Reference [28] and its effects are demonstrated in a recent study [29].

4.1.2 Energy Calibration

First and foremost, energy calibration coefficients should be extracted from the amplitude spectra (recorded by the *Producer*, see Paper II and Appendix in Paper III) for both the segments and the central contact. Provided this information, spectra written by the next actor to come, *Preprocessing*, are properly calibrated and the *PSA* can be applied subsequently. Due to intrinsic limitation of the segments' digitizers, namely the flash ADCs implemented in them, segment spectra exhibit certain non-linearity, which does not allow the obtained calibration coefficients to be generally valid. This leads to obvious dissimilarity in the sum of calibrated energies measured in the individual segments and the energy recorded by the central contact of one and the same crystal. Such a pronounced difference can be seen in Figure 4.1. It significantly affects the performance of tracking (see Section 4.1.3). Therefore, this effect is treated at the final step before the global-level data processing, namely *Post-PSA*. At this stage the segment energies are renormalized such that their sum corresponds to the energy recorded by the central core contact.

In the following, this renormalization will be referred to as the condition of equality of segment-sum and core energies. Table 4.1 summarizes all crystals operational during the 2012 experiment, their central-contact energy resolutions and averaged segment resolution. Prior to the analysis of the stopped-beam data (see Section 4.3), the energy calibration of the central contact was refined by using the background 511-keV annihilation γ-ray line and/or one of the ^{60}Co γ-ray lines in energy spectra reconstructed from the particle-ungated AGATA data. For this purpose, the *Post-PSA Filter* was utilized to readily implement newly obtained calibration coefficients and pass the recalibrated data further to the global level. The data on which this correction was performed comprised the FRS isomer settings dedicated to ^{206}Pb, ^{202}Pb, ^{200}Pb, ^{198}Pb, and ^{206}Hg,

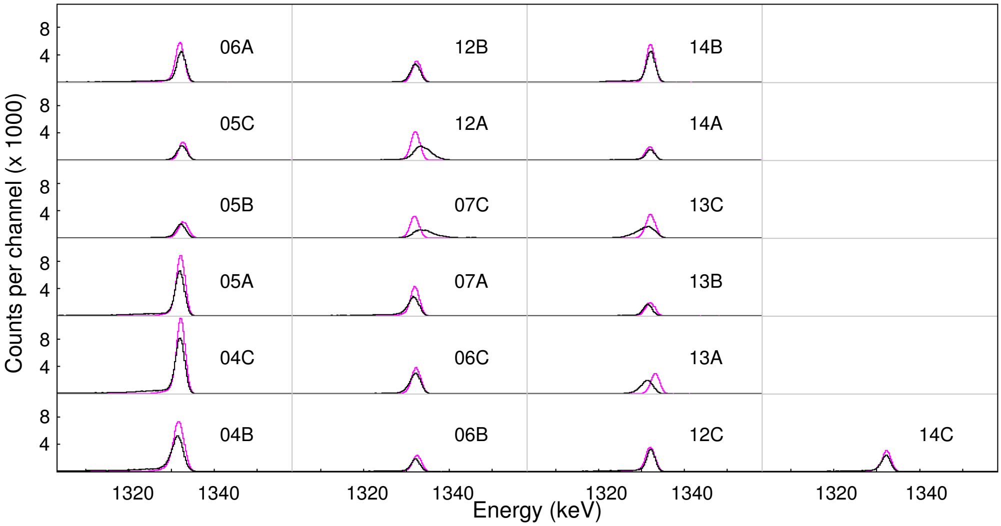

Figure 4.1: Comparison of the energies recorded by the central contact and the segment sum at $E_\gamma = 1332$ keV for 19 AGATA crystals. Magenta lines show the calibrated spectra of the central contacts. The spectra in black show the respective segment sum.

i.e. when implanting the selected ions in a passive plastic stopper (Section 4.3). Thereafter the corresponding AGATA runs were recalibrated by means of a linear calibration either with unique pairs of coefficients per crystal for a whole run or, in case of longer runs, splitting data in two portions and extracting separate coefficients. Such treatment allowed to correct for energy shifts throughout the course of the experiment. Figure 4.2 characterizes the effect of recalibration expressed in relative energy difference for two γ-ray lines in case of individual crystals. All crystals show that the peak shift, relative to the theoretical value of the respective γ-ray line, is smaller than 0.05%, which denotes noticeable improvement in peak position. Statistics of the spectra used to perform this correction was not favouring the line $E_\gamma = 1173$ keV, as it was applied to the experimental data directly.

4.1.3 Cross Talk

AGATA detectors, being the novel highly segmented Ge detectors, have the outer electrode divided by segmentation lines. Each of the segments is read out with a charge-sensitive preamplifier. Such a design allows the γ-ray energy to be obtained either from the energy depositions in all 36 segments or conventionally from the signal of the central contact, which is the inner core electrode. For the former, the contributions from active segments, i.e. those that fired, are added to

Table 4.1: Energy resolution of AGATA crystals measured at the ^{60}Co-source energy of 1332 keV.

Detector	Crystal ID	Core FWHM (keV)	Segment FWHM (keV)
00B	1	2.53	2.02
00C	2	2.43	2.03
01B	4	2.43	2.15
01C	5	2.35	2.16
04B	13	2.30	2.04
04C	14	2.27	2.09
06A	18	2.49	2.25
06B	19	2.57	2.08
12A	36	2.65	2.16
12B	37	2.43	2.53
12C	38	4.31	2.44
13A	39	2.42	2.54
13B	40	2.49	2.17
13C	41	2.53	3.25
14A	42	2.62	2.16
14B	43	2.32	2.29
14C	44	2.59	2.13

create the energy spectrum. The advantages of the electrical segmentation have been explained in Paper III and Section 2.2, but the practical drawbacks have also been extensively studied [30]. One of the well-known problems is the so-called *cross talk* between the segments, which is caused by the mutual electrical couplings of these. Its effects are easily demonstrated with respect to the *segment fold*, which is the number of segments firing simultaneously. Figure 4.3 shows γ-ray spectra around the 1332 keV line of the ^{60}Co source measured by one AGATA crystal, ID = 12A. The spectra are constructed by means of segment add-back, namely summing the calibrated contribution of each fired segment as a function of segment fold. Not only does the position of the peak shift as the segment fold increases, but also the FWHM deteriorates, thus broader lines. The energy resolution is worsened and an energy deficit is observed in case of multiplicities larger or equal to two. A more detailed investigation (see References [31, 32]) has shown that these effects stem from dependency of the sum of segment amplitudes on the hit pattern. Such limitations could be overcome by applying a numerical correction on the data. This procedure is explained in References [31–34]. The amplitude recorded by each segment can be readily corrected with respect to the linear combination of the amplitudes seen by all other segments. As a result, the observed line shift may be compensated for. This is depicted in the right panel of Figure 4.3.

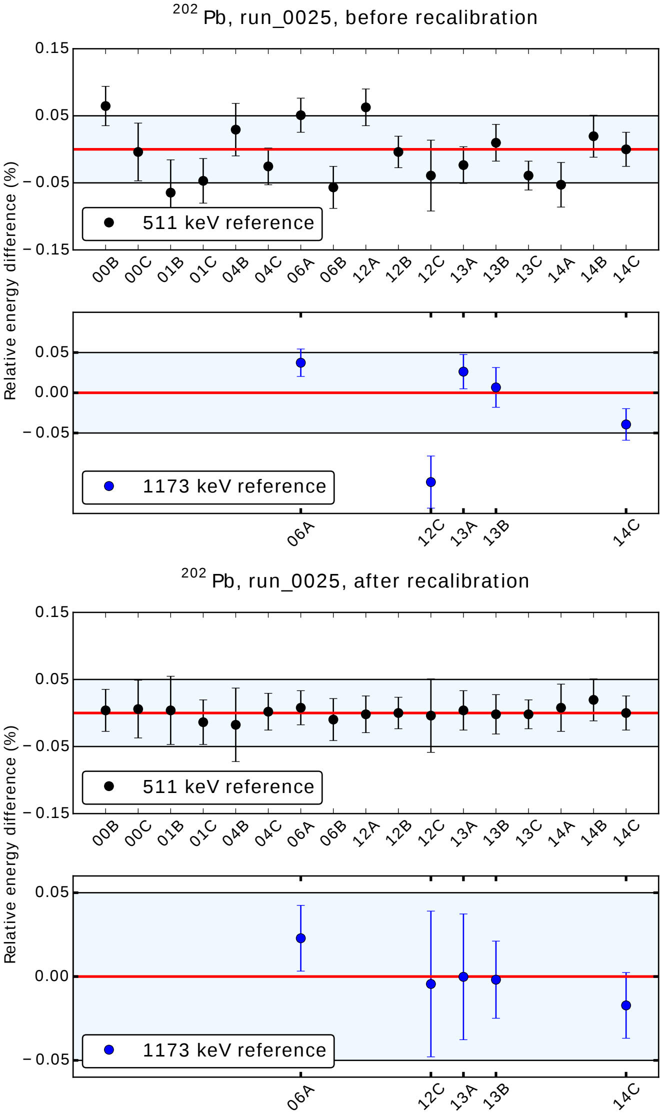

Figure 4.2: Relative difference between the measured and theoretical value of $E_\gamma = 511.0$ keV and $E_\gamma = 1173$ keV for corresponding AGATA crystals denoted on the x-axis (upper panel). The lower panel exemplifies the effect of additional energy calibration performed at the final step of the local-level processing (see text for more details).

Another representation of the correction algorithm effect is seen in Figure 4.4. The energy information obtained from the segment add-back is now contrasted to the one recorded by the central contact. The difference between the peak position of 1332 keV ^{60}Co line in segment add-back and central contact spectra is shown versus segment fold before (red circles) and after (blue stars) correction.

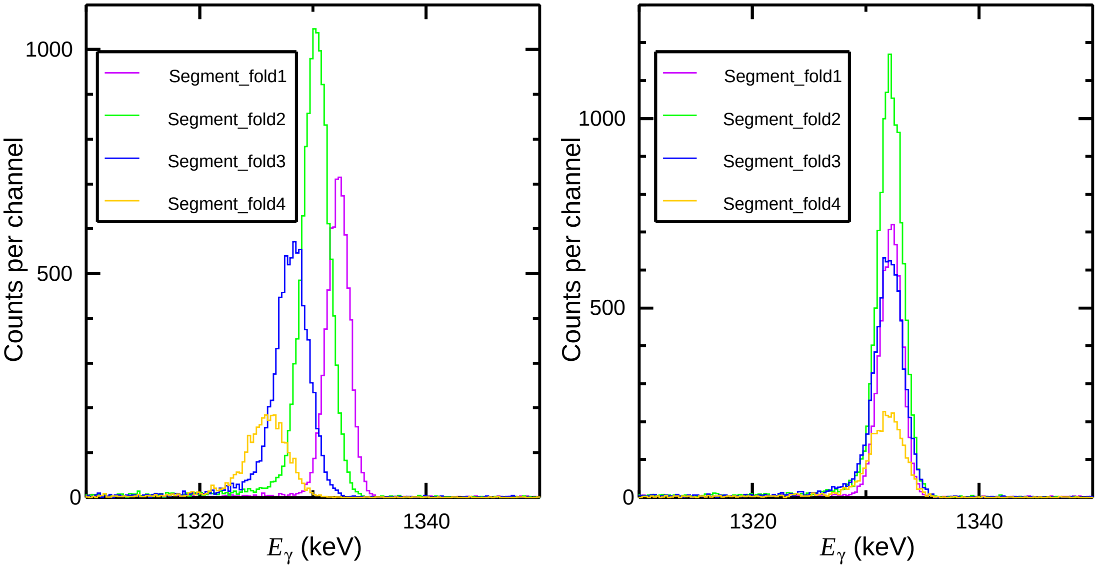

Figure 4.3: Energy spectra reconstructed for crystal 12A by adding back the active segments for different segment folds listed in the legend. The ^{60}Co γ-ray line at $E_\gamma = 1332$ keV is shown before (left panel) and after (right panel) performing the cross-talk correction. The fold-dependent line shift is obvious and explained in the text.

The same AGATA crystal as in Figure 4.3 was used as a reference. The correction algorithm reduces the discrepancy between the energy information obtained in two different approaches. However, for higher multiplicities the effect of the fold-dependent line shift persists. In practice, in order to collect reliable source data for performing the cross-talk correction for higher folds, sufficient data should be taken, both by choosing an appropriately strong radiation source and adjusting the measurement time. Moreover, even the implementation of the algorithm does not allow for correction of the energy deficits of higher folds by explicitly adjusting the energy information of every individual segment. It is rather expressed in terms of the deficit of the involved pairs of segments [31].
So far, the cross-talk effects have been described only locally on the level of a single crystal. If AGATA data is to be used in the tracking mode (see Paper III), the energy information recorded by individual segments is essential. Therefore, γ-ray tracking requires properly adjusted segment energies. In order to see the relevant effect of the cross-talk correction on the global level, there is an additional adjustment to be made, which is neither affected by the correction-algorithm treatment of higher folds, nor does it allow some discrepancies to affect the final tracked spectrum. Essentially, the calculated energy deficit is related

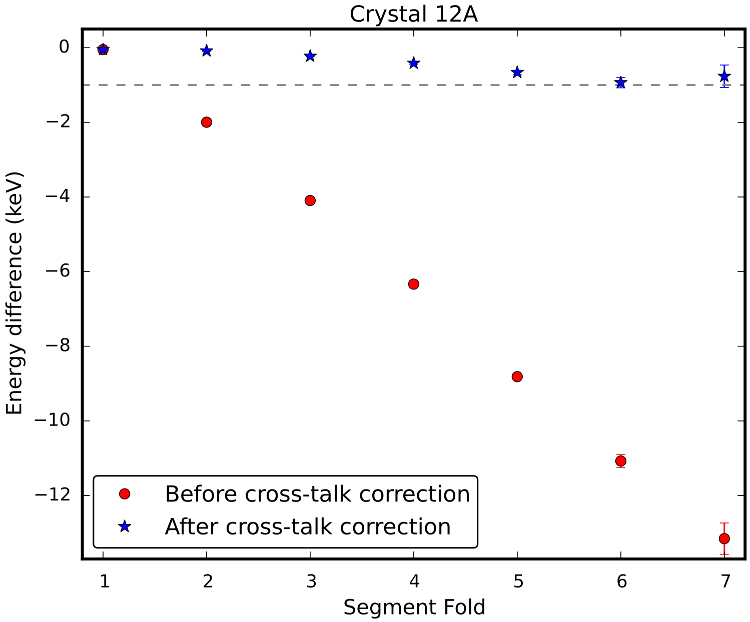

Figure 4.4: Difference between segment sum energy peak and the central core contact energy at $E_\gamma = 1332$ keV for crystal 12A. The shift of the peak position is displayed as a function of increasing segment fold. The dashed line is drawn for the value of ordinate equal 1 keV.

to the energy recorded by the segments and distributed after the local-level treatment. This compensates for any non-linearity effects (see Section 4.1.2). In our quality assessment of cross-talk and non-linearity correction, this equality condition of segment-sum and core energies represents one of the two parameters. The other one is the cross-talk correction related to the local level, as explained previously. Table 4.2 lists the total of four different combinations using these two operations and provides a naming convention used to classify the corresponding spectra.

In the following, the evaluation of the tracked spectra with respect to the cross-talk correction is performed based on Figures 4.5 and 4.6.

Table 4.2: Overview of the settings as a result of different operations combinations for assessment of quality of the cross-talk and non-linearity correction. These settings refer to the tracked spectra shown in Figure 4.5.

	Operation		Setting Number
	equality of segment-sum and core energies	cross-talk correction	
Presence	X	X	0
	✓	X	1
	X	✓	2
	✓	✓	3

In the following, the evaluation of the tracked spectra with respect to the cross-talk correction is performed based on Figures 4.5 and 4.6.

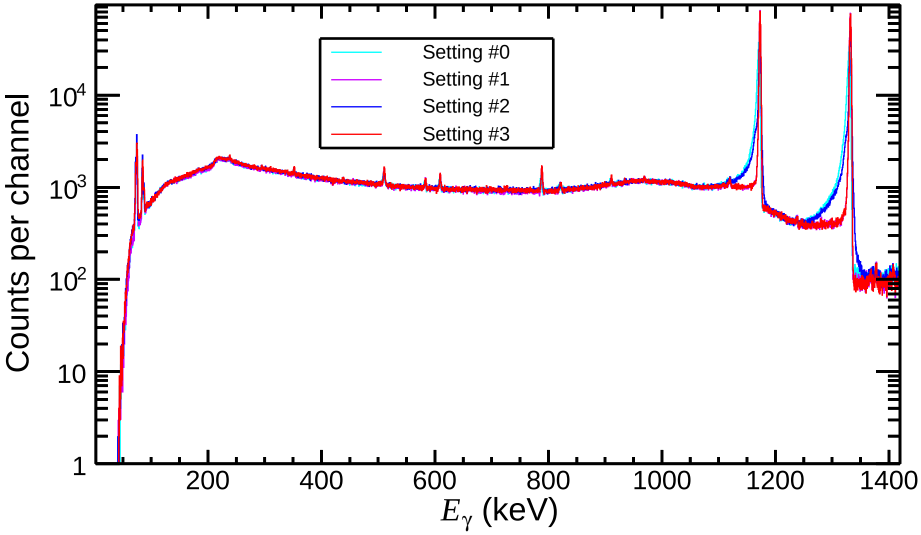

Figure 4.5: ^{60}Co tracked spectrum for four different parameter combinations regarding the cross-talk and non-linearity correction. Different colors of spectra indicate the so-called setting number, as assigned in Table 4.2.

A particularly interesting case is setting number 2. Although the cross-talk correction has been performed for every crystal, some shifts are obvious. Judging by Figure 4.4, the cross-talk correction does not really cancel the line shift completely, especially for higher multiplicities. It is apparent that these adjustments can affect the data tremendously and compromise the quality of spectra.

In general, a pronounced difference is observed when switching the equality con-

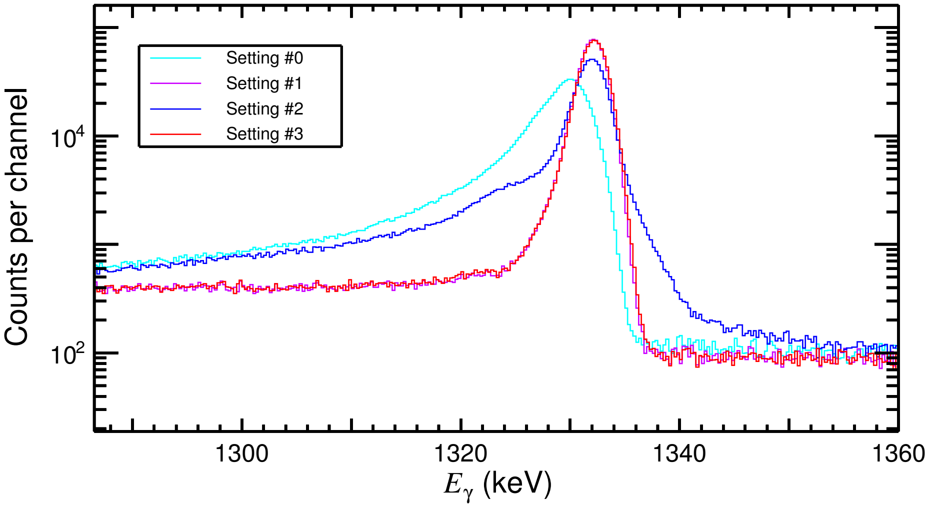

Figure 4.6: ^{60}Co tracked spectrum for four different parameter combinations regarding the cross-talk and non-linearity correction with an emphasis on $E_\gamma = 1332$ keV. See Table 4.2 and text for more details.

dition on and off, whereas the cross-talk correction does not seem to have a large impact on the overall quality of the spectra. To clarify this, in addition to the explanation provided thus far, individual crystal spectra were investigated; for each crystal the energy information seen by the core was contrasted to the segment sum energy (see Figure 4.1 and Section 4.1.2). Note that this comparison does not include the equality condition of segment-sum and core energies, which is why discrepancies are observed in several crystals. It is obvious that some of the crystals have worse energy resolution. This should have been improved by the cross-talk correction, if the mutual capacitive coupling was the cause of it. Therefore, before proceeding to the global-level data treatment, the individual cross-talk correction should be revised for the crystals in case of which the central contact and segment sum energy differ substantially. Regardless of the cross-talk correction, the overall performance of the crystals in question should be investigated, such as gain stability, missing/broken/unstable segments, which is sometimes influenced even by the automatic liquid nitrogen filling.

Finally, before choosing the right set of parameters described in this section, all the adjustments should be revisited. The mode of data treatment should be decided upon, based on the actual experiment and such that the refinement efforts can be properly channelled. For example, if data analysis of a certain experiment is primarily the core common AGATA data treatment, then (re)calibration of the central contact energies is the most important. As soon as the segment energy information is used, i.e tracking, proper energy-calibration and cross-talk correction coefficients become at least equally relevant. Only then one needs to consider to finally exploit different parameter combinations presented in Table 4.2.

4.1.4 Timing

The format of the time information an AGATA crystal is influenced by the specifically-tailored AGATA digital electronics [5]. The *Global Trigger and Synchronization*, GTS [35] sets the 100-MHz clock and a time stamp to each of the AGATA digitizers. In order to correlate time signals of all individual detectors, a time-stamping system is developed to translate the clock pulse sent from the GTS into a time information of when a certain event happened relative to the beginning of the run. Paper II explains how the alignment of such time information is practically performed at which data-processing stage.

AGATA data is formatted in such a way that it represents the so-called *AGATA Data Flow*, ADF [36], which is a composite structure. The incorporated substructures, called data frames, contain the information from different data-processing stages. In the current implementation of ADF there is a record of the event time information, but not explicitly of the segment time. However, in the design of data words enough place has been reserved, if proven valuable to include segment time information in the data flow as well.

4.2 Source Measurements

The performance of AGATA within the PreSPEC-AGATA experimental campaign was carefully examined by means of a series of source measurements. This is described in detail in Paper III.

4.2.1 External Trigger Method

For this purpose an external non-segmented and electrically cooled HPGe detector [37], based on an EUROBALL capsule [20] was added to the set-up. It was used as an external trigger while employing compatible AGATA electronics, i.e. its output was sent to one of the AGATA digitizers. Therefore, the signal from the detector was split in two: one for the core- and the other one for the segment digitizer, giving in total three raw signals to mimic conventional AGATA readout. Since the EUROBALL capsule is a non-segmented detector, in AGATA data-analysis terminology it was sufficient to process the signal from the central contact only. As a consequence, the existing sophisticated PSA algorithms developed for AGATA crystals cannot be directly applied to this external crystal. Any link between the EUROBALL capsule and PSA is hence only formally established (see Paper III).

The analysis algorithm was modified so that the data from two completely different detector types could be treated within the analysis framework for AGATA detectors. In other words, the EUROBALL capsule was integrated as if it were one of the AGATA crystals. Hence, its data could be processed in the same way as of an AGATA crystal (see Appendix A of Paper III).

The absolute efficiency at 1173 keV in all five analysis modes is extracted from the ratio of the intensity in the 1173 keV peak measured by AGATA crystals over the intensity of the 1332 keV peak measured by the EUROBALL capsule. In this case, P/T was calculated as a ratio of the yield of the peak at 1173 keV and the total number of counts in the spectrum in the energy range $E_\gamma = [20, 1500]$.

4.2.2 Background Subtraction

The spectra obtained with this approach are practically background-free, so there was no need for any explicit background subtraction. However, an additional check was performed to make sure that the gate set on the 1332 keV peak measured by the EUROBALL capsule was wide enough. It was performed via the so-called 'background gating' to see if there were any random coincidences contributing to the background.

For this analysis, three spectra with three different gates (see Figure 4.7) were generated:

1. A complete spectrum by gating on the 1332-keV peak, where the gate was n channels wide: from a to b.
2. A spectrum by gating on the left-hand side background of the 1332-keV peak. The gate was n/2 channels wide: from a-n to a-n/2.
3. A spectrum by gating on the right-hand side background of the 1332-keV peak. The gate was n/2 channels wide: from b+n/2 to b+n.

Then the spectra from items 2 and 3 were summed and subtracted from the spectrum 1 to generate the new background-suppressed spectrum. The comparison of the background-suppressed spectrum and the one obtained in item 1 is shown in Figure 4.8. There is no noticeable difference in these two spectra, apart from some channels, where one could differentiate the cyan spectrum from the red one. However, this difference is negligible, which suggests that the external-trigger method does not require additional background suppression on the generated spectra.

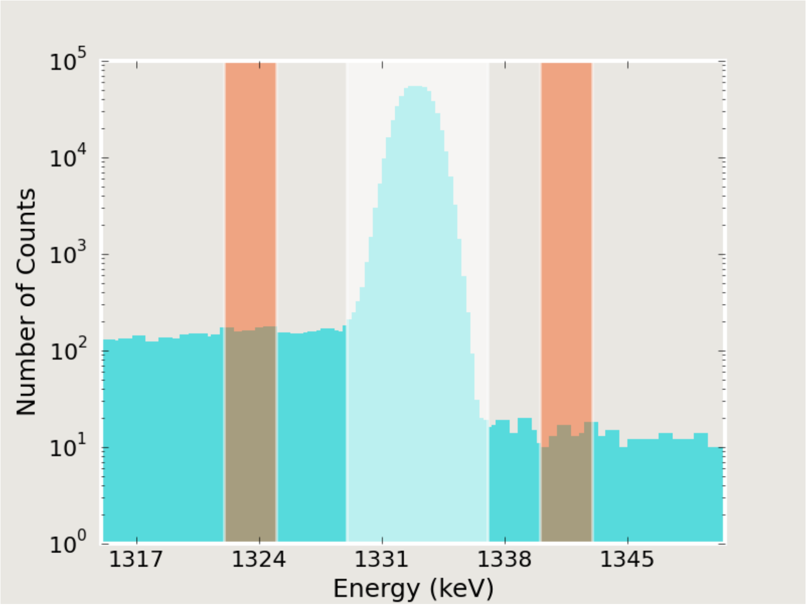

Figure 4.7: An illustration of the 'background gating' method applied on a ^{60}Co tracked spectrum. The white band in the middle represents the 'peak channels' described in item 1, whereas the orange bands show the left- and the right-background channels from items 2 and 3, respectively

4.2.3 Tracking

All aspects of γ-ray tracking algorithms relevant for the current analysis are discussed in Paper III. Essentially, *Figure of Merit*, FOM, is a criterion of how exclusive the chosen tracking algorithm is. Both tracking codes available in the AGATA collaboration [38, 39] rely on their own implementation of this measure. Since they are both of the forward-tracking algorithm type, most considerations for the evaluation of the FOM are centred around accurately extracting clusters with single-hit interactions. One of the advantages offered by the novel HPGe tracking arrays composed of electrically segmented crystals is the possibility to handle high γ-ray multiplicity events due to the high granularity. Although the experiments with fast heavy-ion beams usually do not produce high multiplicity events, it is important to test the effect higher multiplicities might have on the tracking algorithm. Moreover, it is the accuracy of the Doppler reconstruction of the in-beam data that could be influenced by this. This has been studied in a recent work [25], both 'creating' higher multiplicity events from the source data followed by the tracking algorithm performance analysis, as well as by looking into in-beam data.

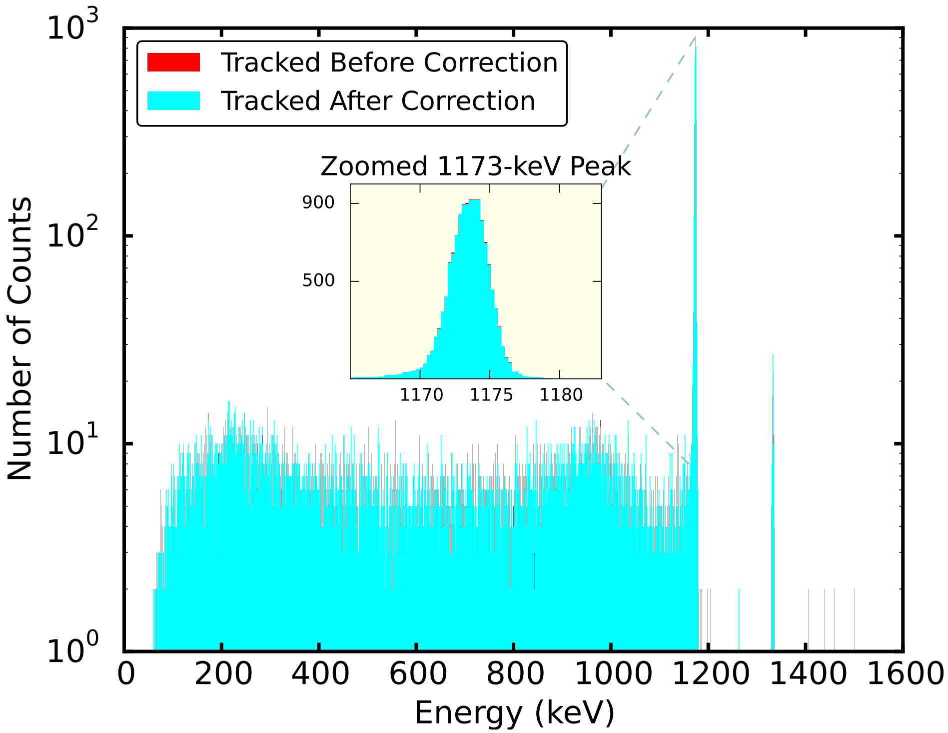

Figure 4.8: ^{60}Co tracked spectrum before (red) and after (cyan) applying the 'background gating' method. The peak at $E_\gamma = 1173$ keV is shown in the inset. Essentially there is no difference in the two spectra: the red one is being completely 'covered' by the cyan one with only a few disparate bins emerging.

4.2.4 Add-Back

To complete the transition, which relates to how data is analyzed, from conventional arrays towards the novel tracking arrays, the nearest-neighbour add-back routine was developed. Choosing the add-back approach is viable only for events where multiplicity exceeds one. All individual hits within an event are filtered and selected only if they were found within a sphere of a certain radius. The sphere was to be created around the hit with maximum energy deposition. For this particular analysis different radii were investigated and the reference value chosen was the radius of 100 mm (see Paper III for more details). For absolute efficiency considerations, data collected with the external trigger method was used.

At present, no physics results of this work rely on the investigation using the add-back mode of analysis. However, a few recent publications [29, 40] emphasize the improvement of the in-beam spectra quality seen when utilizing the nearest-neighbour add-back routine. So far, such an investigation has been done with the in-beam data collected during neither of AGATA campaigns at GSI (see Chapter 3).

4.2.5 Close Position

For the main measurement foreseen by the S429 experiment, Coulomb excitation of isotopes near the primary ^{208}Pb beam, the optimum target was placed at the so-called 'nominal position', i.e. 23.5 cm upstream from the centre of AGATA sub-array. The majority of the performance and characterization measurements with radioactive sources used the same arrangement. See Papers II and III for detailed description of these measurements and their results. However, while AGATA was residing at GSI, both experimental campaigns also made use of a somewhat modified set-up: a more forward placement of the secondary target, the so-called 'close position', 15 cm closer to AGATA. Not only have physics experiments been carried out in such an arrangement [41], but also a number of valuable stopped-beam runs. Chapter 4.3 identifies the relevance of these data. For the stopped-beam measurements a plastic stopper was inserted instead of the secondary target.

In addition to AGATA experiments at 'nominal position', in the course of the 2014 experimental campaign efficiency runs were performed to characterize the modified, 'close position', set-up. In practice, thickness of the plastic stopper was accounted for by placing calibration sources both in front of and behind it. The absolute efficiency in the core common mode of analysis was then evaluated as an average of the values obtained from each of the two positions. The values deduced from this efficiency evaluation are essential to calculate isomeric ratios as shown in Papers IV and V. For a comprehensive display of the results and a comparison with other source data investigations, the reader is referred to Paper III (see, for instance, Figure 5 and Table 2).

4.3 Isomeric Ratios

The research goal of the S429 experiment might appear as greatly varying when identified with respect to its distinct scientific motivation (primary being the in-beam studies) and the empirical methods applied directly upon its evaluation (secondary - isomeric decays).

First of all, online observation of 'isomeric γ rays' serves as a confirmation of the applied FRS settings. Secondly, an unambiguous determination of the secondary beam content arriving at the reaction target is necessary for obtaining precise $B(E2, 2^+ \to 0^+)$ values. This primarily regards those beam particles which can reach the target in a metastable state. Currently available literature data

[42–45] suggest that the nuclei of interest indeed are expected to have isomeric states populated in the fragmentation reaction at the primary target. If the measured half-lives allow them to survive the flight path through the FRS, they could affect the number of particles which can be subject to Coulomb excitation of their ground states. Besides isomeric ratios, however, a detailed spectroscopic investigation of isomeric decays was not foreseen within the scope of the S429 experiment. The established procedures to deduce isomeric ratios (see, for instance, References [46–48]) were followed. They are detailed in this Chapter alongside an example offering a practical explanation of different parameters and observables which are introduced first.

4.3.1 Half-life Determination

Known half-life data already contain rather precisely measured values for the isomeric states of interest. Nevertheless, the acquired statistics in the S429 isomer-centred settings appeared adequate to deduce independent half-life values. The precise method how the half-lives were evaluated is outlined in this Section.

The half-life of a certain isomeric state can be addressed via the γ-ray transition(s) following its decay. In case that the de-excitation happens through a sequence of transitions, it is important to verify that there are no other isomeric states with comparable half-lives occurring in that particular sequence.

The time analysis of the current study was performed starting from energy-time matrices created from the S429 stopped-beam data. One of the most important conditions when constructing such a matrix was the time window utilized for merging different data formats corresponding to FRS and AGATA data acquisitions. The time analysis of isomeric states with very dissimilar half-lives (several orders of magnitude) would benefit from having this time window as wide as possible, as it is often done in dedicated isomeric-decay studies. However, our choice of the width of the time-window was restricted to $\Delta T = 20\ \mu$s due to particular features of the experimental set-up and implementation of the trigger [24]. This imposed a limit on the isomeric states for which the half-lives could be determined, allowing the measurements between a hundred nanoseconds and several microseconds. An example of an energy-time matrix is shown in Figure 4.9.

Before making a projection upon the time axis to deduce the half-life of the isomeric state of interest, a two-dimensional gate is applied to exclude the 'prompt flash' (see Section 4.3.2) and distinguish the isomeric decay. Gates in energy are then applied on such filtered data, i.e. peak areas of the γ transitions originating from a chosen isomeric state are selected and the time spectra are generated. Moreover, the same so-called 'background-gating' procedure explained in Sec-

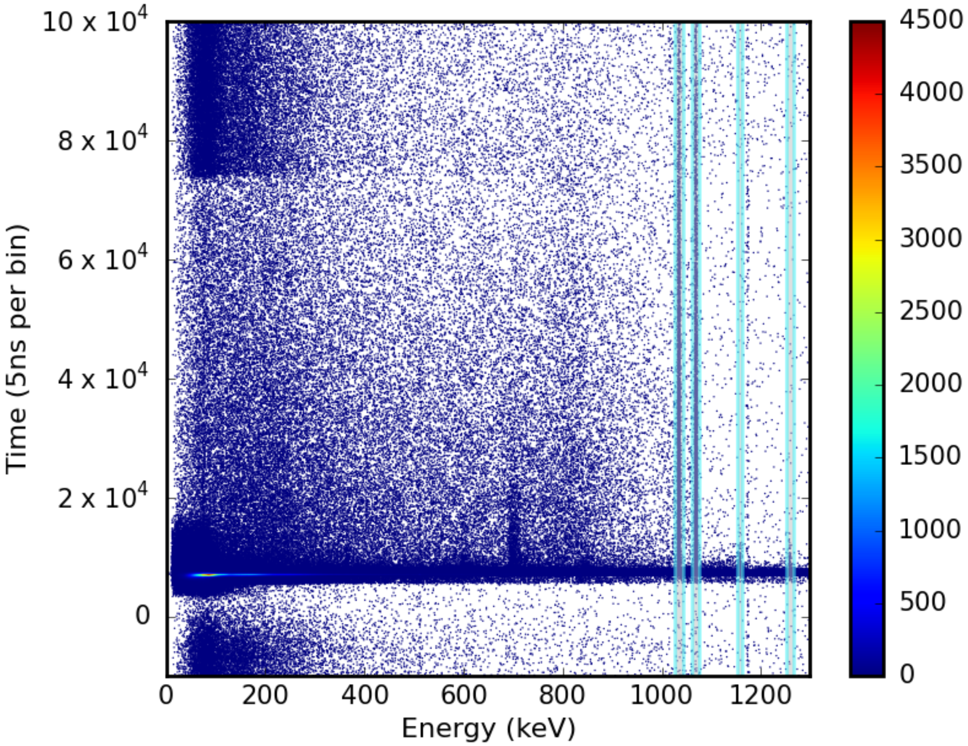

Figure 4.9: Two-dimensional histogram showing energy on x- and time on y-axis for the ^{206}Hg isomer-centred setting. The decays of the two isomeric states with $I^{\pi} = 10^{+}$ and $I^{\pi} = 5^{-}$ (see Figure 4.11) are apparent and enclosed by cyan horizontal bands (from left to right: 1034, 1068, 1157, and 1257 keV). A colormap on the right side indicates the content of each bin.

tion 4.2.2 was used for this analysis in order to subtract background and single out any random coincidences. Finally the resulting time-decay spectra were used to extract the half-life by means of an exponential least-squares fit.

Since the content of the resulting histogram is a linear combination of the contents of the three individual histograms (peak, left- and right background), the corresponding uncertainty per channel is calculated as a square root of the sum of individual standard deviations. This uncertainty is referred to as *experimental uncertainty*, which differs from the *'default' uncertainty* calculated as a square root of the resulting histogram's content. Therefore, the distinction between these two values serves as a first criterion for the assessment of the half-life evaluation.

There is a whole variety of isomeric states with varying half-lives the decays of which are observed in this experiment. The bin width of the resulting time-decay spectrum (histogram) should be adapted to the half-life of the state accordingly. Hence, the bin-width choice dictates another important criterion for half-life determination.

Due to the exponential nature of radioactive decay, either a two- or three-parameter exponential function (f_{2par} Equation 4.1 or f_{3par} Equation 4.2) can be used to fit the data in the time-decay spectrum in the following way:

$$f_{2par}(x) = A_0 \cdot e^{A_1 \cdot x} \tag{4.1}$$

or

$$f_{3par}(x) = A_0 \cdot e^{A_1 \cdot x} + A_2. \tag{4.2}$$

Here, the parameter A_1 has a physical meaning of the decay constant, λ. Consequently, once the value for A_1 is obtained from the fit, the related half-life is calculated as:

$$T_{1/2} = \frac{ln2}{\lambda} \equiv \frac{ln2}{A_1}. \tag{4.3}$$

An optimum fit was found using a χ^2 minimization procedure:

$$\chi^2(A_0, A_1, ..., A_n) = \sum_{i=1}^{nbins} \left(\frac{y_i - f(x_i, A_0, A_1, ..., A_n)}{\sigma_i} \right)^2, \tag{4.4}$$

implemented in ROOT [49], where y_i represents the measured bin i content, $f(x_i, A_0, A_1, ..., A_n)$ is the value predicted by the function used to fit the data $\big[$in this particular case either $f_{2par}(x)$ or $f_{3par}(x)\big]$ in bin i for the given set of parameters $(A_0, A_1, ..., A_n)$, and σ_i is the uncertainty on the measured bin i content.

The result of the fitting routine is also sensitive to the range in which the chosen function is contrasted to the data points. Therefore, the fitting range is yet another criterion for the 'goodness' of the fit evaluation.

Finally, after applying the method described above to the functions in Equations 4.1 and 4.2, the uncertainties associated with the fit appeared to be much larger for the function with three parameters, thus leaving the two-parameter function as a natural choice to be further evaluated.

An overview of the described criteria as a basis for the most reliable half-life value extraction is shown in Table 4.3. Each criterion could be interpreted as a parameter which could have different values practically representing a *number of unique choices*, n_1-n_4. Independently on the isomeric state of interest, there are only two possibilities for both the bin content uncertainty (*experimental* or *default*) and the fit function type (a two-, f_{2par}, or three-parameter exponential function, f_{3par}), leading to $n_1 \equiv n_2 = 2$. The other two criteria are directly dependent on the state of interest and its half-life, thus without a universal

Table 4.3: Relevant criteria for the evaluation of the $T_{1/2}$ quality.

Criterion	Number of unique choices
Bin content uncertainty	$n_1 \equiv 2$
Bin width	n_2
Fitting range	n_3
Fit function type	$n_4 \equiv 2$
Number of possible combinations	$n_1 n_2 n_3 n_4$

number of unique choices. Choosing the two-parameter function to fit the data (n_4=1), total number of fits reduces to $2n_2n_3$.

For the remaining individual fits the values of χ^2 were investigated along with the resulting values of the fit parameters (cf. Equation 4.4) and their uncertainties. This step usually ruled out a significant number of less reliable fits, mostly resulting in $\sim n_3$ of those not being discarded. The last step aimed to derive the average of the $T_{1/2}$ values from the remaining fits as displayed in Figure 4.10. As an example, the shorter-lived isomeric state of ^{206}Hg with $I^{\pi} = 10^{+}$ was chosen (cf. level scheme in Figure 4.11). The final value of the half-life was deduced from this fitting procedure and accounted for systematic uncertainties leading to $T_{1/2} = 106(15)$ ns. Note that the choice of the values for the criteria n_2 and n_3 listed in Table 4.3 specific to the longer-lived isomeric state of ^{206}Hg with $I^{\pi} = 5^{-}$ was quite different.

4.3.2 Calculating Isomeric Ratios

Quantifying the portion of all nuclei produced in a specific isomeric state and implanted in the secondary target means calculating an isomeric ratio (IR). A reliable approach to measure the IR was established a few decades ago and is thoroughly presented in Reference [46] as well as in References [47] and [48]. The IR is a measure for the probability that a certain isomeric state is populated in an observed nucleus, R_{exp}:

$$R_{exp} = \frac{N_d}{N_{imp}F} \cdot 100, \tag{4.5}$$

where

$$N_d = \frac{N_\gamma}{\epsilon_{abs} b_t}(1 + \alpha_{tot}) \tag{4.6}$$

and

$$F = f_1 f_2 f_3 f_4. \tag{4.7}$$

N_{imp} is a measure of the total number of identified ions, implanted in the plastic stopper. The variable N_d represents the number of detected γ-ray decays from

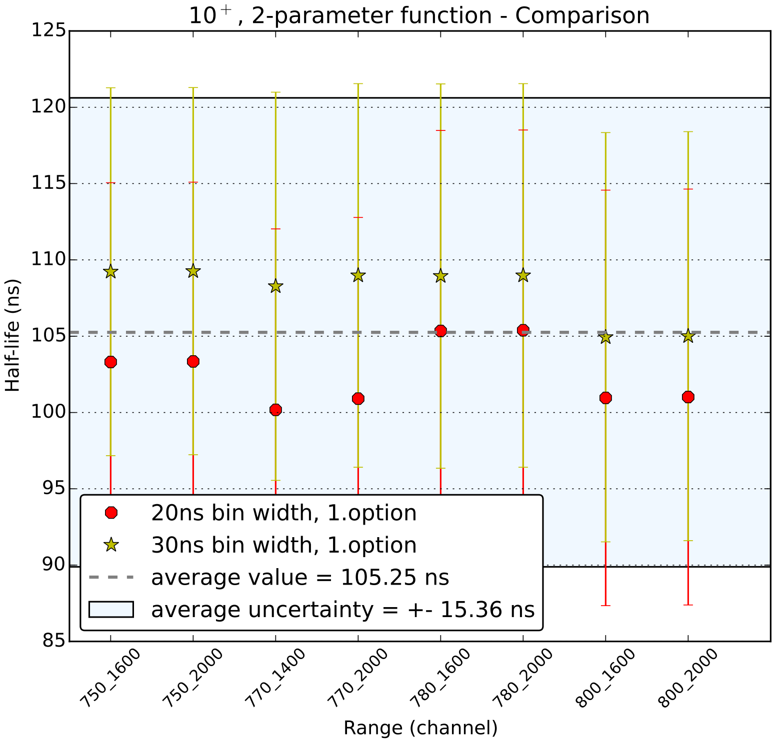

Figure 4.10: Dependency of half-life results on different fit ranges chosen. The figure illustrates the conclusion of the method used to deduce the half-life in case of the $I^\pi = 10^+$ state in ^{206}Hg. Both data sets refer to '1. option' used for fitting which comprises the experimental uncertainty of bin content and the two-parameter fit function. Red circles indicate the points obtained for 20-ns binning, i.e. for only one value of n_2 (see Table 4.3), whereas green stars refer to 30-ns binning. The dashed line designates the average value of the half-life and the blue-shaded band its uncertainty.

the particular isomeric state corrected for the absolute efficiency of the sub-array, ϵ_{abs}, its corresponding branching ratio, b_t, and the competing electromagnetic de-excitation channel, internal conversion, expressed via the total internal conversion coefficient, α_{tot}. For the presented study all internal conversion coefficients are extracted from References [50, 51]. The multiplication, F, of individual correction factors, f_1 to f_4, denotes the effect of the experimental apparatus.

f_1 – interference of the prompt-flash events

The 'prompt flash' [52] is fast continuous radiation, which comes about through disturbing radiation reaching the plastic stopper together with the identified ions. Such radiation consists of Bremsstrahlung, X-ray emission, and radiative electron capture, thus causing germanium crystals to be 'swamped' by undesirable and indistinguishable photons. The 'prompt flash' can thus prevent the system from effective detection of γ rays originating from the implanted ions. Therefore, it is essential to correct for intervals when germanium crystals are unresponsive to those incoming γ rays, which de-excite isomeric states:

$$f_1 = 1 - \frac{N_p}{N_{ion}N_c} \tag{4.8}$$

N_p counts the 'prompt events', i.e. the yield of a γ-ray peak of interest within the time period of the prompt flash, and N_c represents the number of active crystals.

f_2 – effective time of flight

Produced in the fragmentation at the entrance to the FRS, the ions spend approximately 300 ns to arrive at the final focal plane. There is a non-negligible probability that some of those populated in the isomeric state of interest will decay during this time of flight. Additionally, the ions are travelling at relativistic speeds, hence the rate at which they decay is affected and becomes smaller than it would if the ions would be at rest.

$$f_2 = e^{-\lambda_0(\frac{TOF_{1a}}{\gamma_{1a}}+\frac{TOF_{1b}}{\gamma_{1b}}+\frac{TOF_2}{\gamma_2})}. \tag{4.9}$$

Here, λ_0 accounts for the fact that the ion with a particular isomeric state is fully stripped:

$$\lambda_0 = \frac{ln2}{T_{1/2}}\sum_i^n(\frac{b_{ti}}{1+\alpha_{ti}}) \tag{4.10}$$

In the absence of atomic electrons those states de-exciting predominantly via internal conversion will thus have an effectively longer half-life compared to the conventional half-life, $T_{1/2}$. Therefore, all decay branches (with the respective branching ratios, b_{ti}, and conversion coefficients, α_{ti}) which could depopulate the isomer are indicated by summation.

The correction of relativistic velocities is expressed through sequential time of flights (TOF) through three sections of the FRS:

- between the production target and the scintillator placed in S2: TOF_{1a} and the corresponding Lorentz factor, γ_{1a}. These values are obtained by means of the LISE++ simulation package [18].

- between the scintillators placed in S2 and S4: TOF_{1b} and the corresponding Lorentz factor, γ_{1b}. Both of these values were measured in the experiment and cross-checked with LISE++.

- between the scintillator in S4 and the plastic stopper: TOF_2 and the corresponding Lorentz factor, γ_2. For calculation of these values, LISE++ was employed.

f_3 – γ-ray detection time window

Upon implantation of the incoming ions in the plastic stopper, an appropriate time window is to be chosen to detect the γ rays following de-excitation:

$$f_3 = e^{-\lambda t_i} - e^{-\lambda t_f}, \tag{4.11}$$

where

$$\lambda = \frac{ln2}{T_{1/2}} \tag{4.12}$$

The limits of such a window are denoted with t_i and t_f. Their absolute values are calculated relative to the time of implantation corresponding to $t = 0$, which is practically equal to the 'prompt flash'. Equation 4.9 suggests that the choice of detection limits follows from their comparison with the half-life, $T_{1/2}$.

f_4 – simply implanted vs. reacted particles

There is a finite probability that the passive plastic stopper at the final focal plane acts as a medium where a certain portion of the implanted ions can undergo tertiary nuclear reactions. This results in a loss of that reacted fraction from the total amount of ions identified preceding the implantation, N_{total}. Accordingly the correction factor f_4 addresses the fraction which did not react in the stopper, i.e. 'survived', $N_{survived}$:

$$f_4 = 1 - \frac{N_{destroyed}}{N_{total}} = \frac{N_{survived}}{N_{total}} \tag{4.13}$$

In practice this factor is estimated using simulations, quantifying both the reacted and simply implanted fractions by placing varying thicknesses of the plastic implantation material, i.e. plexyglass. For that matter, the mechanism of stopping of the tested ions in the plastic material has been examined using both the LISE++ simulation package as well as the SRIM software [53] thoroughly probing interactions of ions with matter. The congruent result would then define the approximate range of thicknesses to use in the analysis. For each value of thickness, a Monte Carlo calculation of transmission is performed and the unreacted fraction of ions after the implantation material is deduced. The reaction mechanism investigated here was primarily projectile fragmentation. Residual kinetic energy of ions is also noted because its value is decisive for the type of reaction between the projectile ions and the plastic material. This process is repeated iteratively until no ions could pass through the stopper for a chosen thickness. In order to account for other types of reactions eventually happening at lower energies, the numbers of particles reacted within a certain thickness were normalized to the stopping range.

4.3.3 Exemplifying Calculation of Isomeric Ratios

Before presenting a whole compilation of isomeric-ratio-calculation results for several selected nuclei, this section will exemplify the procedure and comment on the meaning of different values or factors.

For this purpose the nuclide ^{206}Hg is chosen. There are two previously reported isomers highlighted in the relevant decay scheme of the ^{206}Hg in Figure 4.11: at 3723 keV an $I^{\pi} = 10^{+}$ isomeric state and an $I^{\pi} = 5^{-}$ state at 2102 keV. For both isomers, two half-life measurements are reported in References [43, 44]: 92(8) ns and 112(4) ns as well as 2.15(21) μs and 2.09(2) μs, respectively.

In the current work the measured half-lives are found to be 106(15) ns and 2.08(4) μs for the isomers with $I^{\pi} = 10^{+}$ and $I^{\pi} = 5^{-}$, respectively. For more details on how exactly these values were extracted, see Section 4.3.1.

Based on the values obtained from this measurement and the values previously measured by Fornal *et al.* [43] and Steer *et al.* [44], new adopted weighted averages calculated for both isomeric states in ^{206}Hg are: $I^{\pi} = 10^{+}$, $T_{1/2} =$ 108(6) ns and $I^{\pi} = 5^{-}$, $T_{1/2} = 2.09(3)$ μs. These new adopted values are shown in Figure 4.11 and then used for the calculation of isomeric ratios.

Another important component for the presented calculation is branching ratios (cf. Equations 4.6 and 4.10). The values corresponding to the actual isomeric transitions were either determined from experimentally measured ratios of the related γ-ray intensities or quoted from literature. All exact values referring to the example case of ^{206}Hg are listed in Table 4.4. The level scheme of ^{206}Hg (see Figure 4.11) suggests that there are two decay branches depopulating the $I^{\pi} = 10^{+}$ isomer: an $E2$ γ transition of 100 keV and an $E3$ of 1257 keV. The corresponding branching ratios have been experimentally determined from the ratio of the γ-ray yields $I(1157)/I(1257)$ (see Table 4.4), where the 100 keV

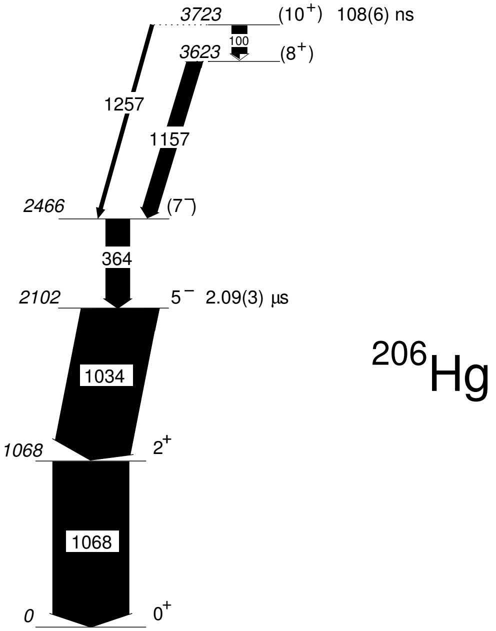

Figure 4.11: Experimental level scheme of ^{206}Hg. Relative γ-ray intensities observed in the delayed γ-ray spectra of this work are denoted by arrow widths. Both excitation energies and transition energies [42, 54] are expressed in keV. Half-life values are adopted values from the present analysis and previous experiments. Additionally, the spin and parity assignments are also indicated [42, 54].

transition was not measured itself, but instead its branch is represented by the succeeding 1157 keV line.

Both isomeric states have been taken into account and an overview of the variables inserted in Equation 4.5 is shown in Table 4.5.

The half-lives of the isomers are very different, which was carefully handled in the analysis (Section 4.3.1). The $I^\pi = 5^-$ isomeric state is fed by the decays of the $I^\pi = 10^+$ state and the start of the γ-ray detection time window related to it was chosen after many half-lives of the shorter-lived isomer. Such a choice has facilitated the isomeric-ratio calculation of the $I^\pi = 5^-$ state insofar as the feeding from the $I^\pi = 10^+$ isomer was simply subtracted.

The correction factor f_1 taking into account the 'prompt flash' was in both cases very close to unity.

The f_2 values were different for the two isomers, as they depend on the half-life of the isomeric state of interest (see Equations 4.9 and 4.10). For the short-lived

Table 4.4: Available branching ratios from literature and the values adopted for the calculation presented here for the $I^\pi = 10^+$ isomer in ^{206}Hg.

E_γ (keV)	$I_i^\pi \to I_f^\pi$	Study	$I(1157)/I(1257)$	b_t adopted (%)
1257	$10^+ \to 7^-$	Fornal *et al.* [43]	3.2(3)	
		Steer *et al.* [44]	3.5(5)	
		this work	3.0(2)	
		adopted	**3.1(2)**	**24(1)**

$I^\pi = 10^+$ isomer, $f_2 = 0.61(3)$, and the effective half-life was calculated to be $T_{1/2}^{eff} = 302(21)$ ns. The low-energy 100 keV transition depopulating this state is known to have a total conversion coefficient $\alpha_{tot} = 5.54(8)$ [51]. Consequently, for the fragments fully stripped of electrons, such a high probability for internal conversion brings about a significant increase in the effective half-life.

For the longer-lived $I^\pi = 5^-$ isomer, $f_2 = 0.931(4)$. This result suggests that a very large fraction of nuclei produced in this isomeric state actually does not decay in flight. Moreover, the effective half-life shows only a small increase to $T_{1/2}^{eff} = 2.15(15)$ μs.

The extracted factor taking into account the finite time window for recording the γ-ray spectrum, f_3, had a value of 0.772(27) and 0.345(2) for the $I^\pi = 10^+$ and $I^\pi = 5^-$ isomer, respectively.

Finally, the determination of the f_4 factor is based on simulations using another isotope, namely ^{202}Pb. Note, however, that the FRS settings for all Hg and Pb nuclei studied within the S429 experiment ensured that all entered the secondary target with $E \approx 160$ MeV/u. Hence, slowing down behaviour and tertiary reaction probabilities in the plastic stopper are considered the same. Therefore, the same value of correction factor f_4 was used for all isotopes studied. Considering the effect this factor has on the final value of isomeric ratios, it is absolutely necessary to understand its evaluation. In turn, it is decisive for the extraction of reliable $B(E2, 2^+ \to 0^+)$ values. Application of the method used to calculate this factor is demonstrated in Figure 4.12. A derived value of $f_4 = 0.86(2)$ suggested that 14% of all the implanted ions underwent tertiary nuclear reactions.

Table 4.5: Quantities relevant for the isomeric-ratio calculation of the isomers in ^{206}Hg. R_{exp} is derived from the f_1 to f_4 values and other observables in Equation 4.5. $T\lambda$ denotes multipolarity of a transition. Half-lives, $T_{1/2}$, and branching ratios, b_t, are adopted values from the present analysis and previous experiments, where applicable (see, e.g., Table 4.4). Excitation energies, E_x, γ-ray transition energies, E_γ, I_i^π, I_f^π and $T\lambda$. are taken from the ENSDF database [42]. See text for details.

E_x (keV)	$T_{1/2}$	E_γ (keV)	$I_i^\pi \rightarrow I_f^\pi$	$T\lambda$	α_{tot} [51]	b_t (%)	R_{exp} (%)
3723		100[a]	$10^+ \rightarrow 8^+$	$E2$	5.54(8)	76(1)	
3723	108(6)	1257	$10^+ \rightarrow 7^-$	$E3$	0.0083(1)	24(1)	4.4(6)
3623	ns	1157	$8^+ \rightarrow 7^-$	$E1$	0.00178(2)	76(1)	3.2(3)
2466		364	$7^- \rightarrow 5^-$	$E2$	0.061(1)	100	3.5(4)
						weighted average:	3.5(2)
2102	2.09(3)	1034	$5^- \rightarrow 2^+$	$E3$	0.0128(2)	100	34.2(18)
1068	μs	1068	$2^+ \rightarrow 0^+$	$E2$	0.00531(8)	100	32.4(18)
						weighted average:	33.2(13)
							29.7(13)[b]

[a] Unobserved γ-ray transition.

[b] Corrected for feeding from the $I^\pi = 10^+$ state.

4.3.4 Experimental Results

In the course of this experiment many nuclei known to have isomeric transitions were measured. The ones which are relevant for the present analysis are the two $A = 206$ nuclei, namely ^{206}Hg and ^{206}Pb as well as the three lighter lead nuclei ^{202}Pb, ^{200}Pb, and ^{198}Pb. In the previous sections the analysis procedure followed in order to extract the experimental isomeric ratios is established. The results of the ^{206}Hg analysis are incorporated in Section 4.3.3 as an example case. In the present section the results regarding the remaining nuclei of interest are expressed. Each nucleus is presented separately introducing the known level scheme reviewed to consider the results of this work, followed by the measured isomeric ratio table and the relevant γ spectra alongside the time decay curves relevant for the isomeric decay in question. In case that any of the analysis steps for a particular nucleus differs from the established method, an alternative approach is suggested and explained.

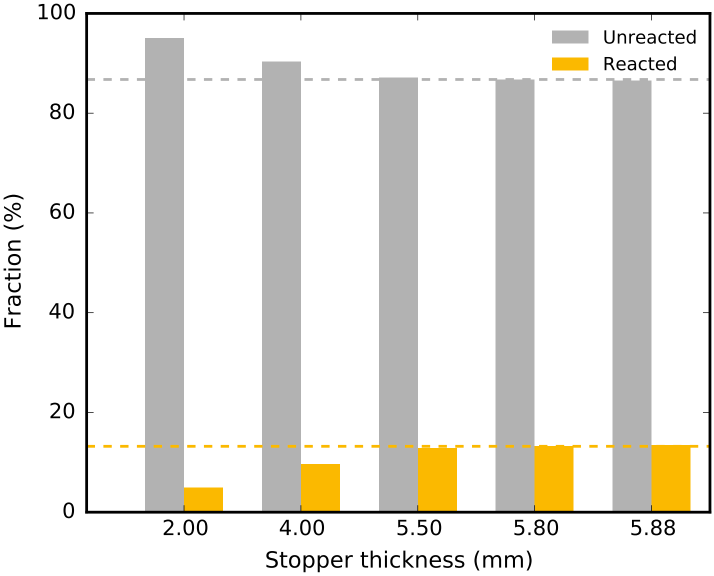

Figure 4.12: Fraction of ions unreacted and reacted in the plastic ($C_5O_2H_8$, $\rho = 1.2$ g/cm^3) stopper of varying thickness. Grey bars indicate the unreacted ions, whereas the light yellow bars show how many ions underwent tertiary reactions in the stopper. Dashed lines exhibit values of the same quantities but only for a fixed thickness equivalent to the evaluated stopping range of 5.77(5) mm (see Section 4.3.2 for more details).

^{206}Pb

Previous measurements reported in the literature confirm that there are two isomers in ^{206}Pb: an $I^\pi = 12^+$ state at 4027 keV and an $I^\pi = 7^-$ state at 2200 keV [54].

As the level scheme shown in Figure 4.13 suggests, the γ-ray transitions relevant for the decay of the $I^\pi = 12^+$ isomeric state are 1369 keV, 1299 keV, and 458 keV. The 69.7 keV, $12^+ \rightarrow 10^+$ transition is not observed in the present measurement. Moreover, such low-energy transitions are known to have worse time resolution than the higher-energy γ rays ('walk effect', see References [55, 56] for more details) which can deteriorate their detection probability and analysis relevance. It is also worth noting the influence of the 'prompt flash' (see Section 4.3.2) severely limiting what could be deduced from the low-energy part of the γ-ray spectra.

The half-life of the higher-spin $I^\pi = 12^+$ isomeric state has been measured from the combined decay curve of the 458, 1299, and 1369 keV transitions and

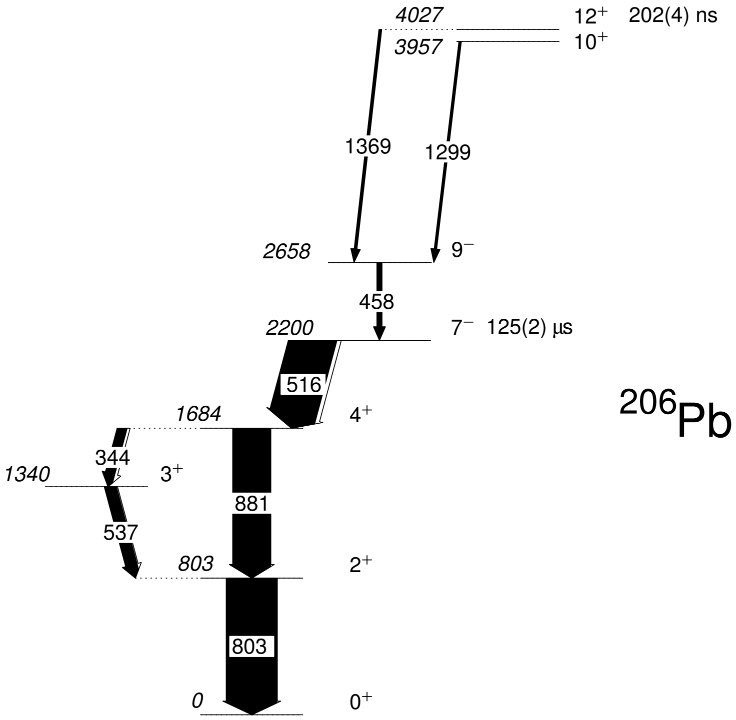

Figure 4.13: Experimental level scheme of ^{206}Pb. Relative γ-ray intensities observed in the delayed γ-ray spectra of this work are denoted by arrow widths. Both excitation energies and transition energies [42, 54] are expressed in keV. Half-lives, $T_{1/2}$, are adopted values from the present analysis and previous experiments. Additionally, the spin and parity assignments are also indicated [42, 54].

resulted in $T_{1/2} = 203(28)$ ns, as detailed in Paper V. This agrees well with the literature value of $T_{1/2} = 202(4)$ ns. The new adopted value is calculated as a weighted average of the two and amounts to $T_{1/2} = 202(4)$ ns. The lower-lying $I^{\pi} = 7^{-}$ isomeric state is much longer lived. The value for its half-life reported in the literature, $T_{1/2} = 125(2)$ μs, exceeds the limits of the experimental set-up employed for the present measurement. See Table 4.6 for the details relevant for the calculation of isomeric ratios. γ-ray yields were obtained from the energy spectra projected from the energy-time matrix for the time range appropriate for the investigated isomeric decay (see Figure 3 in Paper V).

Table 4.6: Quantities relevant for the isomeric-ratio calculation of the isomers in ^{206}Pb. R_{exp} is derived from the f_1 to f_4 values and other observables in Equation 4.5. $T\lambda$ denotes multipolarity of a transition. Half-lives, $T_{1/2}$, and branching ratios, b_t, are adopted values from the present analysis and previous experiments, where applicable (see, e.g., Table 4.4). Excitation energies, E_x, γ-ray transition energies, E_γ, I_i^π, I_f^π, and $T\lambda$ are taken from the ENSDF database [42]. See text for details.

E_x (keV)	$T_{1/2}$	E_γ (keV)	$I_i^\pi \to I_f^\pi$	$T\lambda$	α_{tot} [51]	b_t (%)	R_{exp} (%)
4027	202(4) ns	69.7[a]	$12^+ \to 10^+$	$E2$	33.7(25)	47(3)	
4027		1369	$12^+ \to 9^-$	$E3$	0.0078(1)	53(3)	1.3(3)
3957		1299	$10^+ \to 9^-$	$E1$	0.00163(2)	47(3)	1.2(3)
2658		458	$9^- \to 7^-$	$E2$	0.0364(6)	100	1.5(3)
						weighted average:	1.3(2)
2200	125(2) μs[b]	516	$7^- \to 4^+$	$E3$	0.089(1)	99.89(1)[b]	21.0(27)
1684		344[a]	$4^+ \to 3^+$	$M1$	0.296(5)	25(2)	
1684		881	$4^+ \to 2^+$	$E2$	0.00857(1)	75(2)	26.4(32)
1340		537	$3^+ \to 2^+$	$M1$	0.089(1)	25(2)	21.9(71)
803		803	$2^+ \to 0^+$	$E2$	0.0103(1)	100	24.9(27)
						weighted average:	23.7(16)
							22.4(16)[c]

[a] Unobserved or too weak γ-ray transition.

[b] Taken from ENSDF.

[c] Corrected for feeding from the $I^\pi = 12^+$ state.

^{202}Pb

Many isomeric states have been observed in ^{202}Pb. They are tabulated in detail in References [42, 57]. Data recorded for this isotope in the measurement described here shows evidence of the following isomeric states: $I^\pi = 19^-$, $I^\pi = 16^+$, and $I^\pi = 7^-$ with excitation energies $E_x = 5242 + y$, $4091 + x$ and 2208 keV, respectively. The corresponding partial decay scheme relevant for their consideration is shown in Figure 4.14.

Each of the three isomeric states listed above was subject of the half-life analysis as outlined in Section 4.3.1. After performing the fitting routine on the following decay curves: 797 and 1151 keV transitions for the $I^\pi = 19^-$ state, 853 keV transition for the $I^\pi = 16^+$, and 657, 422, and 961 keV for the $I^\pi = 7^-$, the extracted half-lives were: 105(38), 103(10), and 65(3) ns, respectively.

It is evident from the level scheme illustrated in Figure 4.14 that there is a very long-lived metastable state with excitation energy $E_x = 2170$ keV and

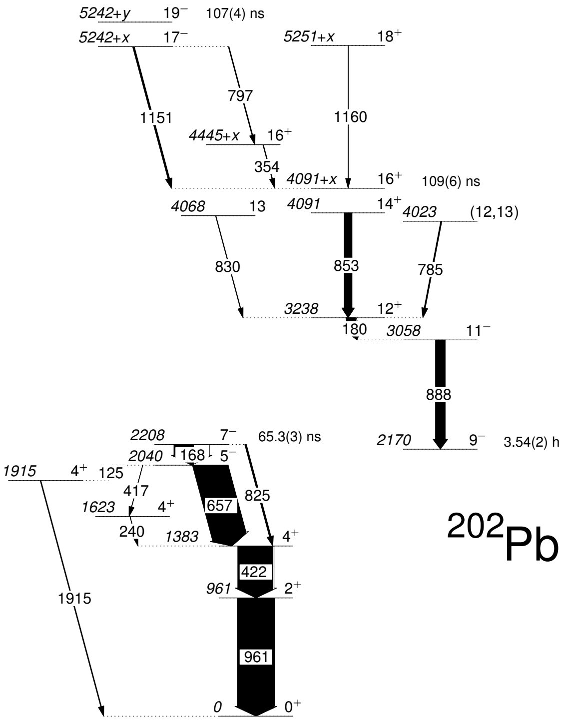

Figure 4.14: Experimental level scheme of ^{202}Pb. Relative γ-ray intensities observed in the delayed γ-ray spectra of this work are denoted by arrow widths. Both excitation energies and transition energies [42, 57] are expressed in keV. Half-lives, $T_{1/2}$, are adopted values from the present analysis and previous experiments. Additionally, the spin and parity assignments are also indicated [42, 57].

$T_{1/2}$ =3.54(2) h [42, 57]. This work could obviously not rely on the possibility to detect the decay of this state or any subsequent decays below this particular state. Nevertheless, some transitions lying below this long-lived state are observed (see, for example Table 4.7 and Paper V). Due to the distinctive population mechanism deployed in this study (see Chapter 3) all of the observed isomeric states were also directly populated, regardless of the feeding from the states above. This includes the yrast $I^\pi = 9^-$ state at 2208 keV.

It is worth noting that there are three γ-ray transitions with unknown transition energies as shown in Table 4.7. Moreover, there is an observed γ-ray transition with 168 keV, which was not included in the calculation of the isomeric ratio for reasons explained in the previous section.

Table 4.7: Quantities relevant for the isomeric-ratio calculation of the isomers in ^{202}Pb. R_{exp} is derived from the f_1 to f_4 values and other observables in Equation 4.5. $T\lambda$ denotes multipolarity of a transition. Half-lives, $T_{1/2}$, and branching ratios, b_t, are adopted values from the present analysis and previous experiments, where applicable (see, e.g., Table 4.4). Excitation energies, E_x, γ-ray transition energies, E_γ, I_i^π, I_f^π and $T\lambda$ are taken from the ENSDF database [42]. See text for details.

E_x (keV)	$T_{1/2}$	E_γ (keV)	$I_i^\pi \rightarrow I_f^\pi$	$T\lambda$	α_{tot} [51]	b_t (%)	R_{exp} (%)
$5242 + y$	107(4) ns	ϵ_1[a]	$19^- \rightarrow 18^+$	$E1$	$>> 1$[b]		
$5242 + y$		ϵ_2[a]	$19^- \rightarrow 17^-$	$E2$	$>> 1$[b]		
$5251 + x$		1160	$18^+ \rightarrow 16^+$	$E2$	0.00500(7)	8(2)	0.6(4)
$5242 + x$		797	$17^- \rightarrow 16^+$	$E1$	0.00380(6)	25(7)	1.0(4)
$5242 + x$		1151	$17^- \rightarrow 16^+$	$E1$	0.00195(3)	67(8)	0.5(1)
						weighted average:	0.5(1)
$4091 + x$	109(6) ns	x[a]	$16^+ \rightarrow 14^+$	$E2$	$>> 1$[b]		
4091		853	$14^+ \rightarrow 12^+$	$E2$	0.00913(13)	83(5)	2.6(3)
4068		831	$13 \rightarrow 12^+$	$(M1)$[c]	0.0286(5)	5(2)	3.6(20)
4023		785	$(12, 13) \rightarrow 12^+$	$(M1)$[c]	0.0332(5)	12(3)	2.6(9)
						weighted average:	2.7(3) 2.2(3)[d]
2170	3.54(2) h	787[e]	$9^- \rightarrow 4^+$	$E5$			
2208	65.3(3) ns	168	$7^- \rightarrow 5^-$	$E2$	0.797(12)	96(2)	
2040		657	$5^- \rightarrow 4^+$	$E1$	0.00550(8)	93(2)	9.5(13)
1383		422	$4^+ \rightarrow 2^+$	$E2$	0.0448(7)	98(2)	8.3(11)
961		961	$2^+ \rightarrow 0^+$	$E2$	0.0072(1)	100	9.3(12)
						weighted average:	9.0(7)

[a] Unobserved γ-ray transition with unknown transition energy.

[b] Decay by very highly converted low-energy transition, i.e. $f_2 = 1$ (no decay in flight in the FRS).

[c] Assumed multipolarity.

[d] Corrected for feeding from the $I^\pi = 19^-$ state.

[e] Unobserved γ-ray transition due to long half-life.

^{200}Pb

^{200}Pb is known to have a few isomeric states. The one with the highest energy has $E_x = 6948$ keV with the spin as high as $I^\pi = 25^-$ [58]. Its presence could not be confirmed from our data as the γ-ray transitions depopulating that state were not apparent in the γ-ray spectra. Therefore the analysis started from the next yrast isomeric state, $I^\pi = 19^-$ at 5076 keV, and comprised these other known metastable states: $I^\pi = 12^+$ at 3005 keV, $I^\pi = 9^-$ at 2183 keV, and $I^\pi = 7^-$ at 2154 keV. The corresponding partial decay scheme of ^{200}Pb is shown in Figure 4.15.

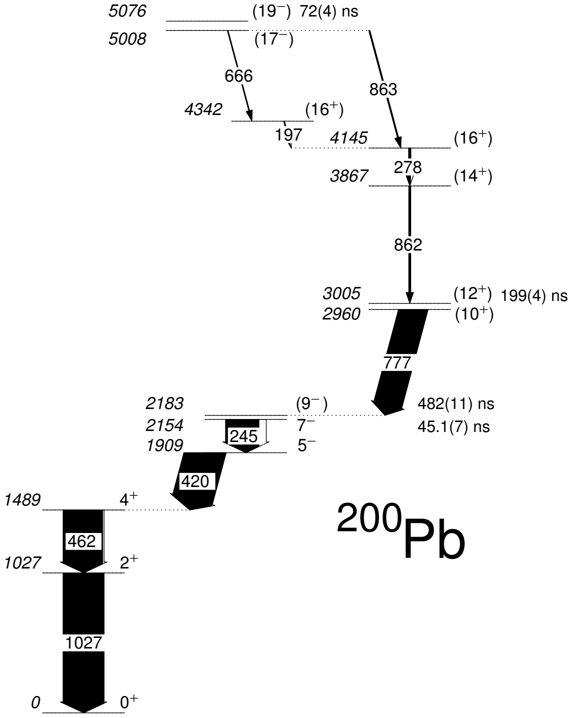

Figure 4.15: Experimental level scheme of ^{200}Pb. Relative γ-ray intensities observed in the delayed γ-ray spectra of this work are denoted by arrow widths. Both excitation energies and transition energies [42, 58] are expressed in keV. Half-lives, $T_{1/2}$, are adopted values from the present analysis and previous experiments. Additionally, the spin and parity assignments are also indicated [42, 58].

The half-lives of observed isomeric states at $I^\pi = 19^-$ and $I^\pi = 12^+$ were readily deduced from the standard procedure demonstrated earlier. The values obtained are $T_{1/2} = 87(18)$ ns and $T_{1/2} = 195(8)$ ns, respectively. These values are in good agreement with the ones from previous measurements: $T_{1/2} = 72(3)$ ns and $T_{1/2} = 199(3)$ ns [58], respectively. Note that the two γ-ray transitions $(17^-) \rightarrow (16^+)$ and $(14^+) \rightarrow (12^+)$ are very close in energy. They form a γ-ray doublet in the spectrum. Since this line represents the most intense signature of the $I^\pi = 19^-$ isomeric state decay, its time decay curve was fitted (see Section 4.3.1) to determine the half-life. As the level scheme suggests, the time projection of the 777 keV γ-ray transition was used to calculate the half-life of the $I^{\pi} = 12^{+}$ state. In both cases the γ-ray spectra were recorded for the same time range (see Figure 7 in Paper V).

The level scheme in Figure 4.15 suggests that there should be three low-energy γ-ray transitions of 68, 45.5, and 29.5 keV [42]. Similarly to previous examples of unobserved low-energy transition, these are considered neither in the time decay-curve analysis nor in the extraction of relevant values from the γ-ray spectra. Table 4.8 lists all the observables used in the analysis presented here.

Table 4.8: Quantities relevant for the isomeric-ratio calculation of the isomers in ^{200}Pb. R_{exp} is derived from the f_1 to f_4 values and other observables in Equation 4.5. $T\lambda$ denotes multipolarity of a transition. Half-lives, $T_{1/2}$, and branching ratios, b_t, are adopted values from the present analysis and previous experiments, where applicable (see, e.g., Table 4.4). Excitation energies, E_x, γ-ray transition energies, E_{γ}, I_i^{π}, I_f^{π} and $T\lambda$ are taken from the ENSDF database [42]. See text for details.

E^{*} (keV)	$T_{1/2}$	E_{γ} (keV)	$I_i^{\pi} \rightarrow I_f^{\pi}$	$T\lambda$	α_{tot} [51]	b_t (%)	R_{exp} (%)
5076		68^{a}	$(19^{-}) \rightarrow (17^{-})$	$E2$	36.2(5)	100	
5008	72(4) ns	666	$(17^{-}) \rightarrow (16^{+})$	$E1$	0.00537(8)	37(20)	0.6(5)
5008		863^{b}	$(17^{-}) \rightarrow (16^{+})$	$E1$	0.0033(1)	63(20)	
3867		862	$(14^{+}) \rightarrow (12^{+})$	$E2$	0.0089(1)	100	0.8(2)
						weighted average:	0.8(2)
3006	199(4) ns	45.5^{a}	$(12^{+}) \rightarrow (10^{+})$	$E2$	254(4)	100	
2960		777	$(10^{+}) \rightarrow (9^{-})$	$E1$	0.00399(6)	100	14.2(7)
							13.4(8)^{c}
2183.3	482(11) ns	29.5^{a}	$(9^{-}) \rightarrow 7^{-}$	$E2$	2140(50)	100	
2154		245	$7^{-} \rightarrow 5^{-}$	$E2$	0.21600(3)	100	35.7(16)
1909		420	$5^{-} \rightarrow 4^{+}$	$E1$	0.0139(2)	100	33.9(15)
1489		462	$4^{+} \rightarrow 2^{+}$	$E2$	0.0356(5)	100	32.0(14)
1027		1027	$2^{+} \rightarrow 0^{+}$	$E2$	0.00633(9)	100	31.0(14)
						weighted average:	32.9(7)
							19.5(10)^{d}

[a] Unobserved γ-ray transition.
[b] γ-ray doublet in the decay sequence of the (19^{-}) isomer.
[c] Corrected for feeding from the $I^{\pi} = (19^{-})$ state.
[d] Corrected for feeding from the $I^{\pi} = (12^{+})$ state.

It is worth noting that the $I^{\pi} = 9^{-}$ isomeric state is a member of a 'decay chain'. It is being populated by the decays of the preceding members, i.e. the metastable states at $I^{\pi} = 19^{-}$ and $I^{\pi} = 12^{+}$. Additionally, this particular sequence ends with the relatively short-lived $I^\pi = 7^-$ isomeric state which also needs to be taken into account. This dictates a different approach for the half-life determination as the relevant transitions express the shape of a multi-component exponential decay curve. In order to perform least-squares fitting of such a curve the Bateman equation is used for four successive exponential decays of a decay chain [59]:

$$\begin{gathered} A(t) = N_0 \sum_{i=1}^{4} (c_i e^{-\lambda_i t}) = \\ N_0 (c_1 e^{-\frac{ln2}{T_{1/2,1}} t} + c_2 e^{-\frac{ln2}{T_{1/2,2}} t} + c_3 e^{-\frac{ln2}{T_{1/2,3}} t} + c_4 e^{-\frac{ln2}{T_{1/2,4}} t}) \end{gathered} \tag{4.14}$$

Here, coefficients c_1 - c_4 are defined by:

$$c_m = \frac{\prod_{i}^{n} \lambda_i}{\prod_{i=1}^{n}{}' (\lambda_i - \lambda_m)} \tag{4.15}$$

The product in the denominator discards the term where $i = m$ which is designated by the prime. $A(t)$ is the activity at time t, N_0 denotes the initial number of nuclei populated in the respective isomeric state (enumeration 1 - 4 refers to the four isomers starting from the one with the highest spin $I^\pi = 19^-$ labelled with 1.) λ_i is the decay constant of the isomer labelled with i. Similarly $T_{1/2,i}$ represents the half-life of the i-th isomeric state.

The final fit function was therefore a sum of the four successive radioactive decays with three free parameters: an arbitrary offset to the time coordinate, a constant normalization term and the half-life of the $I^\pi = 9^-$, namely $T_{1/2,3}$. The half-lives of the first two isomeric states ($T_{1/2,1}$ and $T_{1/2,2}$ referring to the $I^\pi = 19^-$ and $I^\pi = 12^+$, respectively) used here are the ones obtained from this work, whereas the half-life of the final state in the sequence, $I^\pi = 7^-$, was the one available in the literature, $T_{1/2,4} = 45.1(7)$ ns.

The fit-evaluation criteria could be deduced in a manner analogous to the one presented for the simple exponential fit case (see Section 4.3.1 and Table 4.3). The sensitivity of the fit was tested against the first three criteria from Table 4.3. Since this new fitting routine does not treat the half-life of interest independently of the three other isomeric states, there is an additional constraint in the interpretation of the results: how much does the fit result vary by changing the half-lives of the three other states we considered known, fixed parameters in the fit. This consideration is important at the extreme values of the known half-lives, within their uncertainties.

Finally, when applying the new fitting routine to the combined time decay curve of the 420, 462, and 1027 keV transitions, the result this analysis suggests for the half-life of the $I^{\pi} = 9^{-}$ isomeric state is $T_{1/2} = 476(12)$ ns.
In order to settle the new adopted value of this particular half-life, the individual measurement's values compiled in [58] were contrasted with one another. Thereby it became evident that one out of eight literature values is very divergent [60], $T_{1/2}$= 424(10) ns, and thus compromises the resulting weighted average. Moreover, this is the only measurement available reporting the half-life value without the associated decay curve displayed in the original publication [60]. Therefore, this value was considered unreproducible and was neglected in the calculation of the new adopted weighted average which amounts to $T_{1/2}$ = 482(11) ns.

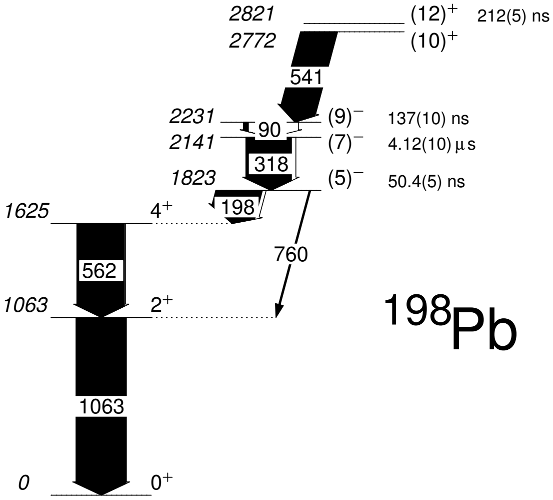

Figure 4.16: Experimental level scheme of ^{198}Pb. Relative γ-ray intensities observed in the delayed γ-ray spectra of this work are denoted by arrow widths. Both excitation energies and transition energies [42] are expressed in keV. Half-lives, $T_{1/2}$, are adopted values from the present analysis and previous experiments. Additionally, the spin and parity assignments are also indicated [42].

^{198}Pb

The highest-lying isomeric state confirmed from the present data has excitation energy E_x = 2821 keV and I^{π} = $(12)^{+}$. It was therefore considered a starting point for the analysis. The relevant partial decay scheme is shown in Figure 4.16. Besides this metastable state, the presence of the one at $E_x = 2141$ keV, $I^\pi = (7)^-$, was established on the basis of the recorded γ-ray spectra. The $I^\pi = (9)^-$ isomeric state at $E_x = 2231$ keV was only indirectly observed given the very low-energy γ-ray transition depopulating it. These three isomeric states form a decay chain in a manner analogous to the one demonstrated for ^{200}Pb. Therefore, the multi-component decay curve, which is a signature of the $I^\pi = (7)^-$ state decay, implies the presence of the $I^\pi = (9)^-$ isomeric state.

The half-life analysis performed for the $I^\pi = (12)^+$ state resulted in the value of $T_{1/2} = 212(10)$ ns. The 541-keV (see $(10)^+ \rightarrow (9)^-$ transition in Figure 4.16) decay curve was fitted following the simple method outlined in Section 4.3.1.

Since the lower-lying isomeric states are associated with a decay chain, the decay profile of the $I^\pi = (7)^-$ state has to be represented by a set of successive exponential decays detailed in Section 4.3.4, ^{200}Pb, and Equations 4.14 and 4.15. For that purpose, the combined decay curve of the transitions at 562 and 1063 keV was fitted using a three-step decay sequence. The partial half-lives considered as known were those of the preceding isomeric states, namely $I^\pi = (12)^+$ (this analysis) and $I^\pi = (9)^-$ (see References [42, 61]).

The $I^\pi = (5)^-$ state with $E_x = 1823$ keV is also reported to be of metastable character [61] with the half-life evaluated to be 50.4(5) ns. As suggested by the level scheme in Figure 4.16, two γ rays following its decay are expected to be recorded. The 760 keV γ-ray transition $(5)^- \rightarrow 2^+$ is too weak to be considered in both half-life and isomeric ratio analysis. The 198-keV transition $(5)^- \rightarrow 4^+$ has been detected. However, there are several reasons not to examine this transition within the presented analysis. It was already mentioned that low-energy transitions have worse time resolution than the higher-energy ones and that their detection might be hampered by the 'prompt flash'. Furthermore, energy-dependent detection efficiency has to be taken into account. Although this factor has been considered in the present analysis, the details of experimental set-up used for the related efficiency measurement (see Paper III) might have had penalizing effect on low-energy γ rays. Regardless of this work's missing direct evaluation of the $I^\pi = (5)^-$ isomeric state, it is evident from Figure 4.16 that it also falls under the same decay sequence as the states $I^\pi = (12)^+$, $I^\pi = (9)^-$, and $I^\pi = (7)^-$. Therefore, the half-life of $I^\pi = (7)^-$ state has also been computed by means of four successive exponential decays of a decay sequence, such as the one shown in Section 4.3.4 for ^{200}Pb. The final value for the half-life is a weighted average of the values obtained from three- and four-component exponential decay fits and equals 4.05(10) μs.

Table 4.9 illustrates the resulting isomeric ratios and indicates which transitions were not considered in the calculation.

For more detailed nuclear-structure consideration of this very isotope, in partic-

Table 4.9: Summary of the quantities relevant for the isomeric-ratio calculation of the isomers in ^{198}Pb. R_{exp} is derived from the f_1 to f_4 values and other observables in Equation 4.5. $T\lambda$ denotes multipolarity of a transition. Half-lives, $T_{1/2}$, and branching ratios, b_t, are adopted values from the present analysis and previous experiments, where applicable (see, e.g., Table 4.4). Excitation energies, E_x, γ-ray transition energies, E_γ, I_i^π, I_f^π and $T\lambda$ are taken from the ENSDF database [42]. See text for details.

E^* (keV)	$T_{1/2}$	E_γ (keV)	$I_i^\pi \to I_f^\pi$	$T\lambda$	α_{tot} [51]	b_t (%)	R_{exp} (%)
2821	212(5)	49.2[a]	$(12)^+ \to (10)^+$	$E2$	173.4(25)		
2772	ns	541	$(10)^+ \to (9)^-$	$E1$	0.00813(12)	100	18.5(10)
2231	137(10)	90[a]	$(9)^- \to (7)^-$	$E2$	9.98(14)		
	ns						
2141		318	$(7)^- \to (5)^-$	$E2$	0.097(1)	100	45.4(21)
1823	4.12(10)	198	$(5)^- \to 4^+$	$E1$	0.080(1)	97(1)	55.0(26)[b]
1625	μs	562	$4^+ \to 2^+$	$E2$	0.0223(4)	97(1)	44.9(21)
1063		1063	$2^+ \to 0^+$	$E2$	0.00591(9)	100	45.0(20)
					weighted average:		45.1(12)
							26.6(16)[c]

[a] Unobserved γ-ray transition.

[b] Not included in the average due to its low γ-ray energy. See text for details.

[c] Corrected for feeding from the $I^\pi = (12)^+$ state.

ular the surprisingly long half-life of the $I^\pi = (7)^-$ state, the reader is referred to Paper V.

4.3.5 Momentum dependence

Knockout reactions are recognized as very important probes in nuclear structure studies. There are well-known examples of the two-nucleon removal via direct reactions at relativistic energies in literature [62–64], which emphasize that the momentum distributions of the reaction residues provides a valuable insight in the reaction mechanism. A number of subsequent studies by E. C. Simpson *et al.* (see [8, 65, 66]) detail the extended theoretical formalism to treat momentum distribution in such reactions. Furthermore, they considered the residue momentum distributions with respect to the isomeric ratios and applied the formalism to heavy projectiles following the fragmentation of ^{208}Pb [67] and confronting the predictions with experimental results [44].

In this work, longitudinal momentum distributions of several Pb isotopes as residuals of the relativistic fragmentation are determined via the measurement of their x position at the intermediate S2 focus of the FRS. Since this study offers examples of multi-nucleon knockout reactions ranging from two to ten nucleons missing from the primary ^{208}Pb beam, determining the parallel momentum distribution shape is not straight-forward. The procedure to extract these distributions is outlined and applied to the extreme cases of multi-nucleon removal studied here, namely ^{206}Pb and ^{198}Pb. The results for the other Pb isotopes, ^{202}Pb and ^{200}Pb, are also presented.

As mentioned in Section 2.1.1, the S429 experiment made use of slits at S2, suppressing non-fragmented primary beam particles. The slit positions were set to -20 mm $< x <$ 20 mm. They thus impose a possible cut on the momentum distribution of the fragments by not necessarily transmitting the whole momentum distribution. This in turn can have an effect on the measured isomeric ratio [8], primarily when comparing experimental results with the theoretical calculations.

First, the total number of ions at the middle focal plane is recorded. Two examples of such a distribution are given in the uppermost row in Figure 4.17. The x-position measured at the middle focal plane, Δx, can be converted to parallel momentum of fragments, Δp, using

$$\frac{\Delta p}{p} = \frac{\Delta x}{D}, \tag{4.16}$$

where D stands for the dispersion constant arising from horizontal dispersion of the fragments at S2 [68]. Momentum of the fragments, p, is calculated using

$$p = B\rho, \tag{4.17}$$

where B represents the strength of the magnetic field in the second dipole of the FRS, and ρ is the radius of the ion's mean path.

Then, a 'γ-ray energy vs. x position' correlation matrix is created in order to select only the isomeric state of interest. At this stage, the same routine developed for the analysis outlined in Section 4.3.1 is deployed. The resulting position distribution for the 7^- isomer in ^{206}Pb is determined by summing up distributions in delayed coincidence with the γ rays at 516, 880, 537, and 803 keV (see the level scheme in Figure 4.13) and is shown in Figure 4.17(c). The resulting distribution for the 7^- state in ^{198}Pb, shown in Figure 4.17(d), is obtained as sum of distributions in delayed coincidence with γ rays at 318, 198, 562, and 1063 keV (see Figure 4.13). Finally, in order to investigate the isomeric ratio dependence on the momentum, the distributions in the middle row of Figure 4.17 are divided by the total number of respective ions, plotted in the uppermost row of Figure 4.17, giving rise to the results displayed in Figure 4.17(e) and (f).

Following the same method, distributions of the remaining isomeric states in Pb isotopes relevant for this work are deduced and illustrated in Figure 4.18.

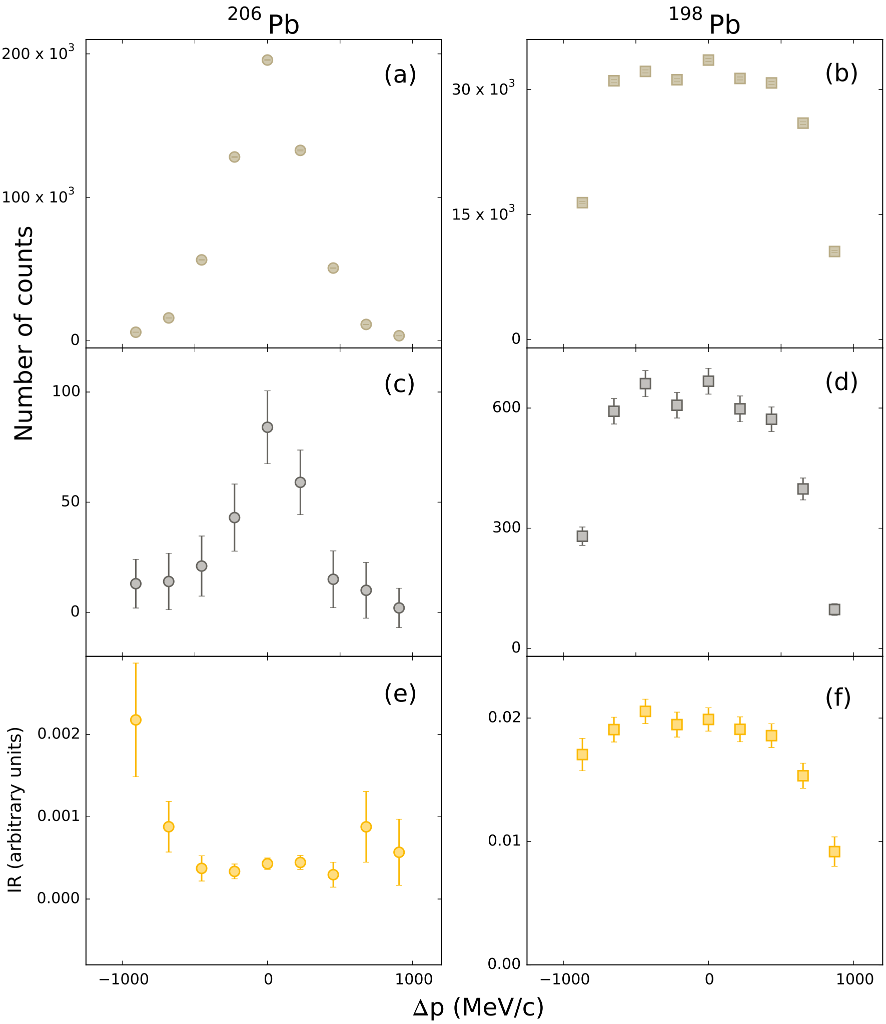

Figure 4.17: Illustrated procedure to obtain momentum-dependent isomeric ratios of the 7^- isomeric states in ^{206}Pb (three panels in the left column) and ^{198}Pb (three panels in the right column). Different symbols represent different nuclei. The same colour across the row serves to distinguish the type of spectrum. Panels (a) and (b) show parallel momentum distributions of the ^{206}Pb and ^{198}Pb ions, respectively. Panels (c) and (d) show the momentum distributions when applying the coincidence requirements for γ-ray transitions depopulating the 7^- isomeric states in ^{206}Pb and ^{198}Pb, respectively. Panels (e) and (f) are isomeric ratios in arbitrary units as a function of momentum transfer of the 7^- isomeric state in ^{206}Pb and ^{198}Pb, respectively. See text for details.

Panels (a) and (b) show distributions of the 12^+ isomeric state in ^{206}Pb and ^{198}Pb, respectively. Partial distributions obtained by delayed coincidence with γ rays at 1369, 1299, and 458 keV depopulating the 12^+ isomeric state in ^{206}Pb were considered. The respective level scheme is shown in Figure 4.13.

In case of ^{198}Pb, the only possible γ-ray gate was set on the 541 keV line (see Figure 4.16). The experimentally observed weakness of transitions depopulating the 19^- isomer in ^{202}Pb prohibits a meaningful momentum-dependence analysis of the isomeric ratio of that state. Hence, for ^{202}Pb the results for the two other isomeric states, namely 16^+ and 7^-, are shown in panels (c) and (d) in Figure 4.18. Delayed coincidence gates were set on 853 and 180 keV for the 16^+ isomer, and on 168, 657, 422, and 961 keV for the 7^- isomeric state.

The observed isomeric state with the highest spin in ^{200}Pb, 19^-, had to be omitted from the present analysis. Similar arguments as for the 19^- isomer in ^{202}Pb apply. Thus, panels (e) and (f) in Figure 4.18 correspond to the 12^+ and 9^- isomeric states in ^{200}Pb, respectively. Delayed coincidence gates on γ-ray energies used here were at 777 keV for the 12^+ state, as well as on 245, 420, 462, and 1027 keV for the 9^- isomer.

Reference [8] suggests that high-spin states in heavy projectiles, produced by a two-nucleon knockout, have wide momentum distributions. The total orbital angular momentum of the nucleon removed in the reaction is considered to affect the momentum distribution. These conclusions are based on the theoretical results following single-nucleon knockout [69], as well as the extended formalism describing two-nucleon removal [8]. See Reference [65] for more details. Furthermore, the application of the nucleon knockout model to heavy mass projectiles has thus far shown a good agreement with experimental results [67] only in cases where one or two nucleons were removed. All nuclei considered in this work are of interest for the nucleon knockout formalism as they provide a range of examples of multi-nucleon removal. Despite this, detailed theoretical discussions of this matter are beyond the scope of this thesis.

Similar to the findings presented in Reference [67] for the reaction $^{208}\mathrm{Pb} \rightarrow {}^{206}\mathrm{Hg}$, direct removal of two neutrons in case of $^{208}\mathrm{Pb} \rightarrow {}^{206}\mathrm{Pb}$ to the 12^+ high spin isomeric state, the parallel momentum distribution is expected to be very wide. Panel (a) in Figure 4.18 suggests that the isomeric ratio increases at both extremes of the distribution, experimentally governed by the position of the slits. It is also apparent that the isomeric ratio is close to zero around the zero momentum transfer. The distribution for the 7^- isomeric state of ^{206}Pb, see Figure 4.17(e), may or may not exhibit the same trend towards the higher edge of the distribution. Whether this is an expected behaviour or an artefact would require a more detailed investigation related to the exact population mechanism of this state.

The other extreme case of nucleon removal in the present experiment is ^{198}Pb

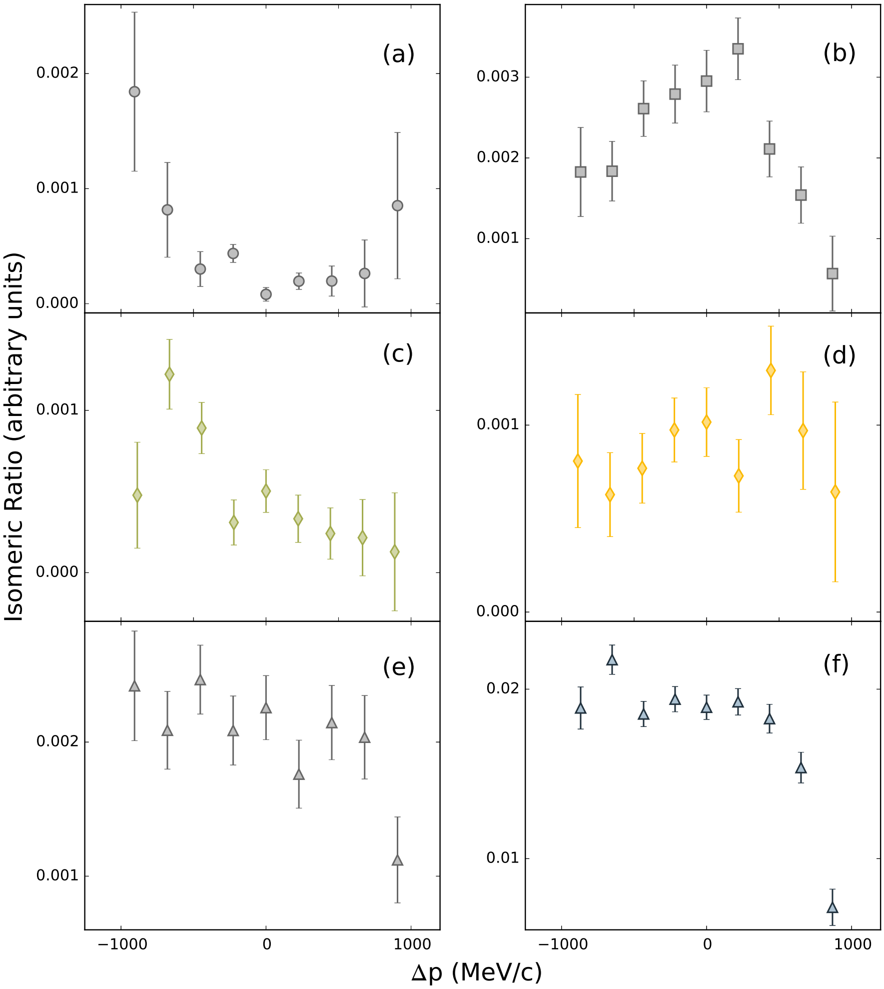

Figure 4.18: Isomeric ratios arising from the procedure exemplified in Figure 4.17 for other isomeric states in Pb nuclei discussed in the present work. Different symbols represent different nuclei and different colours show different isomeric states. Panels (a) and (b) correspond to the 12^+ isomeric state in ^{206}Pb and ^{198}Pb, respectively. Panels (c) and (d) show the isomeric ratio distribution of the 16^+ and 7^- states in ^{202}Pb, respectively. Panels (e) and (f) show the isomeric ratio distribution of the 12^+ and 9^- states in ^{200}Pb, respectively.

which has ten neutrons less than the doubly-magic ^{208}Pb primary beam. Since there are ten valence holes in ^{198}Pb, there are many possibilities for pairs of these particles to couple and produce an excited state of certain angular momentum. These configurations are briefly discussed in Chapter 5 with respect to shell-model calculations of the Pb isotopes. The parallel momentum distributions of the two isomeric states observed in ^{198}Pb, 7^- and 12^+, are shown in Figure 4.17(f), and Figure 4.18(b), respectively. The shapes of these distributions are very different than those representing the isomeric states with the same spins in ^{206}Pb. This observation is in line with the assumed different reaction mechanism in this case of multi-nucleon removal.

The two remaining Pb isotopes considered in the present analysis do not seem to exhibit specific or recognizable patterns in the shape of their respective momentum distributions. They are illustrated in Figure 4.18(c)-(f). Most of the distributions are rather flat, possibly with an exception seen in panel (c) representing the 16^+ high-spin state of ^{202}Pb. The trend observed here does not truly follow those of the other high-spin isomeric states such as, for instance, in Figure 4.18(a) ($I^\pi = 12^+$ in ^{206}Pb) and Figure 2 of Reference [67]. However, increasing values of isomeric ratios are observed towards the lower edge of the distribution in Figure 4.18(c). In order to attribute this to the assumptions presented earlier, more detailed theoretical considerations are required.

Chapter 5

Data Interpretation

5.1 The Nuclear Shell Model

Nuclear physics experiments performed in the first half of the 20^{th} century revealed that certain nuclei show greater stability than other nuclei. These findings led to the development of the *nuclear shell model* [70], which resembles the atomic shell model: a shell filled with given numbers of protons or neutrons yields enhanced stability. The maximum number of nucleons required to fill a shell is determined by the so-called *magic numbers* (Z or N = 2, 8, 20, 28, 50, 82, as well as N = 126, 184). Nuclei with magic nucleon numbers are more tightly bound than both their neighbours. This observation of the binding energy deviating from the predictions of empirical mass formula lays out the basic principle for the shell-model development.

Analogously to the atomic shell model, the arrangement of nucleons in shells is governed by the Pauli principle, so that each nucleon has a specific set of quantum numbers describing its motion, i.e the energy eigenstates (see for example [1]): total angular momentum, j, orbital quantum number, ℓ, and number of nodes of radial wave function, n. A nucleus with a magic number of either protons or neutrons is often referred to as a *magic nucleus*, whereas a *doubly-magic nucleus* has a magic number of both nucleon types. In a similar manner as within an atom, *orbitals*, also known as *subshells*, form shells. In addition to the gaps associated to the magic numbers previously listed, certain subshell gaps might appear: for instance, Z =40 or Z =64 also show somewhat enhanced stability for specific numbers of neutrons [1].

It is due to a strong, attractive force that the nuclei are bound together inside the nucleus. This nuclear force clearly needs to overcome the repulsive Coulomb interaction between positively charged protons and be short-range in nature. In order to study the nuclear levels and their spacing, the potential responsible for the short-range nuclear force, $V(r)$, needs to be modelled realistically. In practice, this description starts from an average potential with a 'transitional' shape between the simple harmonic-oscillator potential and the square well potential. One of the realistic choices - the *Woods-Saxon* potential, though it could be solved only numerically, takes the form

$$V(r) = -\frac{V_0}{1 + e^{(r-R)/d}} \tag{5.1}$$

where R stands for the *nuclear radius* and d for the *skin thickness*. Their values are empirically deduced from numerous fits using the Woods-Saxon distribution. If a potential of the Woods-Saxon form is taken as an ansatz for numerically solving the three-dimensional Schrödinger equation, the resulting energy levels and their ordering are shown in Figure 5.1. However, the suggested scheme does not reproduce experimentally observed magic numbers apart from 2, 8, and 20. Therefore, a spin-orbit coupling term $\alpha(\vec{l} \cdot \vec{s})$, is added to the nuclear potential, giving rise to the total angular momentum, $\vec{j} = \vec{l} + \vec{s}$, of a given orbital. The spin quantum number, $s = 1/2$, takes either the negative or positive value, $m_s = \pm 1/2$, of the s projection. Thanks to this modification, the shell model successfully reproduces the experimentally found magic numbers. This is illustrated in the right panel of Figure 5.1.

The model could be further confronted with experimental findings regarding the binding energies and ground-state nuclear spins. Total nuclear spin, I, is a result of all individual nucleons coupling their $\vec{j}_i$ momenta together. For a nucleus with filled orbitals, all the substates of I are filled, leaving the total angular momentum equal to zero. If a nucleus has only one nucleon outside the last filled shell or one nucleon missing to fill the shell, the so-called *valence* particle or hole, I would take the value of angular momentum, $\vec{j}$, carried by that odd particle or hole. This consideration is based on an assumption of single-particle independent motion, which is in accordance with experimental data, preferably in case of odd-A nuclei. It is important to note that this single-particle interpretation considers that a nucleon individually moves in the mean field, expressed through an external potential, created by all the other nucleons. In practice, the one-particle states corresponding to such simplified potentials are deduced. By solving the Schrödinger equation for one nucleon, single-particle wave functions and eigenenergies, *single-particle energies*, are obtained. Finally, the solution of the many-nucleon Schrödinger equation is then a product of single-particle wave functions.

However, nuclei often have more than one valence nucleon or hole. The current work exemplifies only such multi-valence hole nuclei, ^{206}Pb being the one with least number of valence holes, with respect to the doubly-magic core ^{208}Pb (Z = 82, N = 126). Therefore, the single-particle approach described thus far, i.e.

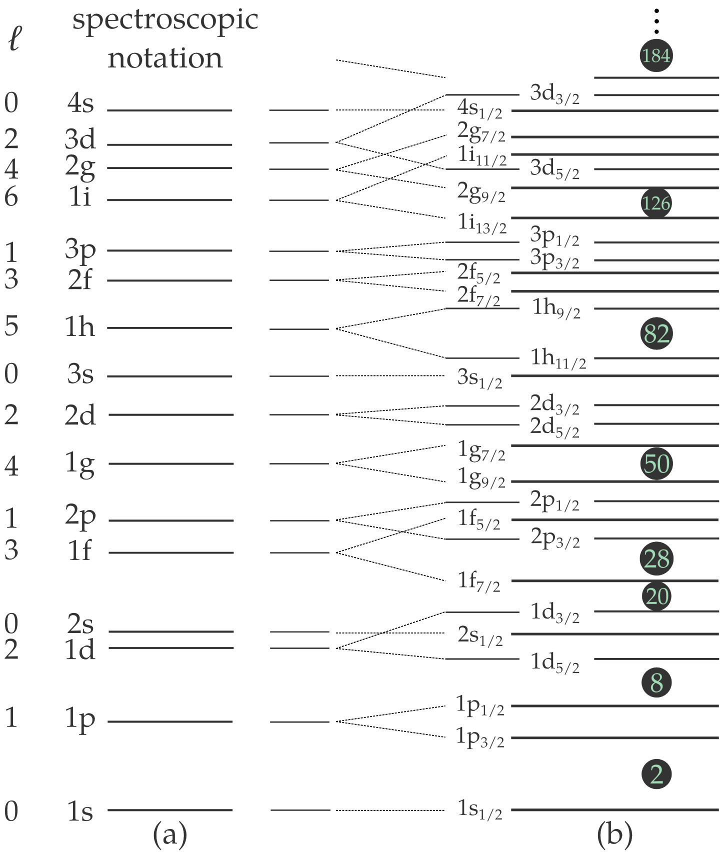

Figure 5.1: Ordering of the energy levels in the shell model. (a) Solving the Schrödinger equation with the Woods-Saxon potential results in the unsplit levels. The orbital quantum numbers, ℓ, are indicated. (b) Adding the spin-orbit coupling term to the potential used in (a), causes splitting of the levels. Each split level is denoted by quantum numbers nlj and the level multiplicity or occupancy is calculated as $2j+1$. Magic numbers are indicated by circled numbers. Adapted from [59].

treating nucleus as an assembly of non-interacting nucleons in a mean-field potential, does not suffice. Instead, the nucleons (or holes) interact with each other via the so-called residual interaction, which also needs to be modelled properly. Within the usual shell-model description, those are typically considered to be of two-body type, expressed by two-body matrix elements (TBME).

There are different ways of treating the residual interaction, which might depend on the region of nuclei studied. Within the shell model, one often refers to configuration mixing as a consequence of the residual interaction. In other words, nucleon configurations change because of the valence nucleons interactions. For instance, if one considers two valence nucleons, their interaction can lead to a scattering to the subshells which are different to the ones they were originally occupying. The theoretical description needs to account for all of the configurations resulting in the same total angular momentum, I^π. Finally, for given quantum numbers I and π only a few discrete states of lowest energy are of interest in discrete γ-ray spectroscopy.

5.2 NuShellX South-West of ^{208}Pb

The shell-model calculations presented in the current work were performed using the NuShellX code [71]. The primary model space of the present calculations comprises the ^{208}Pb core and neutron holes to be distributed amongst the following orbitals: $h_{9/2}$, $f_{7/2}$, $f_{5/2}$, $p_{3/2}$, $p_{1/2}$, $i_{13/2}$. An illustration of this valence model space is shown in Figure 5.2.

The single-particle energies and the relevant TBMEs are derived from interactions suitable for the model space used. Two interactions were chosen for the present study: one is referred to as 'pbpop' and the other as 'khhe'.

The former is suited for the nuclei with atomic numbers ranging from $Z = 58$ to $Z = 114$ and neutron numbers from $N = 100$ to $N = 164$. It was derived by Poppelier and Glaudemans [72] and in contrast to the valence space proposed above, neutron holes could not be placed in $h_{9/2}$ and $f_{7/2}$ orbitals. However, the 'pbpop' calculations can include particle-hole excitations, probing not only neutrons, but proton contributions as well. In the particular case of the ^{208}Pb core, two protons are allowed to be excited across the otherwise closed $Z = 82$ shell.

The 'khhe' interaction is the excitation recommended for the part of nuclear chart of interest. It is the Kuo-Herling interaction [73] and is viable for nuclei whose atomic numbers are in the range from $Z = 50$ to $Z = 82$ and with neutron numbers ranging from $N = 82$ to $N = 126$. The orbitals available for the calculation are all those listed above and displayed in Figure 5.2. That model space, representing the complete set of basis for the calculation, is labelled 'default' in the further text. In some cases, however, restricting the model space could be more time-effective and reduces the size of matrices to be diagonalized. More details about such restrictions applied to this work are listed in Section 5.3.

5.3 Probing Truncation Schemes

The cases when only certain combinations of nucleons are allowed in orbitals are incorporated in the calculation by truncating the model space. Several truncation schemes were deployed for both interactions probed. Their characteristics are presented in Table 5.1. Graphical representations of the principal truncated model spaces used for the 'khhe' interaction are shown in Figure 5.2. It is obvious that certain truncation schemes are equivalent for different interactions. Note that ID = 2 relies on the exact same active orbitals as the ID = 5, as well as the equivalence of ID = 15 and ID = 4 (Table 5.1). Moreover, the schemes labelled as 'tr-f10' and 'tr-f10M' are based on the same model space. However, the four diagonal 0^+ TBME within the 'tr-f10M' scheme, corresponding to the $f_{5/2}$, $p_{3/2}$, $p_{1/2}$, $i_{13/2}$ orbitals, are modified according to $TBME' = TBME + (N - 126) \cdot 50\ keV$. Consequently, there is an additional 100 keV binding per each even-even Pb isotope moving away from the ^{208}Pb core.

The model space with ID = 1 is not indicated in Table 5.1. It implies a different type of excitation. This scheme is implemented within the 'pbpop' interaction and it allows two protons and two neutron holes to be excited across the $Z = 82$ shell closure, therefore denoted by '2p-2h'.

Table 5.1: Truncation schemes used in shell-model calculations. Two different interactions and their respective model spaces are presented through the occupancy of neutron orbitals. Filled orbitals are indicated by 'x', whereas the checkmark stands for the ones to be filled without restrictions.

interaction	truncation ID	name	$h_{9/2}$	$f_{7/2}$	$f_{5/2}$	$p_{3/2}$	$p_{1/2}$	$i_{13/2}$
pbpop	2	default	x	x	✓	✓	✓	✓
	15	pbpop-10	x	x	✓	✓	✓	≥ 10
khhe	8	default	✓	✓	✓	✓	✓	✓
	9	tr-8	≥ 8	≥ 6	✓	✓	✓	✓
	10	tr-8a	≥ 8	≥ 6	✓	✓	✓	≥ 10
	11	tr-8b	≥ 8	≥ 6	✓	✓	✓	≥ 11
	12	tr-8c	≥ 8	≥ 6	≥ 4	✓	✓	≥ 10
	13	tr-8d	≥ 8	≥ 6	≥ 4	≥ 2	✓	≥ 10
	14	tr-8e	≥ 8	≥ 6	≥ 4	≥ 2	✓	≥ 11
	7	tr-9(a)	≥ 9	≥ 7	✓	✓	✓	≥ 10
	6	tr-9b	≥ 9	≥ 7	≥ 4	≥ 2	✓	≥ 11
	5	tr-f	x	x	✓	✓	✓	✓
	4	tr-f10	x	x	✓	✓	✓	≥ 10
	3	tr-f10M[a]	x	x	✓	✓	✓	≥ 10

[a] Modified 0^+ TBME. See text for details.

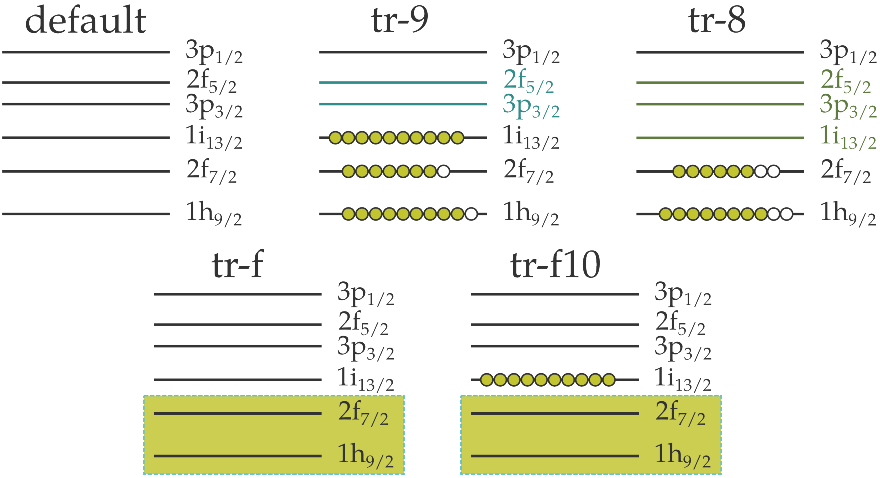

Figure 5.2: Illustration of the neutron orbitals within the model space used by the 'khhe' interaction and included in the NuShellX shell-model calculations. 'default' stands for the configuration containing the complete set of states as defined by the interaction. Other configurations represent the truncated model spaces. See Table 5.1 for a detailed list of all truncations used. The neutron occupancy in orbitals is indicated by the minimum number of neutrons. For $1h_{9/2}$ and $2f_{7/2}$ holes are drawn to indicate the neutrons required to fill the subshell. Orbitals where no neutrons are indicated are 'open', i.e. there is no explicit confinement in placement of neutrons. Encircled orbitals are full and no neutrons can be placed there. 'tr-9' and 'tr-8' have a number of sub-truncation schemes, listed in Table 5.1 and the orbitals relevant for these are indicated by a lighter colour.

In order to test and interpret the complexity and sensitivity of the calculation, several parameters deduced by the NuShellX code need to be clarified. Here, the dimensions in the schemes used in the calculation, $D(J)$ and $D(M)$, as well as the number of partitions are considered. The values are summarized in Tables 5.2 and 5.3.
Although technical, they stem from the quantum mechanical nature of the many-body problem and the approach to obtain the corresponding wave function. As stated, a set of quantum numbers determining each single-particle wave function is (nlj), where each value of the total angular momentum, j, has $(2j+1)$ projections, the m-states. There are different approaches to construct the basis states and two will be mentioned here:

- m-scheme: the basis is composed of eigenstates of J_z, i.e. the z projection of the total angular momentum J. Even though J_z is, J is not necessarily a good quantum number, unless the basis is composed of the complete set of states. In this scheme, the dimension, $D(M)$ is defined as the total number of states for a given J.

- J-scheme: the angular-momentum coupling of the individual wave functions is taken into account. From the details of the calculation [74] and for symmetry reasons [75], in this approach J is a good quantum number. Moreover, the dimension of the calculation, $D(J)$, is reduced in comparison to the $D(M)$, as the dimension of the Hamiltonian matrix is reduced.

Truncated basis shell-model calculations were carried out for all even-even Pb isotopes west from the doubly-magic ^{208}Pb. Since NuShellX uses both the m-scheme and the coupled J-scheme, the results of their respective dimensions are compiled in Table 5.2. The listed values relate to the 0^+ state in each Pb isotope for all truncation schemes introduced earlier. As expected, the dimensions increase rapidly as more holes are introduced with respect to the inert core, ^{208}Pb. See the trend for each truncation scheme across the columns in Table 5.2. Furthermore, the difference in dimensions in the J- and m-scheme is more and more prominent for nuclei further away from the doubly-magic core. With dimensions increasing for certain truncation schemes (see ID in range 6-14) the program is not calculating the values any more [76]. However, this does not necessarily mean that the shell-model calculation would not be performed, but the computing time to reach convergence could be questionable. This is observed for ^{200}Pb and ^{198}Pb. As soon as the full configuration restrictions are placed upon the neutron single particle orbitals $h_{9/2}$ and $f_{7/2}$, i.e. 'blocking' them (see ID = 3-5 in Table 5.1 and Figure 5.2), the program is calculating dimensions again.

The results for ^{206}Pb and ^{204}Pb in model spaces denoted by ID = 2, 15 and ID = 3-5 are the same. This is expected as there are only two and four neutron holes for ^{206}Pb and ^{204}Pb, respectively, to be distributed amongst the same number of active orbitals of the same kind.

Table 5.2 suggests very different dimensions for ID = 1 compared to all other truncation schemes. This is sensible, since this is the only model space which allows excitation of both neutron holes and protons.

There is another 'measure' of the complexity of the calculation, namely the number of *partitions*. A partition is a specific distribution of the available nucleons amongst the allowed set of single-particle orbitals. The number of partitions is calculated by the program taking into account the total number of particles which could be placed in a certain orbital, $2j + 1$, and any other restrictions posed by the basis set. The neutron partitions in case of different truncated model spaces are shown in Table 5.3.

It is worth noting that the numbers of partitions for different truncation schemes applied to ^{206}Pb and ^{204}Pb are very similar. As stated above, certain truncation

Table 5.2: Dimensions of the calculations. For each nucleus, the ground state, 0^+, is considered and the $D(J)$ and $D(M)$ are specified, respectively.

inter-action	truncation		nucleus				
	ID	name	^{206}Pb	^{204}Pb	^{202}Pb	^{200}Pb	^{198}Pb
pbpop	2	default	4 33	23 1004	154 13130	706 81273	1975 262147
	1	2p-2h	1620 180191	5014 7317962	601130 103771482	3462080 666891873	10646879 2193105537
	15	pbpop-10	4 33	23 1004	141 11767	450 47722	581 66547
khhe	8	default	6 92	159 9427	4346 411184	[a]	[a]
	9	tr-8	6 92	149 8931	3404 332062	[a]	[a]
	10	tr-8a	6 92	149 8931	3379 328947	[a]	[a]
	11	tr-8b	6 92	147 8876	3196 307140	[a]	[a]
	12	tr-8c	6 92	146 8852	3194 316735	[a]	[a]
	13	tr-8d	6 92	145 8833	3145 313823	[a]	[a]
	14	tr-8e	6 92	143 8778	2962 292016	[a]	[a]
	7	tr-9a	4 83	88 5942	1418 144821	[a]	[a]
	6	tr-9b	4 83	82 5789	1111 115399	[a]	[a]
	5	tr-f	4 33	23 1004	154 13130	706 81273	1975 262147
	4	tr-f10	4 33	23 1004	141 11767	450 47722	581 66547
	3	tr-f10M	4 33	23 1004	141 11767	450 47722	581 66547

[a] Dimensions cannot be calculated by the NuShellX program yet [76].

schemes are equivalent for different interactions. Additionally, one can explain the similar partition numbers by relatively small numbers of neutron holes in these two nuclei which could be distributed amongst the fixed number of orbitals.

Table 5.3: Complexity of the calculations. For each nucleus, the respective number of neutron partitions is specified.

interaction	truncation ID	truncation name	nucleus ^{206}Pb	^{204}Pb	^{202}Pb	^{200}Pb	^{198}Pb
pbpop	2	default	10	31	60	86	101
	1	2p-2h	10	31	60	86	101
	15	pbpop-10	10	31	56	67	56
khhe	8	default	21	120	400	974	1919
	9	tr-8	21	108	291	535	757
	10	tr-8a	21	108	285	482	569
	11	tr-8b	21	107	270	427	466
	12	tr-8c	21	102	232	301	232
	13	tr-8d	21	96	186	186	96
	14	tr-8e	21	95	171	141	51
	7	tr-9a	19	79	175	251	251
	6	tr-9b	19	66	83	41	6
	5	tr-f	10	31	60	86	101
	4	tr-f10	10	31	56	67	56
	3	tr-f10M	10	31	56	67	56

If the 'pbpop' interaction is used with the truncation scheme '2p-2h', the distribution of protons should also be taken into account. In this particular case, the number of proton partitions is 6.

One could also consider the dependency of the average occupation of neutrons in active orbits with different truncation schemes. This relationship is displayed in Figure 5.3.

The results presented for three excited states, 2^+, 9^-, and 12^+, show a rather constant trend of orbital occupancy while considering different model spaces. Small fluctuations are visible for the lowest excited state presented in Figure 5.3, namely in case of the $s_{1/2}$ orbital.

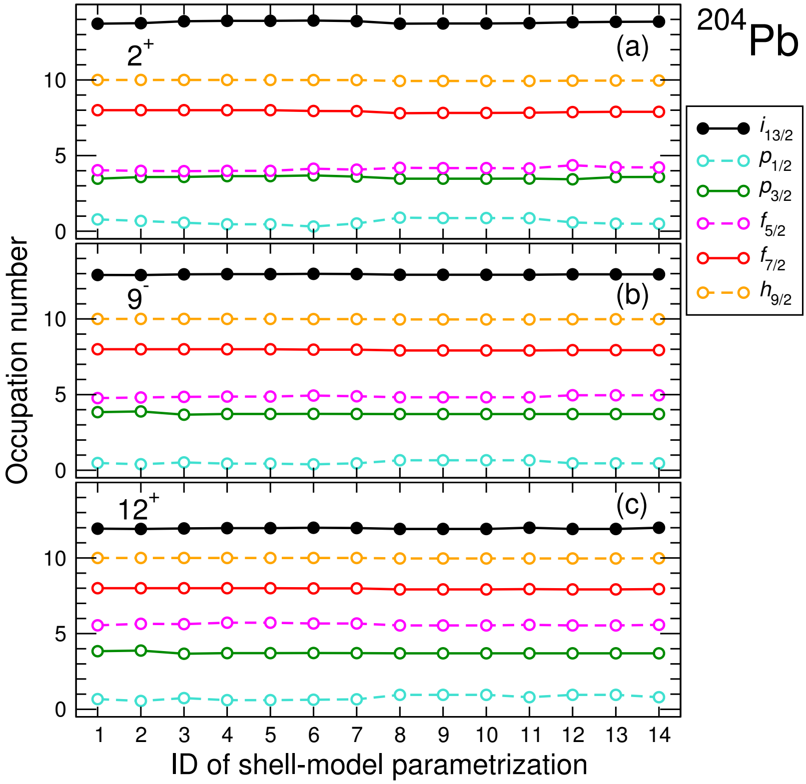

Figure 5.3: Shell-model calculation results for ^{204}Pb neutron (ν) occupancy in orbitals within the model space employed (see Figure 5.2). The relationship between the occupation number and different truncation schemes listed in Table 5.1 is displayed for the following states: (a) the first 2^+, (b) 9^-, and (c) 12^+. Note, however, that the truncation scheme with ID = 15 is not included in the figure, for its results for ^{204}Pb are equivalent to those obtained for ID = 2.

Chapter 6

Concluding Remarks on Isomers

Choosing the combination of relativistic fragmentation as the primary and Coulomb excitation as the secondary reaction to investigate nuclear properties is known to be a probe sensitive to the state of nucleus produced after the primary reaction. Isomeric ratio values indicate which portion of the nucleus produced can undergo Coulomb excitation. The current study suggests the importance of experimentally measured isomeric ratios for reaction mechanism responsible for production of secondary fragments. Although considered in previous studies (see, for instance, Paper IV), this fact has not been widely exploited in the context of relativistic fragmentation of multi-nucleon removal, since primarily aiming to deduct new nuclear structure information.

Theoretical predictions of nucleon-removal have not considered many examples of heavy nuclei as secondary products, i.e. residues. A two-proton removal from the ^{208}Pb beam has already been contrasted to the theoretical reaction model successfully [67]. Very recently, the formalism has been applied to the two-neutron removal, $^{208}\text{Pb} \rightarrow {}^{206}\text{Pb}$, in order to compare it with the experimental results of this work (see Paper V). Experimentally deduced isomeric ratios prove to be a valuable input for theoretical reaction models. Extending the formalism to the isomers in nuclei even further away from the doubly-magic ^{208}Pb is a challenge. Nevertheless, this work provides a number of experimental isomeric ratios which were previously not reported. Thus, if applicable, theoretical predictions could benefit from these examples to be tested upon.

In addition to the isomeric ratio dependency on the longitudinal momentum of fragments (discussed in Section 4.3.5), the relationship of isomeric ratios and mass of the fragment offers insight into the population probability of the fragmentation reaction. The latter is summarized in Figure 6.1.

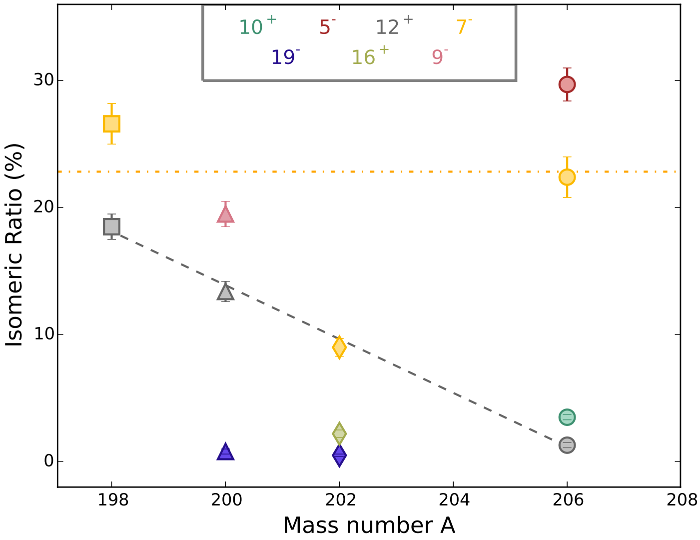

Figure 6.1: Summary of the measured isomeric ratios resulting from the current study. Total angular momenta, i.e. spins, of the considered isomeric states are described in the legend. Different nuclei represented by their mass numbers, A, are assigned different symbols, much as those presented in Figure 4.18. Note, however, that both ^{206}Hg and ^{206}Pb are displayed with the same symbol. The values corresponding to 12^+ isomeric states are connected with the dashed line to guide the eye. Horizontal dotted line indicates the average value of 7^- states in ^{198}Pb and ^{206}Pb, and the 9^- state in ^{200}Pb. See Tables 4.5 - 4.9 as well as Table 1 in Paper V for more details.

Figure 6.1 suggests an increase in isomeric ratio of the 12^+ state with an increasing number of neutron holes. In a very simplified picture, one could attribute this increase to many more possibilities to populate the state of interest with an increased number of valence holes available.

An apparent trend is missing for other isomeric states. The lower spin states tend to have isomeric ratios independent on the mass number, possibly all having values in the region $\sim$ IR $= 20 - 30\%$. Therefore, the dotted horizontal line is drawn in Figure 6.1 and shows the average value of the isomeric ratios referring to the following states: 7^- in both ^{198}Pb and ^{206}Pb, and 9^- in ^{200}Pb. However, a deviant value for the 7^- in ^{202}Pb is obvious. This nucleus is a particular case, due to its significantly longer-lived 9^- isomeric state ($T_{1/2} = 3.54$ h compared to the 7^- having $T_{1/2} = 65.3$ ns). The corresponding half-life and isomeric ratio could not be deduced from the experiment described here. With this in mind, one may assume that the sum of the 9^- and 7^- isomeric ratios for this particular nucleus can have a value close to the one indicated by the dotted line in Figure 6.1.

In the course of this work, large-scale shell-model calculations were performed across the even-even members of the neutron-deficient part of the Pb isotopic chain, starting with ^{206}Pb and up to ^{198}Pb. The technicalities of the investigation are summarized in Chapter 5 and the results are presented in Paper V. All the previously reported isomeric states that have been measured in the current study have been successfully reproduced by the calculations. Paper V also suggests a new structural input regarding the surprisingly long half-life of $I^{\pi} = (7)^{-}$ state in ^{198}Pb.

Chapter 7

3D-Imaging with Scintillation Detectors

The significance of γ-ray imaging concepts can be best appreciated by perceiving its numerous applications: they range from tumour diagnosis and therapy to homeland security, de-mining of antipersonnel land-mines, void inspection within structural materials or safety surveillance, to name but a few. This ever-growing interest to observe and clearly understand (γ-radioactive) matter hidden from direct sight is also present in the field of basic nuclear physics research [77, 78].

To achieve γ-ray imaging of the incoming radiation, the first goal is to locate a single interaction point of a γ ray in radiation detectors. For that purpose, a stack of scintillation detectors arranged in a matrix is to be deployed in order to determine the direction of the interacting γ rays through the recorded energy deposition.

This Chapter presents a concise overview of the Compton imaging principles and outlines the most important parts of the simulation code developed. After discussion of the first results, a plan for future developments is considered.

7.1 Method

Locating the source of γ-ray radiation is the first step towards the image reconstruction, or three-dimensional imaging. Given the energy of photons, the underlying Compton scattering mechanism allows for the source location determination. In effect, whenever a first interaction point of an event contributes to a Compton scattering sequence, the event is selected. The scattering angle is then computed from the amount of energy transferred to the detector medium.

$$1 - \cos\theta = \frac{\Delta E}{E_\gamma E_f} \cdot m_e c^2 \tag{7.1}$$

for

$$E_f = E_\gamma - \Delta E \tag{7.2}$$

Therefore:

$$\theta = \arccos\left(1 - \frac{m_e c^2 \Delta E}{(E_\gamma)^2 - E_\gamma \Delta E}\right) \tag{7.3}$$

θ is the scattering angle, ΔE the energy deposited, E_γ is the energy before scattering and E_f the energy after scattering. The scattering sequence described here is illustrated in Figure 7.1. It suggests that the origin of the primary quantum can be determined to lie somewhere on a conical surface. In three-dimensional space, a particular event could have originated from any direction, as long as it forms an angle θ with the scattered direction.

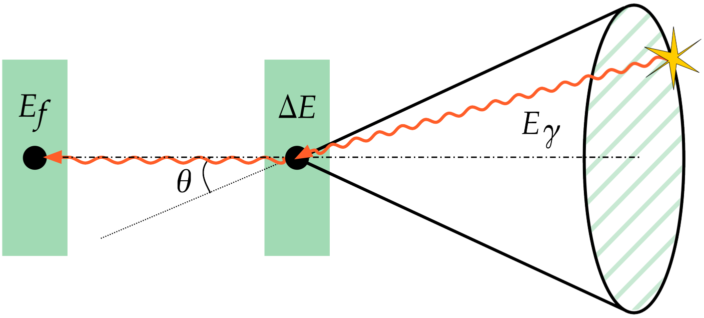

Figure 7.1: The simplest scenario of multiple Compton scattering sequence. The radiation source is indicated by a star on a base of cone, since there is no unambiguous solution for its determination. Instead, all possible locations form a distribution on a conical surface.

Any γ-ray source reconstruction algorithm based on this principle is viable only if several scattering events are observed from the same radiation source. Each of these events would then form a different cone, namely a cone surface of ambiguity. With an assumption that all these events do originate from the same source, the intersection of these cones should be a single point, i.e. *the source of the γ-ray radiation*. Applicability of this simple back-projection approach is mentioned in Section 7.2.3 and Paper I.

7.2 Simulations

7.2.1 Preparation Considerations

During the preparation stage of the original version of the project reviewed here, different combinations of scintillation materials and readout technologies have been evaluated. These first simulations aimed to find the solution with the optimal response in terms of energy resolution, integrity, ruggedness and cost efficiency. Scintillation materials considered, both plastic and inorganic, were BC-404, BC-408, BC-428, NaI(Tl), CsI(Na), CsI(Tl), and $LaBr_3$(Ce), coupled to the readout schemes of either photomultiplier tubes (PMTs) or the more recently developed Silicon Photomultipliers (SiPMs) [79]. As a result, CsI(Na), CsI(Tl), and BC-404 were chosen as the materials to be implemented in more-detailed simulations, initially being read out by position-sensitive PMT's and upgraded to SiPMs if applicable.

7.2.2 Geant4

Paper I outlines the virtual implementation of the intended experimental set-up in the Geant4 toolkit [80]. Two different geometries are considered. Both follow the same set-up scheme proposed earlier, i.e. a matrix constructed out of single scintillation detectors shaped as bars, where the light-sensitive readout components, predominantly PMTs, were glued on their ends. The use of the inorganic scintillation material, CsI(Na), is expected to facilitate the results of the simulated experiment mainly due to higher detection efficiency. The light yield specified in the simulations is 41 photons/keV, the wavelength for the maximum intensity of emitted light 420 nm, and the absorption length 33 cm. The developed simulation code provides the input data for the offline analysis briefly discussed in Section 7.2.3.

7.2.3 Data Analysis

In Section 7.1 the principle of Compton imaging is discussed through an example of a two-hit event: The incoming γ-ray photon scatters off one detector element from the proposed array of scintillator bars and then it is photo-absorbed in the second detection element. The reconstruction of the possible origin of the γ-ray source can be traced back (see Paper I and references therein).

First results shown in Figures 2 and 3 in the same contribution suggest that the determination of the common origin of γ radiation is not trivial in practice. One of the main reasons can be the need for much higher statistics. Such a set-up also relies on very precisely measured energies in order to deduce the positions. The finite precisions induce uncertainties in geometrical characterization of each probability distribution cone. Finally, the back-projection approach should be followed for different two-dimensional planes in order to deduce the point of cones' intersection.

7.3 Preparation of Experimental Tests

The virtual implementation of the experimental set-up is able to disentangle all the interaction points in an event, mostly due to multiple Compton scattering sequences. Empirically, the three spatial coordinates of each point are recorded through the readout scheme: x- and y-coordinate directly, and z from the timing differential measurement. In this particular case, PMTs are mounted on both ends of a scintillator bar, hence the processing of their signals safely allows to use 'left-right' timing information.

7.3.1 Scintillators and PMTs

During R&D stage of the project, a compact demonstrator is to be built. It is planned to deploy $20 \times 20 \times 100$ mm^3 bars of inorganic scintillation materials with reasonably good energy resolution, coupled with either two photomultiplier tubes (PMTs) at the ends, or a number of novel Silicon photomultipliers (SiPM) along the crystals. The SiPM components comprise little matter, such that many of these can be positioned at one, two, or all four sides of a scintillator crystal bar. Practically they do not disturb the paths of the γ rays. The small dimensions of the SiPM allow thus for rather compact packing, which is of crucial importance in light-mechanical design. Furthermore, they are very attractive new candidates in photo sensors, with promising time jitter characteristics for measurements with high timing resolution.
Based on the simulations, the initial geometry chosen for the demonstrator comprises the larger bars simulated in the geometry one. See Paper I for details on the two geometries. Moreover, a third geometry was proposed: it includes two crossed layers of three to five of the larger bars each in front of a 100×100 mm^2 wall of 25 existing LYCCA [10] CsI(Tl)-PD scintillators [81]. This implementation was chosen as the second candidate for the demonstrator and is depicted in Figure 7.2.

7.3.2 Electronics and Data Acquisition

The maximum number of detector channels requires two 16-channel cards for the 25 LYCCA detectors, one 16-channel card for (a subset of) SiPMs, and a fourth 16-channel card for PMT processing (geometry depicted in Figure 7.2). A full suite of such a 64-channel data acquisition based on standard electronics

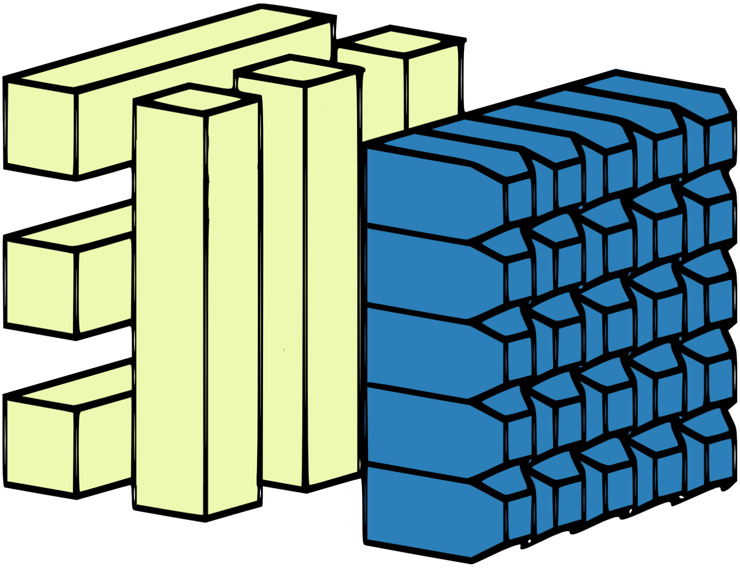

Figure 7.2: A possible demonstrator geometry employing existing LYCCA-type CsI detectors to form a highly efficient wall (blue). Position sensitive CsI(Tl) or CsI(Na) bars are indicated in light green. For the sake of clarity of the scheme, the PMTs are omitted on both ends of the detector bars.

would be very expensive. Therefore, a so-called 'digital FEBEX system' [82] is proposed, which directly records the pulses from the detectors, i.e. being much more cost-effective while digitising more direct information. In brief, the SiPMs will be processed by custom-made LYCCA-type preamplifiers with a range 0-10 MeV, read-out by GSI-EE 14-bit 50 MHz sampling ADC self-triggering FEBEX cards. It should be noted that such a signal-processing scheme is also useful for future experiments within the FAIR-NUSTAR environment.

Appendix A

Not to forget about an AGATA experiment

The following overview refers to a few software-related points which the author considers important for AGATA data taking and processing. The terminology here requires basic understanding of AGATA set-up and might depend on nuances, due to the complexity of data processing.

- Always save AGATA raw data, the so-called *traces*. Their typical file extension is **cdat**. However, there is another file format of essentially identical information, namely **bdat**, which is deprecated. Therefore, it is more convenient to configure the raw-data recording to be formatted as the former.

- Do invest time in setting up software for displaying *local* spectra online. This does not need to include spectra from all actors acting on individual crystals. However, the *Producer* spectra are an absolute minimum. In case that the NARVAL emulator, *femul*, is configured to write these spectra, consult the local data-acquisition team to understand the possible effect on the dead time of the system.

- At the stage of 'almost nearline analysis' or better yet 'immediately after online data taking', it is important to make a *global* replay of the data. In other words, all the data recorded by individual crystals need to be processed by one or more *global* actors. Knowing that the information recorded by individual crystals is transformed in *events* at this stage, it is important to determine the time window within which data recorded from different crystals will be considered. Additionally, it is very convenient to write spectra of single crystals typically processed by the last actor at the *local* level, *Post PSA*. In this way, one could see how adjusted the data from individual crystals were right before being processed at the *global* level.

- In physics experiments, either a few or a whole ensemble of ancillary detectors are deployed. Their data is recorded by a separate data stream and converted to the AGATA data format. It might be challenging to merge the AGATA and the ancillary data online. Usually, once AGATA data is written by a *global* actor, it is *merged* with the data from the ancillary system.
- The GammaWare software [83] is most often configured to process merged data and format it in such a way that a preliminary nearline analysis can be readily performed. But GammaWare can also be used for monitoring purposes while taking data, that is the libraries known as *Watchers* which show different spectra in real time.
- As mentioned above, the ancillary data also need to be written in the AGATA data format. Therefore, it can be very valuable to know how the transformation from the ancillary data format to the AGATA data format is made in practice, and vice versa. Moreover, if there are (slightly) different converters for performing this action online and offline, one should be aware of those.

Appendix B

Towards the AGATA data refinement

Notes on a few calibration aspects:

- Check the energy calibration of the segments and the cross-talk coefficients on the crystal level.
- If there are missing/broken segments (maximum 2), correct for them.
- Check that the cross-talk correction is properly done on the level of each individual detector, in other words that the coefficients generated by the automatic correction procedure are indeed reasonable.
- Choice of the parameter combination should be based on comparison of the spectra from Figure 4.5. But beforehand make sure that there is no significant difference between the energy read out by the core and the segment sum.

References

[1] R. F. Casten, *Nuclear Structure from a Simple Perspective* (Oxford Univ. Press, 1990).

[2] G. D. Dracoulis, P. M. Walker, and F. G. Kondev, Rep. Prog. Phys. **79**, 076301 (2016).

[3] G. Audi et al., Chin. Phys. C **36**, 1157 (2012).

[4] H. Geissel et al., Nucl. Instr. Meth. Phys. Res. B **70**, 286 (1992).

[5] S. Akkoyun et al., Nucl. Instr. Meth. Phys. Res. A **668**, 26 (2012).

[6] N. Pietralla et al., EPJ Web of Conferences **66**, 02083 (2014).

[7] P. G. Hansen, Phys. Rev. Lett. **77**, 1016 (1996).

[8] E. C. Simpson, Ph.D. thesis, University of Surrey (2009).

[9] A. Giaz et al., Nucl. Instr. Meth. Phys. Res. A **729**, 910 (2013).

[10] P. Golubev et al., Nucl. Instr. Meth. Phys. Res. A **723**, 55 (2013).

[11] P. Spädtke et al., Nucl. Instr. Meth. Phys. Res. B **139**, 145 (1998).

[12] W. Henning, Nucl. Phys. A **538**, 637 (1992).

[13] F. Ameil et al., GSI Scientific Report 2011, **2012-1**, 171 (2012).

[14] M. L. Cortes et al., GSI Scientific Report 2013, **2014-1**, 117 (2014).

[15] V. Hlinka et al., Nucl. Instr. Meth. Phys. Res. A **419**, 503 (1998).

[16] A. Stolz et al., Phys. Rev. C **65**, 064603 (2002).

[17] R. Hoischen, Ph.D. thesis, Lund University (2009), ISBN 978-91-7473-090-6.

[18] O. Tarasov and D. Bazin, Nucl. Instr. Meth. Phys. Res. B **376**, 185 (2016).

[19] F. Beck, *Proceedings of the Conference on Physics from Large γ-ray Detector Arrays*, LBL-35687, CONF-940888, UC-413 **2**, 154 (1994).

[20] J. Eberth et al., Prog. in Part. Nucl. Phys. **28**, 495 (1992).

[21] J. Eberth et al., Nucl. Instr. Meth. Phys. Res. A **369**, 135 (1996).

[22] J. Simpson et al., Acta Physica Hungarica. New series, Heavy ion physics **11**, 159 (2000).

[23] D. Habs et al., Prog. in Part. Nucl. Phys. **38**, 111 (1997).

[24] D. Ralet et al., Nucl. Instr. Meth. Phys. Res. A **786**, 32 (2015).

[25] A. Lopez-Martens et al., Nucl. Instr. Meth. Phys. Res. A (2017), *to be submitted.*

[26] B. Bruyneel, B. Birkenbach, and P. Reiter, Eur. Phys. J. A **52**, 70 (2016).

[27] R. Venturelli and D. Bazzacco, LNL Annual Report p. 220 (2004).

[28] S. Paschalis et al., Nucl. Instr. Meth. Phys. Res. A **709**, 44 (2013).

[29] T. Lauritsen et al., Nucl. Instr. Meth. Phys. Res. A **836**, 46 (2016).

[30] J. Eberth et al., AIP Conf. Proc. **656**, 349 (2003).

[31] R. Venturelli et al., LNL Annual Report p. 156 (2002).

[32] B. Bruyneel et al., Nucl. Instr. Meth. Phys. Res. A **599**, 196 (2009).

[33] B. Bruyneel et al., Nucl. Instr. Meth. Phys. Res. A **608**, 99 (2009).

[34] A. Pullia et al., IEEE Transactions on Nuclear Science **58**, 1201 (2011).

[35] M. Bellato et al., IEEE Transactions on Nuclear Science **55**, 91 (2008).

[36] *A library of services to decode/encode data through the Agata Data Flow* (2007), URL `http://agata.in2p3.fr/doc/ADF_DesignProposal.pdf`.

[37] I. Kojouharov et al., GSI Scientific Report 2008, **2009-1**, 235 (2009).

[38] D. Bazzacco, Nucl. Phys. A **746**, 248 (2004).

[39] A. Lopez-Martens et al., Nucl. Instr. Meth. Phys. Res. A **533**, 454 (2004).

[40] D. Weisshaar et al., Nucl. Instr. Meth. Phys. Res. A **847**, 187 (2017).

[41] T. Hüyük, Ph.D. thesis, University of Valencia (2017), *to be published.*

[42] *Brookhaven National Laboratory. National Nuclear Data Center, ENSDF* (2017), URL `http://www.nndc.bnl.gov/ensdf/ensdf/ensdf.jsp`.

[43] B. Fornal et al., Phys. Rev. Lett. **87**, 212501 (2001).

[44] S. J. Steer et al., Phys. Rev. C **84**, 044313 (2011).

[45] M. Bowry et al., Phys. Rev. C **88**, 024611 (2013).

[46] M. Pfützner et al., Phys. Rev. C **65**, 064604 (2002).

[47] S. Steer, Ph.D. thesis, University of Surrey (2008).

[48] M. Bowry, Ph.D. thesis, University of Surrey (2013).

[49] R. Brun and F. Rademakers, Nucl. Instr. Meth. Phys. Res. A **389**, 81 (1997).

[50] T. Kibédi et al., Nucl. Instr. Meth. Phys. Res. A **589**, 202 (2008).

[51] *BrIcc v2.3S Conversion Coefficient Calculator* (2017), URL `http://bricc.anu.edu.au/index.php`.

[52] Z. Podolyák et al., Nucl. Phys. A **722**, C273 (2003).

[53] J. F. Ziegler, M. Ziegler, and J. Biersack, Nucl. Instr. Meth. Phys. Res. B **268**, 1818 (2010).

[54] F. Kondev, Nuclear Data Sheets **109**, 1527 (2008).

[55] G. Knoll, *Radiation Detection and Measurement* (Wiley, 2000).

[56] *Principles and applications of timing spectroscopy*, URL `http://www.ortec-online.com/service-and-support/library/application-notes`.

[57] S. Zhu and F. Kondev, Nuclear Data Sheets **109**, 699 (2008).

[58] F. Kondev and S. Lalkovski, Nuclear Data Sheets **108**, 1471 (2007).

[59] K. S. Krane, *Introductory Nuclear Physics* (Wiley, 1987).

[60] B. Fant et al., Nucl. Phys. A **475**, 338 (1987).

[61] X. Huang and M. Kang, Nuclear Data Sheets **133**, 221 (2016).

[62] D. Bazin et al., Phys. Rev. Lett. **91**, 012501 (2003).

[63] J. A. Tostevin et al., Phys. Rev. C **70**, 064602 (2004).

[64] J. A. Tostevin and B. A. Brown, Phys. Rev. C **74**, 064604 (2006).

[65] E. C. Simpson et al., Phys. Rev. C **79**, 064621 (2009).

[66] E. C. Simpson et al., Phys. Rev. C **80**, 064608 (2009).

[67] E. C. Simpson et al., Phys. Rev. C **82**, 037602 (2010).

[68] *FRS ion optics* (2017), URL `https://web-docs.gsi.de/~weick/frs/frs-ion-optics.html`.

[69] J. A. Tostevin, Eur. Phys. J. **150**, 67 (2007).

[70] M. G. Mayer, Phys. Rev. **74**, 235 (1948).

[71] B. Brown and W. Rae, Nuclear Data Sheets **120**, 115 (2014).

[72] N. A. F. M. Poppelier and P. W. M. Glaudemans, Z. Phys. A **329**, 275 (1988).

[73] E. K. Warburton and B. A. Brown, Phys. Rev. C **43**, 602 (1991).

[74] B. A. Brown, *Lecture Notes in Nuclear Structure Physics* (NSCL-MSU, 2005).

[75] C. Qi, Rom. Journ. Phys. **60**, 782 (2015).

[76] B. A. Brown, private communication.

[77] J. Gerl et al., Nucl. Instr. Meth. Phys. Res. A **525**, 328 (2004).

[78] R. Speller et al., Nucl. Instr. Meth. Phys. Res. A **457**, 653 (2001).

[79] J. Gerl, private communication.

[80] S. Agostinelli et al., Nucl. Instr. Meth. Phys. Res. A **506**, 250 (2003).

[81] T. Almqvist, Bachelor Thesis, Lund University, 2015.

[82] J. Hoffman et al., GSI Scientific Report 2011, **2012-1**, 253 (2012).

[83] *GammaWare online HTML documentation* (2017), URL `http://www.ipnl.in2p3.fr/gammaware/doc/html`.

Scientific publications

Paper I

Simulations for position-sensitive tracking of γ rays in scintillators
Approach for source reconstruction

N. Lalovic[*1,2], *J. Gerl*[1], *D. Rudolph*[2], *R. Hoischen*[1], *and P. Golubev*[2]
[1]GSI, Darmstadt, Germany; [2]Lund University, Lund, Sweden

Introduction

There is a growing demand to localize the single interaction point of γ rays in radiation detectors. This is relevant not only in the basic research sector, but even more in societal and industrial applications, such as medical imaging, environmental and safety investigations. Scintillation materials with position-sensitive read-out are viable candidates for this purpose and have been tested using Geant4 simulation toolkit [1].

Geant4 Simulations

The present simulation code enables easy and quick optimization of different geometries. Detailed simulations were performed with both BC404 and CsI(Na) scintillators. Here we present results with the latter detector elements, providing higher efficiency. Energy response and associated light production of the initial radiation (γ rays) has been investigated, hence including all the underlying physics processes. In addition, optical photons have been treated, with an assumption that the surface was a perfectly polished mirror. So far, $511\,keV$ e^+e^- annihilation radiation has been considered. First geometry simulated comprises $9 \cdot 18 \cdot 18 \cdot 100\,mm^3$ scintillator bars with Hamamatsu R7600U-2000 PMTs with $2\,mm$ distance between each 2 crystal elements in the 'matrix', as represented in Fig 1. The second geometry included $9 \cdot 4 \cdot 9 \cdot 9 \cdot 100\,mm^3$ scintillator bars with Hamamatsu R7600U-2000M4 PMTs with $2\,mm$ between 'submatrix' elements and $4\,mm$ between 'matrix' elements.

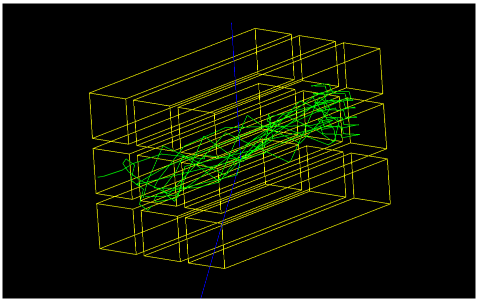

Figure 1: Geometry 1

Analysis and Reconstruction Algorithm

We are interested in multiple Compton scattering [2, 3] in those events causing the incoming γ photon to be scattered from one detector element and then photoabsorbed in the second one. Add-back energy spectra showed Peak-To-Total approximately 50 % and 60 % in case of the first and second geometry, respectively. Compton kinematics and energy conservation law then give the scattering angle (with respect to ΔE-energy deposited in the second detector element and E_i-energy before scattering):

$$\beta = \arccos\left(1 - \frac{m_e c^2 \Delta E}{(E_i)^2 - E_i \Delta E}\right) \tag{1}$$

For our offline analysis it is essential to find the scattered direction, i.e. vector. Simulation gives the exact coordinates of the interaction points, so the 3D vector (ρ, θ, ϕ) is easily extracted. The algorithm concentrates on the reference plane (θ, ϕ), where the centre of each circle (θ, ϕ) characterizes the scattered direction. Finally, the scattering angle is seen as a radius of the corresponding circle, as illustrated in Fig 2.

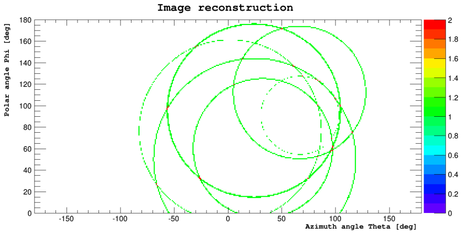

Figure 2: Representation of the reconstructing algorithm

Summary and Outlook

The simulation code has been developed providing the input data for the offline analysis and the flexibility for deploying different materials and/or geometries has been achieved. First version of the algorithm which aims to reconstruct the source position confirmed the idea of possible reconstruction of source position and is currently being tested on the larger set of data, since the preliminary results (see Fig 3.) don't yet provide an unambiguous conclusion. In addition to that, the experimental test are ongoing and the parameters from the simulations have to be normalized with respect to the response from the realistic setup [4].

---

[*] n.lalovic@gsi.de

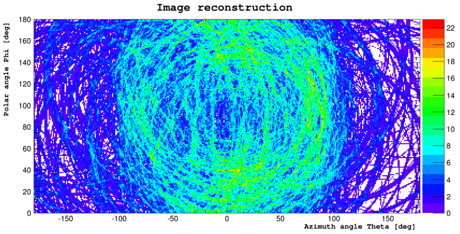

Figure 3: Reconstructing algorithm applied on a small set of data

References

[1] Geant4 - A Simulation Toolkit, Nucl. Instr. Meth. A506, 250 (2003)

[2] N. Dogan, D. K. Wehe, A. Z. Akcasu, IEEE Trans. Nucl. Sci. 39, 1427 (1992)

[3] N. Dogan, D. K. Wehe, G. F. Knoll, Nucl. Instr. Meth. A299, 501 (1990)

[4] P. Golubev, D. Rudolph, private communication

Paper II

EPJ Web of Conferences **93**, 07007 (2015)
DOI: 10.1051/epjconf/20159307007

Analysis of the Response of AGATA Detectors at GSI

N. Lalović[1,2,a], R. M. Perez-Vidal[3], C. Louchart[4], C. Michelagnoli[5], D. Ralet[4,2], T. Arici[6,2], D. Bazzacco[7], E. Clément[5], A. Gadea[3], J. Gerl[2], I. Kojouharov[2], A. Korichi[8], M. Labiche[9], J. Ljungvall[8], A. Lopez-Martens[8], J. Nyberg[10], N. Pietralla[4], S. Pietri[2], D. Rudolph[1], O. Stezowski[11], and the AGATA collaboration

[1] *Department of Physics, Lund University, S-22100 Lund, Sweden*
[2] *GSI Helmholtzzentrum für Schwerionenforschung GmbH, D-64291 Darmstadt, Germany*
[3] *Instituto de Fisica Corpuscular, CSIC-Universitat de Valencia, E-46920 Valencia, Spain*
[4] *Institut für Kernphysik, Technische Universität Darmstadt, D 64289 Darmstadt, Germany*
[5] *GANIL, CEA/DSM-CNRS/IN2P3, BP 55027, F-14076 Caen, France*
[6] *Justus-Liebig-Universität Giessen, D-35392 Giessen, Germany*
[7] *INFN Sezione di Padova and Dipartimento di Fisica, Università di Padova, IT-35131 Padova, Italy*
[8] *CSNSM, F-91405 Orsay Campus, France*
[9] *STFC Daresbury Laboratory, Daresbury, WA4 4AD Warrington, UK*
[10] *Department of Physics and Astronomy, Uppsala University, S-75121 Uppsala, Sweden*
[11] *Université de Lyon, CNRS-IN2P3, Institut de Physique Nucléaire de Lyon, F-69622 Villeurbanne, France*

Abstract. In 2012 and 2014 the γ-ray tracking spectrometer AGATA was operated at the SIS/FRS facility at GSI in Darmstadt, Germany. The performance of the array is discussed, outlining some important aspects of the offline data processing and analysis. Relying on the data obtained from measurements with standard γ-ray sources, a first estimate of the photopeak efficiency and peak-to-total (P/T) is presented.

1 Introduction

Accessing unique nuclear structure information in the field of γ-ray spectroscopy calls for an exclusive coupling of accelerator facilities for radioactive ion beams and sophisticated γ-ray spectrometers. The Advanced GAmma Tracking Array (AGATA) [1] is aiming at as exhaustive as possible spatial and energy information on γ rays. With the advance of algorithms treating the original signals of the segmented detectors, it is possible to extract the three-dimensional positions of interactions. Relying on this input, newly developed tracking algorithms can then reconstruct the path of a γ ray.

In the course of the PreSPEC-AGATA campaign at GSI [2], several source run measurements have been conducted. The setup comprised twenty-one 36-fold segmented AGATA crystals positioned at the nominal target-array distance of 23.5 cm. The calibration sources – ^{60}Co, ^{152}Eu, ^{133}Ba, ^{166}Ho and ^{56}Co – were placed at the target position. The data was acquired using an external non-segmented EUROBALL Ge detector as a reference. The output of the preamplifiers of each AGATA detector was digitized by a flash ADC. In this measurement the EUROBALL detector was connected to one of the AGATA digitizers. Therefore, it followed the same digitization procedure. The offline data treatment requires several corrections to provide reliable energy and position information for the final tracking stage. In the following, the main stages of the data processing are addressed.

2 Data Processing

The AGATA data acquisition (DAQ) system is realized via a dedicated modular framework called Narval [3], with so-called ”actors” that receive and process the data. Since the digital signal processing electronics implies parallelized treatment of the data flow, the AGATA DAQ is designed to work in a pipeline mode, such that all the detectors are handled individually. This is known as local-level processing, which is a necessary step prior to the global-level processing. At last, the previously independently handled detector events are all assembled and the actual events are built. It is also possible to perform these actions offline, replaying the raw data by means of a Narval emulator.

2.1 Overview of Data Processing Stages

At the local-level processing, the electronics is read-out and signals are saved in raw-data files. The original waveforms for all 36 segments and the central contact are decoded – at this stage, represented by the Narval actor *Producer*. The data is then formatted and passed to the actor *Preprocessing*. The amplitudes extracted previously have to be calibrated and stored. The waveform contains the time information, which is obtained using a software leading edge filter or the linear fit of the signals corresponding

---

[a] e-mail: N.Lalovic@gsi.de

to segments and central contact. Additionally, *Preprocessing* addresses the cross-talk [4] between segments.

The actor *PSA* follows and is responsible for decomposing the waveforms. It aims at deriving the interaction position. A sophisticated PSA algorithm (see Ref. [5]) performs the comparison of the recorded waveforms of observed signals with a set of reference signals. Once refined by *PSA*, the data is passed to the actor *PostPSA*. All the information, such as energy and time of the central contact and energy of the segments is accessible. This is especially important if the sum of energy deposits recorded by the segments is not equal to the energy 'seen' by the central contact. Thus, recalibration can be performed here.

Finally, the global-level processing can take place, represented by the actor *Event Builder*. To characterize the response of AGATA, only those events that fulfilled the EUROBALL-detector coincidence trigger requirement were used. Then the actor *Tracking* is applied, executing the algorithm to first group those hits that are the best candidates for a γ-ray path and then filter only those that satisfy the restrictions posed by the physics of the interaction (see, e.g., Ref. [6]).

2.2 Improvements Along the Way

To access the energy information from the sampled detector signal, the moving-window deconvolution technique is used. It relies on the digital algorithm providing trapezoidal filtering suitable for Ge detectors. Knowing the features of the detector preamplifier, such as rise-time and shaping-time, the *Preprocessing* filter can readily perform the energy calibration. In an event involving several segments, the portions of energy deposited in all of them should be equal to the initial energy, but due to the cross-talk this is not always the case. Cross-talk can compromise the energy resolution and hinder the accuracy of the segment energy information, which tracking heavily depends on. Therefore, a linear combination of amplitudes recorded by all segments has to be applied sequentially to correct for the amplitude of the actual segment. Since this analysis treats prompt $\gamma\gamma$ coincidences, time information first needs to be acquired consistently on the local-level, within each detector (segments aligned to the central contact) by *Preprocessing*, and subsequently for all the detectors (all central contacts between each other) by *PSA*. Thereby, contributions of random coincidences are well reduced. In addition, at the global-level, different time latencies of the detectors have to be fixed, and the resulting corrections passed back to the local-level *PostPSA*.

3 First Results

The analysis was initially performed on the data from the run with ^{60}Co. First estimate of efficiency and P/T at 1.173 MeV refers to AGATA as a calorimeter, summing up energies recorded by the central contacts of all crystals. The second scenario measures efficiency on the basis of energy from the central contact of only a single crystal. Preliminary γ-ray spectra of ^{60}Co in these two cases are shown in Fig. 1. Furthermore, AGATA was treated as a tracking array, utilising the energy information from reconstructed γ-ray interactions. The calorimetric approach results in an efficiency of 3.3 % and P/T of 32 %, whereas the obtained tracking efficiency yields 2.5 % and P/T of 34 %. The latter results were obtained with standard values of tracking parameters, which still require optimization in the course of the further analysis. Additionally, Geant4 simulations have been performed and they suggest somewhat higher values, namely 3.9 % efficiency and a P/T of ~50 %.

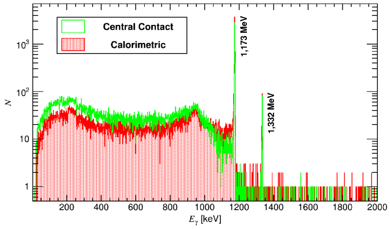

Figure 1. Pulse-height spectra measured by the AGATA array from the γ-ray spectrum issued by the ^{60}Co calibration source obtained as a sum from all central contacts (red) or scaled from a single central contact (green). The spectra were taken in prompt coincidence with the 1.332-MeV line. The weak presence of the 1.332-MeV line itself is due to random events.

4 Summary and Outlook

To optimize information from recorded signals of AGATA detectors, the complete complex framework for data processing is employed. Fine tuning is necessary to obtain a first estimate of the absolute efficiency and peak-to-total of the AGATA-at-GSI setup. The detailed analysis is still ongoing and should provide reliable performance figures of AGATA to be used for the analysis of the data taken within the PreSPEC-AGATA campaign.

Acknowledgments

This work is supported by the European Community FP7-Capacities ENSAR No. 262010 and the Helmholtz International Center for FAIR.

References

[1] S. Akkoyun *et al.*, Nucl. Instr. Meth. A **668**, 26 (2012)
[2] N. Pietralla *et al.*, Eur. Phys. J. Web of Conferences **66**, 02083 (2014)
[3] X. Grave *et al.*, Real Time Conference 14th IEEE-NPSS (2005)
[4] B. Bruyneel, Nucl. Instr. Meth. A **608**, 99 (2009)
[5] R. Venturelli and D. Bazzacco, LNL Annual Report 2004, 220 (2004)
[6] A. Lopez-Martens *et al.*, Nucl. Instr. Meth. A **533**, 454 (2004)

Paper III

Nuclear Instruments and Methods in Physics Research A 806 (2016) 258–266

Contents lists available at ScienceDirect

Nuclear Instruments and Methods in Physics Research A

journal homepage: www.elsevier.com/locate/nima

Performance of the AGATA γ-ray spectrometer in the PreSPEC set-up at GSI

N. Lalović [a,b,*], C. Louchart [c], C. Michelagnoli [d], R.M. Perez-Vidal [e], D. Ralet [b,c], J. Gerl [b], D. Rudolph [a], T. Arici [f,b], D. Bazzacco [g], E. Clément [d], A. Gadea [e], I. Kojouharov [b], A. Korichi [h], M. Labiche [i], J. Ljungvall [h], A. Lopez-Martens [h], J. Nyberg [j], N. Pietralla [c], S. Pietri [b], O. Stezowski [k]

[a] Department of Physics, Lund University, SE-22100 Lund, Sweden
[b] GSI Helmholtzzentrum für Schwerionenforschung GmbH, D-64291 Darmstadt, Germany
[c] Institut für Kernphysik, Technische Universität Darmstadt, D-64289 Darmstadt, Germany
[d] GANIL, CEA/DSM-CNRS/IN2P3, BP 55027, F-14076 Caen, France
[e] Instituto de Fisica Corpuscular, CSIC-Universitat de Valencia, E-46920 Valencia, Spain
[f] Justus-Liebig-Universität Giessen, D-35392 Giessen, Germany
[g] INFN Sezione di Padova and Dipartimento di Fisica, Universitàdi Padova, IT-35131 Padova, Italy
[h] CSNSM, F-91405 Orsay Campus, France
[i] STFC Daresbury Laboratory, Daresbury, WA4 4AD Warrington, UK
[j] Department of Physics and Astronomy, Uppsala University, SE-75120 Uppsala, Sweden
[k] Université de Lyon, CNRS-IN2P3, Institut de Physique Nuclaire de Lyon, F-69622 Villeurbanne, France

For PreSPEC and AGATA Collaborations

ARTICLE INFO

Article history:
Received 29 July 2015
Received in revised form
2 October 2015
Accepted 9 October 2015
Available online 23 October 2015

Keywords:
AGATA
Gamma-ray spectroscopy
Gamma-ray tracking
Nuclear structure
Pulse shape analysis
HPGe detectors

ABSTRACT

In contemporary nuclear physics, the European Advanced GAmma Tracking Array (AGATA) represents a crucial detection system for cutting-edge nuclear structure studies. AGATA consists of highly segmented high-purity germanium crystals and uses the pulse-shape analysis technique to determine both the position and the energy of the γ-ray interaction points in the crystals. It is the tracking algorithms that deploy this information and enable insight into the sequence of interactions, providing information on the full or partial absorption of the γ ray. A series of dedicated performance measurements for an AGATA set-up comprising 21 crystals is described. This set-up was used within the recent PreSPEC–AGATA experimental campaign at the GSI Helmholtzzentrum für Schwerionenforschung. Using the radioactive sources ^{56}Co, ^{60}Co and ^{152}Eu, absolute and normalized efficiencies and the peak-to-total of the array were measured. These quantities are discussed using different data analysis procedures. The quality of the pulse-shape analysis and the tracking algorithm are evaluated. The agreement between the experimental data and the Geant4 simulations is also investigated.

1. Introduction

Numerous exciting nuclear-structure phenomena can be probed by in-beam γ-ray spectroscopy experiments. Innovative approaches in design of dedicated detection systems during the past decades led to significant advances in position sensitivity, photopeak efficiency and peak-to-total ratio (P/T) in γ-ray spectroscopy. Moreover, the most recent γ-ray spectrometers, such as AGATA [1] and GRETA [2], brought about the new concept of high-resolution germanium tracking arrays. This paper starts out with a retrospective overview of large γ-ray arrays (Section 2) in order to introduce the developments and requirements of the new tracking arrays.

Here, the focus is the performance of AGATA in the framework of the recent PreSPEC–AGATA campaign at the GSI Helmholtzzentrum für Schwerionenforschung, Darmstadt, Germany [3,4]. Incoming particle identification is done event by event by Fragment Separator (FRS) detector systems [5]. Details of the AGATA subarray configured for the PreSPEC–AGATA campaign are presented in Section 3.

Using Monte Carlo simulations based on the Geant4 toolkit [6], extensive characterization studies of AGATA were performed [7,8].

---

[*] Corresponding author.
E-mail address: Natasa.Lalovic@nuclear.lu.se (N. Lalović).

http://dx.doi.org/10.1016/j.nima.2015.10.032
0168-9002/© 2015 Elsevier B.V. All rights reserved.

Nevertheless, it is important for the feasibility and the success of the present and future experiments to check experimentally the validity and reliability of this simulation tool, as well as the calculated performance figures. Therefore, a dedicated source measurement was performed and is described in detail in Section 4. Furthermore, the quantities such as photopeak efficiency, normalized efficiency as a function of the γ-ray energy and P/T were investigated following the procedure outlined in Section 5. The results of the analysis performed on the data alongside their interpretation and effect on other measurements are presented in Section 6. Moreover, these results were confronted to the output of the Geant4 simulation and their agreement is presented in Section 7.

Finally, the paper concludes with a short summary and an outlook for further investigations of performance of AGATA at GSI.

2. Concept of γ-ray detection with AGATA

The strength of AGATA is the ability to obtain positions and deposited energies of individual γ-ray interactions. Applying γ-ray tracking makes it possible to determine the sequence of the interactions.

The sophisticated design of AGATA came about only after a series of advancements of large γ-ray detector arrays [9,10]. At a very early stage of HPGe detectors' development, studies of nuclear structure could benefit from larger individual detectors, in comparison with Li-drifted Ge detectors. Further improvements focused on the increase of both the number of detectors and the solid angle covered by an array. This led to an enhancement of detection properties, mainly efficiency and energy resolution, and to some extent P/T. Additionally, a technique of background reduction was developed by means of Compton suppression. These efforts gave rise to the first arrays of HPGe detectors actively shielded by scintillating materials, which provided a substantial improvement of P/T.

Once a γ ray interacts with the detector medium, the energy recorded by those conventional arrays is the signal of any individual Ge-detector crystal. Typically, the absolute photopeak efficiency here depends on the intrinsic efficiency of the detector and its distance to the source. The P/T is determined by the intrinsic P/T of the individual detector elements, i.e. Ge detector plus surrounding Compton-suppression shield, and its geometry.

The next generation of Ge arrays relied on the novel idea of producing composite detectors, in particular the clover [11] and the cluster [12,13] detectors. Such detectors overcame the size limitation of the germanium crystals, while maintaining high granularity. This is important for the detection of long cascades of coincident γ rays. Arrays based on composite detectors increased efficiency over a large energy range and showed excellent P/T performance, thanks to the ‘add back’ concept [14], that uses signals from neighbouring Ge-detector crystals. Not only are the events originating in individual detectors summed to generate the total energy signal, but also the fraction of energies is recorded in cases of scattering between the crystals.

However, those detectors cover relatively large solid angles. This implies an uncertainty in γ-ray detection angle and quickly leads to Doppler-broadened peaks when studying γ-ray decays of fast-moving sources [15]. Secondly, it is difficult to distinguish two (or more) γ rays interacting at the same time in the same detector. This can lead to summing effects of coincident γ-ray transitions. The fact that those two γ rays are counted as one reduces the gain in efficiency and P/T provided by the advancement of composite detectors. Therefore, in the next generation of large γ-ray arrays the granularity was increased by means of additional contact segmentation [16,17].

The innovative concept of segmentation ensured smaller opening angles of the individual granuli, which allowed for shorter detector-to-source distance, without deteriorating energy resolution due to Doppler broadening. As a consequence, the efficiency improved significantly [8]. The first arrays had longitudinal segmentation and made the localization of the first interaction point in a two-dimensional plane possible [16,17]. In this generation of detector arrays it was not the opening angle of the crystal as a unity that affected the Doppler broadening, but that of an individual segment instead. The above mentioned summing effects are also significantly reduced. Finally, the P/T of such detector arrangements can be enhanced.

The most recent developments followed the line of segmentation introduced above, and the idea of γ-ray tracking was realized through the three-dimensional segmentation (longitudinal and azimuthal) of HPGe crystals of specific tapered shape. The prerequisite to tracking are the determined interaction points provided by the pulse-shape analysis (PSA). As a consequence, Compton-suppression shields can be excluded. This allows us to fill significantly more solid angle with Ge detectors. Currently two systems based on this principle are operational, one being in the U.S.A., GRETINA [2], and one in Europe, AGATA [1,18-20].

The present work provides the feedback on the application of PSA algorithms and helps to evaluate the reconstruction quality with respect to all three coordinates, x, y and z.

There are two types of algorithms dealing with the tracking of the subsequent interactions of a γ-ray in a Ge crystal. The first one, which is called back-tracking [21,22], is based on the reconstruction of the γ-ray path by starting the tracking procedure from the final interaction point. The second one is called forward-tracking [23–25] and starts by first recognizing clusters of interaction points. In this work, the forward-tracking algorithm is used and the results of the optimization are presented in Section 6.

3. AGATA detector configuration at GSI

In preparation for the HISPEC experiment at the FAIR-NuSTAR facility [26], the PreSPEC–AGATA campaign [3,4] was conducted at GSI in 2012 and 2014. Here, secondary radioactive beams are produced by fission or fragmentation of a primary stable beam delivered by GSI accelerator complex and selected by the FRS [5]. These beams are directed to a secondary target at relativistic energies of several hundred MeV/u. The in-flight emitted γ rays coming from the secondary reactions are therefore affected by a significant Doppler shift: the sources are moving with velocities of about 50% of the speed of light. The products of secondary nuclear reactions were discriminated using the Lund York Cologne CAlorimeter (LYCCA) [27].

The AGATA subarray composed of 21 encapsulated detectors was placed at its nominal distance of 23.5 cm to the centre of the secondary target. Such a configuration ensured optimal energy resolution of Doppler-corrected γ-ray spectra, alongside the improved efficiency of the array compared with the earlier RISING fast-beam set-up [15]. However, compared with the full AGATA array, this geometrical configuration results in only about 60% of the crystal surfaces in contact with neighbouring ones. Thus the probability of γ rays escaping the active Ge volume is rather large, which limits the tracking performance compared to a full 4π tracking array.

According to the original design [1], AGATA consists of triple clusters of Ge crystals (cf. Fig. 1). Hosting AGATA at the final focal plane of the FRS required a modified arrangement. Because of the rather large beam-spot size, the most inner ring of five triple clusters needed to be replaced. Newly developed double clusters were then put in place to guarantee angular coverage at forward angles. This is due to the Lorentz boost, which has to be considered in case of γ rays emitted from nuclei moving at relativistic energies.

The arrangement of AGATA detectors in doubles and triples is shown in Fig. 1. The triples are enclosed by blue lines and the doubles by green lines. Dashed lines refer to missing crystals in two triple clusters, as well as one crystal from an AGATA double.

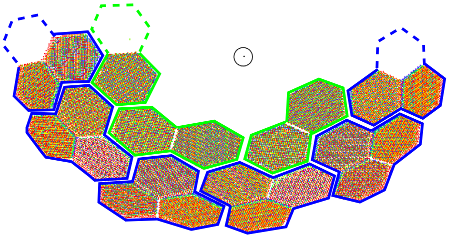

Fig. 1. Configuration of AGATA at GSI during the PreSPEC–AGATA campaign. AGATA triples are enclosed by blue lines and AGATA doubles by green lines. Dashed lines indicate missing crystals. The ⊙ symbol marks the beam direction. (For interpretation of the references to colour in this figure caption, the reader is referred to the web version of this paper.)

Its electronics was used for the EUROBALL reference capsule (see Section 4).

4. Source measurements

In order to analyse the in-beam experimental data, it is necessary to determine the response of the spectrometer by measuring efficiency and P/T. As mentioned before, simulations can be an excellent way to characterize, in a broad energy range, the performance figures for the campaigns employing AGATA. Nevertheless, simulated figures need to be checked thoroughly and, therefore, source measurements are required.

Early measurements at both LNL and GSI were severely hampered by factors such as the reduced number of encapsulated detectors present in the set-up, the uncertainties about the source position, the radiation background, the data acquisition dead time, to name but a few. Hence, a series of dedicated source measurements focusing on the determination of the absolute efficiency was performed within the scope of the PreSPEC–AGATA campaign at GSI in 2014.

The principal set-up comprised 21 36-fold segmented AGATA crystals positioned at the nominal target-array distance of 23.5 cm and one external non-segmented and electrically cooled detector [28], based on an EUROBALL capsule [12] as a reference (cf. Fig. 2). It was intended to extract the absolute quantities, such as photopeak efficiency and P/T, in the most reliable manner. This was ensured by an approach, which is based on prompt coincidences of cascading γ rays between the external reference detector, i.e. the EUROBALL capsule, and all AGATA crystals.

Each of the AGATA crystals provides 38 signals: 36 for the segments and two for the core, namely two gains corresponding to a 5-MeV and a 30-MeV full range. The output of the respective preamplifier is digitized by means of a 100-MHz 14-bit ADC. This information is then sent via optical links to pre-processing cards, which perform the task of extracting the energy and time of a particular detector element [1]. To access the energy and time information, the Moving-Window Deconvolution (MWD) technique [29] and a leading-edge algorithm have been used, respectively. The outputs of this stage are transmitted to a computer farm performing further data processing, the overview of which is given in Ref. [30]. For more details on the complete data acquisition system employed in the PreSPEC–AGATA campaign, see Ref. [31].

For the source measurements, the electrically cooled EUROBALL capsule was integrated into the system in such a way that the signal from its preamplifier was sent to one of the AGATA *digitizers*. This ensured the same treatment of all crystals used for this measurement during data-taking. However, the fact that not all AGATA-tailored processing algorithms can be applied to or are relevant for the EUROBALL capsule led to further differentiation between these two detector types in the offline analysis. Data has been taken with standard γ-ray sources: ^{56}Co, ^{60}Co and ^{152}Eu. Each source was placed at the target position in the centre of the PreSPEC–AGATA scattering chamber. During the in-beam experiments, this chamber holds the secondary target, so that the γ rays emitted from the target are to be detected by the surrounding array. For the measurements described here, the side parts of the scattering chamber were dismounted, whereas the holding ring structure was left in place. This can be seen in Fig. 2. The self-triggered data acquisition was handling the data generated by event rates up to 4–5 kHz per crystal.

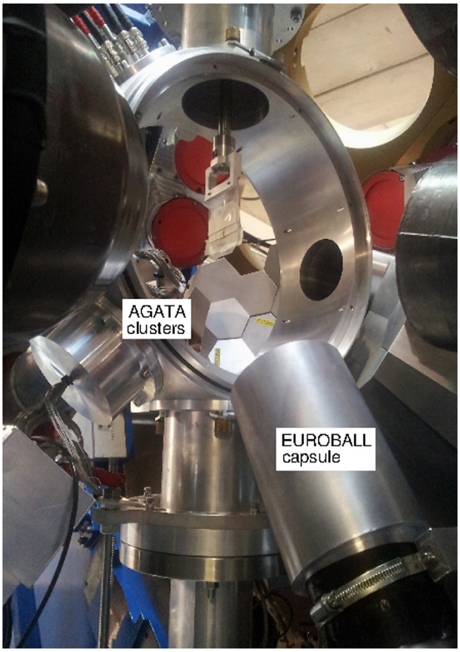

Fig. 2. Part of the experimental set-up with the EUROBALL capsule, target station, and some AGATA clusters visible in the back. The EUROBALL capsule is located in the lower right corner.

In order to make a reliable efficiency estimate of direct use for the analysis of the stopped-beam experiments, the ^{60}Co and ^{152}Eu sources were also placed in front of and behind the plastic stopper. This 1 cm thick stopper was located 15 cm downstream from the focal point of the AGATA subarray. Then, averaging measurements of these two source positions, the efficiency values are extracted for the centre of the plastic stopper. This position is denoted ‘close position’. However, since these measurements were performed in between two in-beam experiments, additional material was present around the scattering chamber, namely its side parts and a 2 mm thick lead shielding. This has to be taken into account when interpreting particularly the low energy region of the spectra recorded under these conditions.

5. Analysis

5.1. Fine tuning prior to the analysis

The processing of the signals from individual AGATA crystals and the essential calibration aspects are detailed in Ref. [30]. The processing takes place on two levels: on the *local* level all crystals are handled separately; on the *global* level the streams of processed data from individually treated crystals are assembled on the basis of time-stamp and processed further as events. The sequence of processing stages and a schematic overview are outlined in Appendix A.

In order to derive the interaction positions a number of tests with several PSA algorithms were performed. Although different, those algorithms had no apparent effect on the results and the analysis was conducted with the standard PSA algorithm, Adaptive Grid Search [33], considering single interaction in a segment.

Since the EUROBALL capsule was integrated as if it were one of the AGATA crystals, its data was processed in the same way as an AGATA crystal.

In this measurement events were constructed using all the data from the crystals within a time window of 100 ns. Thereafter, the tracking algorithm was applied on the AGATA data exclusively, which is discussed thoroughly in Section 5.2.

5.2. Absolute efficiency and peak-to-total

One of the main tasks of the data analysis was to determine the absolute efficiency of the AGATA array, depending on data treatment and parametrization. Thereby, two different approaches have been employed. The data taken with a ^{60}Co source utilizes its cascade of two coincident γ rays at 1332 and 1173 keV. In the first approach, the so-called *external trigger method*, the coincidences between AGATA crystals and the EUROBALL capsule as a reference are studied. The second approach is the *sum-peak method*, focusing on AGATA crystals only where no coincidences were used. In the external trigger method, a $\gamma\gamma$ angular correlation correction of 0.981(5) is applied for the ^{60}Co cascade, corresponding to the average angle between the AGATA crystals and the EUROBALL capsule.

5.2.1. External trigger method

Events which fulfilled the trigger requirement from the reference detector within a 100 ns time window were selected for this approach. The energy spectra representative for the whole array were created, depending on the modes in which AGATA can be operated at the data-analysis stage:

- *core common*: takes into account individual energies registered by the central contacts;
- *calorimetric*: total sum of energies recorded by all central contacts of all AGATA crystals;
- *tracked*: uses the reconstructed energy, which is subject to the tracking performance and thus choice of tracking parameters.
- *tracked, excluding single interaction*: same as the previous mode except that it discards events with only a single interaction point up to the energy of 800 keV.
- *add-back*: selectively sums single hits in an event found within a sphere of 100 mm radius. The reference point for this approach was the hit with maximum energy deposition.

The absolute efficiency at 1173 keV in all five analysis modes is extracted from the ratio of the intensity in the 1173 keV peak measured by *AGATA* crystals over the intensity of the 1332 keV peak measured by the *EUROBALL* capsule. In this case, P/T was calculated as a ratio of the yield of the peak at 1173 keV and the total number of counts in the spectrum.

Furthermore, in case of the tracking mode of analysis, the impact of the AGATA tracking algorithms on the performance was studied. This is explained in more detail in Section 6.3.

5.2.2. Sum-peak method

In this approach, the absolute efficiency was determined using the sum-peak method [34,35]. Data collected by the reference detector was not used in this case. AGATA was treated as a calorimeter, resulting in a total spectrum where the energies from all central contacts have been summed up. Thus, the absolute efficiency at 1173 keV was measured from the ratio of the intensity in the sum-peak at 2505 keV over the intensity of the 1332 keV peak. In this case, P/T was calculated as a ratio of the sum of the ^{60}Co peaks intensities and the total counts in the spectra up to 1350 keV. For a reliable efficiency estimate, a correction for random coincidences was performed, quantifying it from the activity of the source used in the measurement. Additionally, rare cases of multiple cascades have also been accounted for.

The use of the external trigger method was motivated in Section 4 as the most reliable method to extract the absolute efficiency, hence the thorough consideration of different analysis modes. In contrast, for the sum-peak method only the calorimetric mode of analysis was used to simply cross check the values obtained with the external trigger method.

5.3. Normalized efficiency

Data taken with the ^{56}Co and ^{152}Eu sources provide the energy dependence of the efficiency in the γ-ray energy range from 120 to 3300 keV. To combine the two data sets collected with the two aforementioned sources separately, the spectrum of the former was normalized with respect to the 867-keV line of the latter, since the ^{56}Co source emits a γ ray of similar energy, namely 847 keV. For this method, calorimetric, core common and the tracked mode of analysis were used.

Data taken with the ^{152}Eu source alone has also been analysed by means of the add-back routine. To normalize the yields obtained in this way, the absolute efficiency from the external trigger method was utilized (see Section 5.2.1). Furthermore, performance of the tracking has been tested on the data taken with the ^{152}Eu source only (see Section 6.3).

In order to obtain the normalized efficiency curve for the stopped-beam data from the PreSPEC–AGATA campaign, data collected with the ^{152}Eu source at the so-called ‘close position’ (see Section 4) has been analysed. Thereby, the energy information from the central contact of all crystals was employed. Finally, the yields of standard γ lines recorded at two different positions were averaged and normalized to the absolute efficiency.

6. Results

6.1. Absolute efficiency and peak-to-total

The values obtained for the absolute efficiency and P/T values at 1173 keV are shown in Table 1.

As seen in the table, the values derived for the absolute efficiency, ϵ, differ significantly for the various modes of extracting the energies from the AGATA detectors. In the conventional approach, the efficiency was determined only taking into account energy information from the central contact of each single crystal. This core-common treatment results in the lowest value of $\epsilon = 2.38(2)\%$ and the poorest $P/T = 18.3(2)\%$. Since AGATA has no Compton-suppression shields, about 60% of the Compton-scattered events escaping the crystals will increase the background of the spectra by producing counts in both neighbouring

Table 1
Efficiency and P/T at 1173 keV obtained for different modes of data treatment. The statistical uncertainties are indicated in parenthesis. Tracking refers to default parameters (cf. Section 6.3). See text for details.

Input	Efficiency (%)	P/T (%)
AGATA (*external trigger method*)		
Core common	2.38(2)	18.3(2)
Calorimetric	3.30(2)	32.2(3)
Tracked with single interactions	2.55(3)	37.5(4)
Tracked without single interactions	2.53(3)	42.3(5)
Add-back 100 mm	2.86(4)	24.6(2)
Geant4 simulations (*external trigger method*)		
Core common	2.84(9)	22.5(6)
Calorimetric	4.21(8)	42.5(10)
Tracked with single interactions	2.53(8)	58.2(19)
AGATA only		
Sum-peak calorimetric	3.25(4)	30.0(5)

crystals. Therefore, such low value of the P/T is understood. A pronounced increase in both efficiency and P/T is observed when referring to AGATA as a calorimeter, namely $\epsilon = 3.30(2)\%$ and $P/T = 32.2(3)\%$, respectively. The calorimetric mode takes into account not only full-absorption in a crystal, but also Compton-scattering into neighbouring crystals. Therefore, more events are registered in the full-energy peak, simply because energy portions, which the core-common mode predominantly interprets as background, are summed up. In general, the calorimetric mode is sensitive to summing up multiple γ rays, particularly in case of high-fold cascading γ rays.

In order to apply tracking algorithms on the present data sets, an adjustment in the data processing was implemented. The absolute efficiency measurement relies on coincidences between AGATA and the reference EUROBALL capsule, but only AGATA crystals are included in the tracking routine. Therefore, two classes of detectors have been defined in the analysis procedure: one for the EUROBALL capsule alone and the other one for all AGATA crystals, which registered a signal in a coincident event. This allowed for a separate treatment of different detectors taking part in coincident events, yet being implemented in the same DAQ system. Finally, this approach led to an efficiency of $\epsilon = 2.55(3)\%$ and $P/T = 37.5(4)\%$. The efficiency is obviously lower than the one in calorimetric mode of analysis, but P/T shows a significant improvement.

The results of the calorimetric mode suggest that summing up all energies recorded by all crystals could enhance lower-energy contributions, leading to somewhat deteriorated P/T. Additionally, this approach does not allow for rejection of partially absorbed γ rays and, as stated in Section 3, around 40% of the detector surface is not covered by other neighbouring detectors. Therefore, all partially absorbed γ rays are included in the calorimetric spectrum.

As compared to the calorimetric mode, the tracked mode results in better P/T. Tracking relies on properly extracted sequences of γ-ray energies and points and rejection of the γ rays that could not be reconstructed. Hence, it replaces the Compton suppression shields to some extent. If performed successfully, it suffers less from background contributions.

As explained in Section 5.2, the single-interaction contributions, being clusters with single hits in a detector, could be excluded from the spectrum obtained after tracking. This modification yields an efficiency of $\epsilon = 2.53(3)\%$ and $P/T = 42.3(5)\%$. The single interactions are largely responsible for the low-energy part of the spectrum, hence the better P/T values as seen in Table 1. Fig. 3 depicts this property of the spectra obtained with and without single interactions. Due to a hard-coded limit, the spectral response of single interactions extends up to 800 keV. Recent work [36] suggests that those events account for $\sim 20\%$ of the photopeak yield at 1173 keV. Therefore, the efficiency value reported here might show a corresponding increase if setting the energy acceptance limit for the single interactions as high as the γ rays of ^{60}Co.

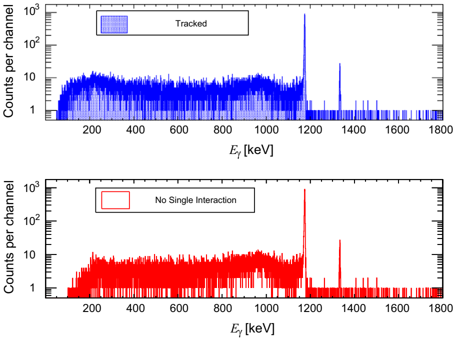

Fig. 3. Spectra obtained with the MGT tracking algorithm [24] including (upper panel) and excluding single interaction points up to 800 keV (lower panel).

The sum-peak method (see Section 5.2.2) yields results similar to the *calorimetric* mode, namely $\epsilon = 3.25(4)\%$ and $P/T = 30.0(5)\%$.

6.2. Normalized efficiency

Different in-beam experiments performed with AGATA at GSI focused on different γ-ray energy regions. Therefore, a reliable reference in terms of an energy-dependent efficiency curve is needed. In this work, the energy extends up to ~ 3.3 MeV, i.e. one of the γ-ray transitions originating from the ^{56}Co source measurement. Three modes of operating AGATA at the data-analysis stage have been considered for the combined data set of ^{56}Co and ^{152}Eu: core common, calorimetric, and tracked with default parameter values (*Figure of Merit* FOM = 10, see Section 6.3). For the analysis of the three respective cases, two spectra-analysis programs were used: tv [37] and TkT [38]. All γ-ray lines were least-squares fitted several times with a convolution of a Gaussian, a function that accounts for eventual tails on either right or left side of the centroid and another set of functions used to estimate the background. These fit results, including systematic uncertainties, were then sent to the code EFFIT, included in the Radware software package, which is using the parametrization detailed in [39] to extract the efficiency values from the measured peak intensities. The function used to fit the data points from the ^{56}Co and ^{152}Eu data sets is [39]

$$\ln \epsilon(E_\gamma) = \{(A + B{*}x + C{*}x^2)^{-G} + (D + E{*}y + F{*}y^2)^{-G}\}^{-1/G} \qquad (1)$$

with $x = \ln(E_\gamma/100)$, $y = \ln(E_\gamma/1000)$, E_γ in units of keV and A, B, C, D, E, F, G as fit parameters. Provided the absolute values of efficiency at 1173 keV (see Section 6.1 and Table 1), the aforementioned efficiencies can be readily normalized to the absolute efficiencies of the respective mode:

$$\epsilon_{\text{abs}}(E_\gamma) = N \cdot \epsilon(E_\gamma). \qquad (2)$$

The efficiency curves according to Eq. (2) for different modes of analysis, alongside the experimental values for the calibration sources, are shown in Figs. 4, 5 and 7. The values of the fit and normalization parameters for all the curves are listed in Table 2.

In case of the calorimetric spectrum, it is obvious that certain data points lie somewhat away from the least-squares fit (green stars in Fig. 4). Comparison of the γ-ray spectra has shown enhanced yields or slight modification in peak shapes. These differences in the shape of the peak in the calorimetric spectrum can arise from another

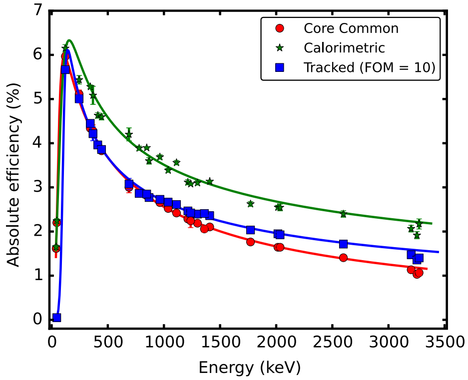

Fig. 4. Efficiency curves obtained with spectra collected with ^{56}Co and ^{152}Eu normalized to the absolute efficiency determined at 1173 keV and confirmed by an external trigger method with the ^{152}Eu source data. (For interpretation of the references to colour in this figure caption, the reader is referred to the web version of this paper.)

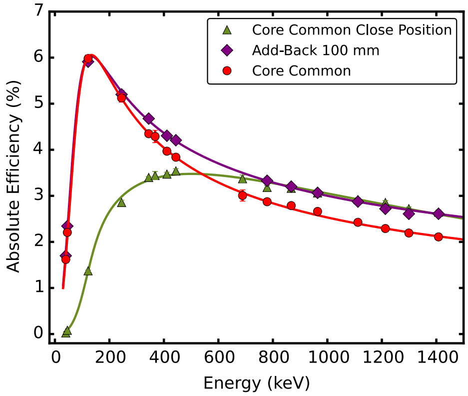

Fig. 5. Efficiency curves obtained with spectra collected with ^{152}Eu normalized to the absolute efficiency determined at 1173 keV. The green curve (triangle up) and the red curve (circle) both represent the results when utilizing core common energy information but at two different positions: the green curve being closer to the array and the red at the nominal position. The purple curve (diamond) is obtained after adding back all hits in an event, which occurred within 100 mm radius from the reference point (highest energy release). (For interpretation of the references to colour in this figure caption, the reader is referred to the web version of this paper.)

process resulting in very similar energy deposition, i.e. summing of either two coincident γ rays or a γ ray and an X ray.

The drop in tracking efficiency below 100 keV is in part related to the approximation made to compute effective distances in Ge. The approximation of a Ge sphere leads to an overestimation of the distance travelled by photons into the detector by up to a few mm. This overestimation is extremely penalizing for low-energy photons, which have very small ranges in Ge and are therefore awarded a poor figure of merit.

The results with the ^{152}Eu source at 'close position' (cf. Section 4) as well as the add-back treatment in case of the nominal position of the source are shown in Fig. 5. The two mentioned curves are compared to the core-common efficiency derived from the data collected with the same source at nominal position. In case of the core common at the close position the low-energy part of the spectrum is strongly affected by the lead shielding around the scattering chamber. Another cause of the attenuated yields is that this curve was derived by placing the ^{152}Eu source both in front and behind the plastic stopper. Consequently, in the first case the γ rays had to travel through the plastic medium, which reduced the low-energy contributions. In contrast to low energies, in the region of $E_\gamma \gtrsim 500$ keV the enhancement in the efficiency is ensured by the vicinity of the source.

6.3. *Influence of the tracking algorithms*

Two codes based on the forward-tracking algorithm mentioned in Section 2, both used by the AGATA community, have been employed to further investigate the effect of tracking on the performance. The details of the OFT performance are discussed in Ref. [36], whereas this work focuses on the MGT performance. The details of its implementation are, however, not the subject of this work. They can be found in Ref. [24].

MGT and OFT tracking algorithms start by grouping certain interaction points which may be a part of the same physical event, resulting in one *track*. These groups of candidates are called *clusters*. The interaction points in each cluster are thus accepted in a given sequence or eventually rejected based on the conditions demanded by the algorithm.

In general, for the so-called FOM only one MGT parameter is varied, which defines how restrictive the algorithm is to the data sent as an input [24]. It quantifies divergence from the accepted χ^2 value, which is calculated between the ideal angle-energy sequence and the measured one. The higher the FOM value, the more data satisfy the MGT criteria, because the clusters are evaluated with greater 'tolerance', and vice versa. Consequently, for very high values of the FOM, more data has been interpreted as 'good'. But it also happens that the algorithm considers more events as background or it simply, due to the possible surplus of lower-energy contributions, does not classify the events in clusters well enough as a part of a real Compton scattering sequence.

The behaviour of tracking efficiency and P/T with respect to the absolute tracking efficiency has been tested in MGT [24] and OFT [25,36], respectively. This was done by 'tuning' the FOM by changing the tracking parameters which are left free for the user to modify.

The effect of changing the FOM can be seen in Fig. 6. The curves show how the efficiency at 1173 keV and P/T change as the FOM varies. The efficiency is increasing with higher FOM, unlike the P/T. For higher values of the FOM, more events have fulfilled the requirement of the algorithm. Hence, one can expect enhancement in the intensity of the full-energy peak, thus in the absolute efficiency. This increase comes about at the cost of deteriorated P/T. However, after subtracting single-interaction contributions in the tracked spectra (see Section 6.1), a significant enhancement in the P/T is obtained (see Fig. 6). In the range of the tested FOM values the absolute efficiency exhibits an increasing trend for the lower values of the FOM. This behaviour is less pronounced for the rest of the range, as the absolute efficiency could not raise infinitely. Additionally, the further decrease of the P/T and the interplay of the two quantities suggest that the overall sensitivity of the system might not continue to improve significantly as the FOM increases. Therefore, the optimum value of the FOM should be decided by the user, in such a way to benefit from the changes in the values of the absolute efficiency and P/T. The MGT default value is set to $\text{FOM} = 10$ [24].

Moreover, consideration of the optimum FOM value is essential when applying tracking algorithms to different in-beam data sets. Beside Fig. 6, which shows that there is practically no increase in efficiency for FOM $\gtrsim$10, there are several criteria to be considered. Firstly, how the value of the FOM might affect the results in an energy region of interest for a certain experiment. Secondly, if

Table 2
Fit parameters using the program EFFIT [39]. In all cases the parameters $C=0$ and $G=12$ were kept fixed. See text for details.

Dataset	Mode	Parameters					
		A	*B*	*D*	*E*	*F*	*N*
^{152}Eu and ^{56}Co	Core common	8.42(19)	2.66(21)	6.410(3)	−0.573(6)	−0.071(6)	0.00454(3)
	Calorimetric	7.43(4)	1.69(5)	6.579(2)	−0.391(5)	–	0.00513(3)
	Tracked	6.80(5)	5.60(11)	6.3882(25)	−0.452(5)	–	0.00478(4)
^{152}Eu	Tracked FOM = 1.0	6.89(6)	5.73(12)	6.374(3)	−0.438(5)	–	0.00460(4)
	Tracked FOM = 0.1	7.7(3)	6.7(4)	6.274(4)	−0.421(6)	–	0.00440(5)
^{152}Eu	Add-back 100 mm	7.77(5)	1.86(6)	6.5653(24)	−0.413(5)	–	0.00423(5)
	Close position	3.11(7)	2.9(3)	4.375(5)	−0.377(20)	−0.272(20)	0.038(2)

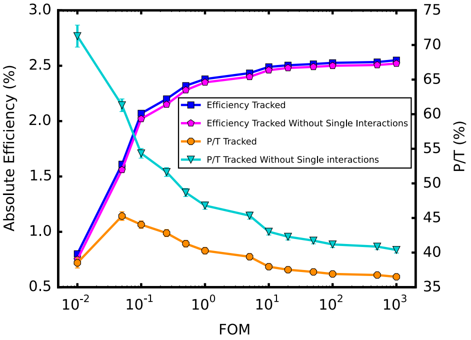

Fig. 6. Influence of the FOM on the efficiency and P/T. FOM values range from 0.01 (left) to 1000 (right). All curves are obtained after applying the MGT tracking algorithm on ^{60}Co data. The blue curve (squares) represents the tracked efficiency trend for varying FOM. The magenta curve (pentagons) is a result of the same procedure, only without single interactions being treated. The orange curve (octagon) shows how the tracked P/T is affected by different values of the FOM. Similarly, the turquoise curve (triangle down) shows the behaviour of the same quantity, only referring to the tracked data without single interactions. (For interpretation of the references to colour in this figure caption, the reader is referred to the web version of this paper.)

choosing the tracked spectrum with or without single interactions could serve as a reference alone, again depending on the energy region of interest. Finally, the selection of the best FOM might also depend on γ-ray multiplicity.

Additionally, the analysis of the ^{152}Eu data after tracking provides decisive input for treatment of the in-beam data. This implies the consideration of the ^{152}Eu dataset in the tracked mode alone, whilst varying the FOM. As in Section 6.2, the measured values of efficiency were normalized with respect to the absolute efficiency for different values of FOM and the fitting routine [39] generated the corresponding curves. Fig. 7 shows that the general trend of the efficiency curve is independent of the variation in FOM. Instead, only the absolute value of efficiency is affected by changes of the FOM. As in case of ^{60}Co data, efficiency increases as the FOM increases. Following the analysis with different values of the FOM (see Fig. 6), the three values of the FOM were selected and displayed in Fig. 7, since further increase of the FOM does not affect the values of absolute efficiency significantly. This property is, as expected, in accordance with the analysis performed on the ^{60}Co data, which strengthens the argument of choosing the appropriate FOM value.

7. Geant4 simulations

The developed Geant4 simulation comprises a realistic implementation of the set-up used during the source measurement

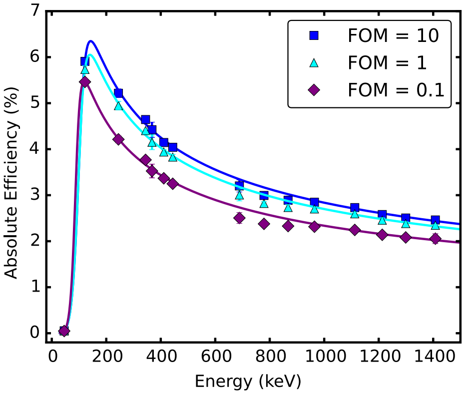

Fig. 7. Efficiency curves obtained with a ^{152}Eu source by varying the FOM in the MGT tracking algorithm.

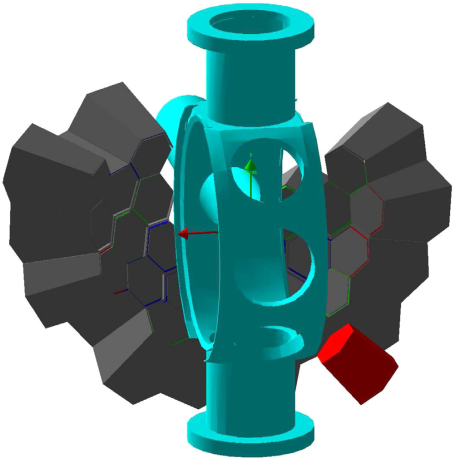

Fig. 8. Geant4 visualization of the set-up. All AGATA crystals placed around the scattering chamber and the holding structure and the EUROBALL capsule are depicted solid. When used in the full PreSPEC–AGATA set-up, the beam enters from the front side. The EUROBALL capsule, shown in red, is located in the lower right corner. (For interpretation of the references to colour in this figure caption, the reader is referred to the web version of this paper.)

including the scattering station with the holding ring structure as seen in Fig. 8. The evaluated results suggest the absolute efficiency for the core-common treatment of $\epsilon = 2.84(9)\%$ and $P/T = 22.5(6)\%$, $\epsilon = 4.21(8)\%$ and $P/T = 42.5(10)\%$ for operating AGATA in calorimetric mode and $\epsilon = 2.53(8)\%$ and $P/T = 58.2(19)\%$ for the tracking approach. The results from the simulation are somewhat higher than the experimental ones (see Table 1). They are also free from random coincidences. To first order, this can be associated to the difference between ideal detectors in the simulation and real detectors used for the experimental campaign at GSI. Despite these small discrepancies, detailed Geant4 simulations are a valuable tool in optimizing the tracking parameters for (in-beam) data analysis.

8. Summary

The performance of the AGATA subarray at GSI has been presented, with the main figures absolute efficiency and P/T being evaluated. Twenty one AGATA crystals were employed in the experimental campaign at GSI, after which the characterization measurements using calibration sources were performed. Several practical aspects of applying the tracking algorithms on the source data have been described, as well as some issues which need to be considered in case of in-beam data taken during the PreSPEC–AGATA campaign at GSI. Additionally, the same data has been analysed by exploiting only the energy recorded by the central contact of all crystals, in the so-called core-common mode, as well as summing up energies recorded by all crystals, in the calorimetric mode. The measured values of the absolute efficiency do vary, but they do so in a predictable manner, as shown by the calorimetric efficiency being larger than the core-common. This consideration affects the in-beam data in such a way that the optimal treatment should be found for each experiment individually.

Moreover, further studies should focus on high γ multiplicity effects by both adding events recorded during measurements with sources and in in-beam events. This aspect should help understand the properties of γ-ray spectra taken in in-beam conditions.

Acknowledgements

This work has been supported by the European Community FP7-Capacities, contract ENSAR no. 262010 and by the Swedish Research Council and the Knut and Alice Wallenberg Foundation. This work has also been supported by the BMBF under nos. 05P09RDFN4 and 05P12RDFN8, the LOEWE center HIC for FAIR, and the UK Science and Facilities Research Council. A.G. and R.M.P.V. were partially supported by MINECO, Spain, under the grants FPA2011-29854-C04 and FPA2014-57196-C5, Generalitat Valenciana, Spain, under the grant PROMETEOII/2014/019 and EU under the FEDER program.

Appendix A. Overview of data processing

All the operations on the data are performed with dedicated Narval [32] chains – the so-called actors on the data – implemented via C++ classes.

The data from the EUROBALL capsule was processed in the same way as from an AGATA crystal but with one exception, namely the *Tracking* actor. Furthermore, the EUROBALL capsule is a single non-segmented HPGe detector and the PSA was only formally performed on it. In practice, the algorithm applied to it differs significantly from the sophisticated AGATA-tailored algorithms. Basically, every interaction is treated as if it had happened in the centre of the crystal (Fig. A1).

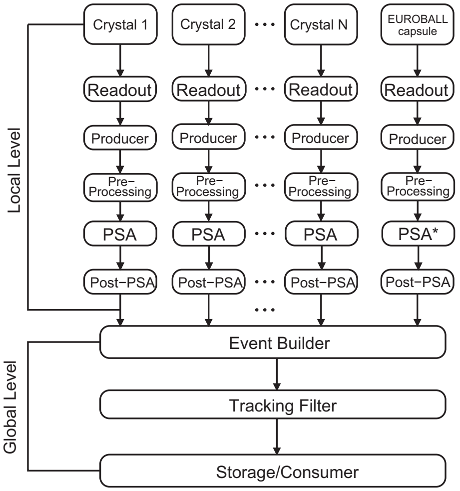

Fig. A1. Structure of AGATA data processing; here $N = 21$. Each box corresponds to a Narval actor. The EUROBALL capsule is also integrated in the system. The PSA associated to it was marked with an asterisk due to the fact that it was applied only formally. See text for details.

References

[1] S. Akkoyun, et al., Nuclear Instruments and Methods in Physics Research Section A 668 (2012).
[2] M.A. Delaplanque, et al., Nuclear Instruments and Methods in Physics Research Section A 430 (1999) 292.
[3] N. Pietralla, et al., European Physical Journal Web of Conferences 66 (2014) 02083.
[4] P. Boutachkov, et al., in preparation.
[5] H. Geissel, et al., Nuclear Instruments and Methods in Physics Research Section B 70 (1992) 286.
[6] S. Agostinelli, et al., Nuclear Instruments and Methods in Physics Research Section A 506 (2003) 250.
[7] E. Farnea, et al., Nuclear Instruments and Methods in Physics Research Section A 621 (2010) 331.
[8] C. Domingo-Pardo, et al., Nuclear Instruments and Methods in Physics Research Section A 694 (2012) 297.
[9] C.W. Beausang, J. Simpson, Journal of Physics G: Nuclear and Particle Physics 22 (1996) 527.
[10] J. Eberth, J. Simpson, Progress in Particle and Nuclear Physics 60 (2008) 283.
[11] F.A. Beck, in: Proceedings of the Conference on Physics from Large γ-ray Detector Arrays, Berkeley, LBL 35687, CONF 940888, UC 413, 1994, p. 154.
[12] J. Eberth, Progress in Particle and Nuclear Physics 28 (1992) 495.
[13] J. Eberth, et al., Nuclear Instruments and Methods in Physics Research Section A 369 (1996) 139.
[14] G. Duchêne, et al., Nuclear Instruments and Methods in Physics Research Section A 432 (1999) 90.
[15] H.J. Wollersheim, et al., Nuclear Instruments and Methods in Physics Research Section A 573 (2005) 637.
[16] J. Simpson, et al., Acta Physica Hungarica 11 (2000) 159.
[17] D. Habs, et al., Progress in Particle and Nuclear Physics 38 (1997) 1.
[18] J. Gerl, Acta Physica Polonica B 34 (2003) 2481.
[19] J. Simpson, Journal of Physics: Conference Series 41 (2006) 72.
[20] A. Gadea, et al., Nuclear Instruments and Methods in Physics Research Section A 654 (2011) 654.
[21] J. Van der Marel, B. Cederwall, Nuclear Instruments and Methods in Physics Research Section A 477 (2002) 391.
[22] L. Milechina, B. Cederwall, Nuclear Instruments and Methods in Physics Research Section A 508 (2003) 394.
[23] G.J. Schmid, et al., Nuclear Instruments and Methods in Physics Research Section A 430 (1999) 69.

[24] D. Bazzacco, Nuclear Physics A 746 (2004) 248c.
[25] A. Lopez-Martens, et al., Nuclear Instruments and Methods in Physics Research Section A 533 (2004) 454.
[26] A.M. Bruce, et al., in preparation.
[27] P. Golubev, et al., Nuclear Instruments and Methods in Physics Research Section A 723 (2013) 55.
[28] I. Kojouharov, H.-J. Wollersheim, J. Gerl, M. Wolf, T. Engert, GSI Scientific Report 2008, GSI Report 2009-1, 2009, p. 235.
[29] A. Georgiev, et al., IEEE Transactions on Nuclear Science NS-41 (1994) 1116.
[30] N. Lalović, et al., European Physical Journal Web of Conferences 93 (2015) 07007.
[31] D. Ralet, et al., Nuclear Instruments and Methods in Physics Research Section A 786 (2015) 32.
[32] X. Grave, et al., Real Time Conference on 14th IEEE-NPSS, 2005, p. 5.
[33] R. Venturelli, D. Bazzacco, LNL Annual Report 2004, 2004, p. 220.
[34] I. Kim, C. Park, H. Choi, Applied Radiation and Isotopes 58 (2005) 199.
[35] J.M.R. Hutchinson, W.B. Mann, P.A. Mullen, Nuclear Instruments and Methods 112 (1973) 187.
[36] A.Lopez-Martens, et al., Nuclear Instruments and Methods in Physics Research Section A.
[37] J. Theuerkauf, S. Esser, S. Krink, M. Luig, N. Nicolay, O. Stuch, H. Wolters, Program TV, University of Cologne, Unpublished.
[38] D. Bazzacco, The TkT Spectrum Viewer, Private Communication.
[39] D.C. Radford, Nuclear Instruments and Methods in Physics Research Section A 361 (1995) 297.

Paper IV

Role of the Δ Resonance in the Population of a Four-Nucleon State in the ^{56}Fe → ^{54}Fe Reaction at Relativistic Energies

Zs. Podolyák,[1] C. M. Shand,[1] N. Lalović,[2,3] J. Gerl,[3] D. Rudolph,[2] T. Alexander,[1] P. Boutachkov,[3] M. L. Cortés,[3,4] M. Górska,[3] I. Kojouharov,[3] N. Kurz,[3] C. Louchart,[4] E. Merchán,[4] C. Michelagnoli,[5] R. M. Pérez-Vidal,[6] S. Pietri,[3] D. Ralet,[4,3] M. Reese,[4] H. Schaffner,[3] Ch. Stahl,[4] H. Weick,[3] F. Ameil,[3] G. de Angelis,[7] T. Arici,[3,8] R. Carroll,[1] Zs. Dombrádi,[9] A. Gadea,[6] P. Golubev,[2] M. Lettmann,[4] C. Lizarazo,[4,3] D. Mahboub,[10] H. Pai,[4] Z. Patel,[1] N. Pietralla,[4] P. H. Regan,[1] L. G. Sarmiento,[2] O. Wieland,[11] E. Wilson,[1] B. Birkenbach,[12] B. Bruyneel,[13] I. Burrows,[14] L. Charles,[15] E. Clément,[5] F. C. L. Crespi,[16,11] D. M. Cullen,[17] P. Désesquelles,[18] J. Eberth,[12] V. González,[19] T. Habermann,[4,3] L. Harkness-Brennan,[20] H. Hess,[12] D. S. Judson,[20] A. Jungclaus,[21] W. Korten,[13] M. Labiche,[14] A. Maj,[22] D. Mengoni,[23,24] D. R. Napoli,[7] A. Pullia,[16,11] B. Quintana,[25] G. Rainovski,[26] P. Reiter,[12] M. D. Salsac,[13] E. Sanchis,[19] and J. J. Valiente Dóbon[7]

[1]*Department of Physics, University of Surrey, Guildford GU2 7XH, United Kingdom*
[2]*Department of Physics, Lund University, S-22100 Lund, Sweden*
[3]*GSI Helmholtzzentrum für Schwerionenforschung GmbH, D-64291 Darmstadt, Germany*
[4]*Institut für Kernphysik, TU Darmstadt, D-64289 Darmstadt, Germany*
[5]*GANIL, CEA/DRF-CNRS/IN2P3, F-14076 Caen Cedex 05, France*
[6]*Instituto de Fisica Corpuscular, Universitat de Valencia, E-46980 Valencia, Spain*
[7]*INFN, Laboratori Nazionali di Legnaro, I-35020 Legnaro, Italy*
[8]*Justus-Liebig-Universität Giessen, D-35392 Giessen, Germany*
[9]*Institute for Nuclear Research, Hungarian Academy of Sciences, P.O. Box 51, Debrecen H-4001, Hungary*
[10]*Physics Department, University of Hail, PO Box 2440 Hail, Saudi Arabia*
[11]*INFN, Sezione di Milano, I-20133 Milano, Italy*
[12]*Institut für Kernphysik, Universität zu Köln, D-50937 Köln, Germany*
[13]*Irfu, CEA, Université Paris-Saclay, F-91191 Gif-sur-Yvette, France*
[14]*STFC Daresbury Laboratory, Daresbury, Warrington WA4 4AD, United Kingdom*
[15]*Institut Pluridisciplinaire Hubert Curien, CNRS-IN2P3, Université de Strasbourg, F-67037 Strasbourg, France*
[16]*Dipartimento di Fisica dell'Università degli Studi di Milano, I-20133 Milano, Italy*
[17]*School of Physics and Astronomy, Schuster Laboratory, University of Manchester, Manchester M13 9PL, United Kingdom*
[18]*Centre de Spectrométrie Nucléaire et de Spectrométrie de Masse—CSNSM, CNRS/IN2P3 and University Paris-Sud, F-91405 Orsay Campus, France*
[19]*Department of Electronic Engineering, University of Valencia, E-46100 Burjassot (Valencia), Spain*
[20]*Oliver Lodge Laboratory, The University of Liverpool, Liverpool L69 7ZE, United Kingdom*
[21]*Instituto de Estructura de la Materia, CSIC, Madrid, E-28006 Madrid, Spain*
[22]*Institute of Nuclear Physics Polish Academy of Sciences, PL-31-342 Krakow, Poland*
[23]*Dipartimento di Fisica e Astronomia dell'Università degli Studi di Padova, I-35131 Padova, Italy*
[24]*INFN, Sezione di Padova, I-35131 Padova, Italy*
[25]*Laboratorio de Radiaciones Ionizantes, Universidad de Salamanca, E-37008 Salamanca, Spain*
[26]*Faculty of Physics, St. Kliment Ohridski University of Sofia, 1164 Sofia, Bulgaria*

(Received 2 June 2016; revised manuscript received 14 September 2016; published 23 November 2016)

The ^{54}Fe nucleus was populated from a ^{56}Fe beam impinging on a Be target with an energy of $E/A = 500$ MeV. The internal decay via γ-ray emission of the 10^+ metastable state was observed. As the structure of this isomeric state has to involve at least four unpaired nucleons, it cannot be populated in a simple two-neutron removal reaction from the ^{56}Fe ground state. The isomeric state was produced in the low-momentum (-energy) tail of the parallel momentum (energy) distribution of ^{54}Fe, suggesting that it was populated via the decay of the Δ^0 resonance into a proton. This process allows the population of four-nucleon states, such as the observed isomer. Therefore, it is concluded that the observation of this 10^+ metastable state in ^{54}Fe is a consequence of the quark structure of the nucleons.

DOI: 10.1103/PhysRevLett.117.222302

Introduction.—The structure of atomic nuclei can be understood considering the interaction between its constituents, protons and neutrons. The properties of nuclear states, being of single-particle or collective type, are always expressed in terms of proton and neutron excitations. Although nucleons are not elementary particles, their inner structure usually does not have to be considered in order to explain the low-energy nuclear properties. One exception is the magnetic moment of the nucleus, where the nonzero value in the case of the neutron [1] and the unexpectedly large value for proton [2] provided early evidence that nucleons are composite, not elementary particles.

The nucleons, protons and neutrons consist of three quarks [3,4]. The lowest energy excitation of a nucleon is the Δ resonance at an energy of 1232 MeV [5]. The Δ resonance of a proton, Δ^+, can decay into a proton ($\Delta^+ \to \pi^0 + p$), or into a neutron ($\Delta^+ \to \pi^+ + n$). Similarly, the Δ resonance of a neutron, Δ^0, can decay into a neutron ($\Delta^0 \to \pi^0 + n$), or into a proton ($\Delta^0 \to \pi^- + p$). The fact that the Δ resonance plays a role in relativistic energy charge-exchange reactions was established, by studying the final ejectile nuclei in the 1980s [6].

Here we present results of an experiment where the population of an *excited state* of a nucleus is the consequence of the inner quark structure of the nucleon. The nucleus of interest was populated in relativistic energy heavy-ion collision.

Understanding relativistic energy reactions [7] is in itself important for several reasons. It forms the basis of existing and future radioactive-beam facilities [8,9], as it is one of the main processes to produce previously unidentified nuclear species [10]. It is also the mechanism which explains the nucleosynthesis of the chemical elements beryllium, boron, and possibly lithium [11]. These elements are not produced in the stars, but from the fragmentation of carbon and oxygen in the interstellar medium.

We define relativistic energy reactions, those which occur during the collision between two nuclei at relative velocities higher than the Fermi velocity of the nucleons ($v_F \sim 10^6$ m/s). Peripheral collisions, resulting in fragments with masses close to those of the projectile and target, can be described rather successfully by the two-step abrasion-ablation model [12,13]. The macroscopic abrasion model, the most successful so far, relies on the concept of a clean cut of the projectile nucleus by the target (and vice versa). According to the model, since the relative velocity of the reaction partners is much higher than v_F, the nucleon-nucleon collisions are restricted to the overlap zone. The parts of the nuclei outside the overlap zone, called spectators or prefragments, are not supposed to be affected in the abrasion process. Considering nucleons as elementary particles, as in both abrasion and ablation phases nucleons are removed, the reaction products will always have fewer or an equal number of protons and neutrons than the initial nucleus. Therefore, the product will be a fragment of the initial nucleus. Accordingly, we adopt the term fragmentation for this process in the present Letter. We include in this term direct processes such as one or multinucleon removals (sometimes called cold fragmentation).

The existence of metastable (isomeric) states in nuclei allows for a very sensitive study of the reaction products and thus the reaction process itself. The fragments can be separated and identified, and their decays investigated in essentially background free conditions. The technique is often used to gain access to the structure of exotic nuclei [14–16], as well as for angular momentum population studies [17]. Here we will use isomeric decays in a novel way, namely, to disentangle different contributions to the mechanism of relativistic heavy-ion collisions. The influence of nucleonic excitation on the population of excited states is suggested.

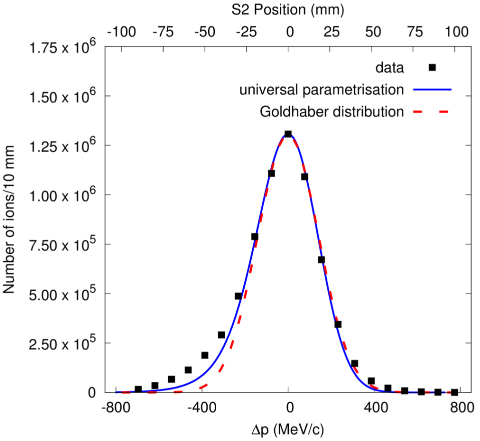

FIG. 1. Parallel momentum distribution of the ^{54}Fe ions, as deduced from the position measurement (upper X axis) at the intermediate focal plane of the fragment separator. The measured distribution is compared with the universal parametrization of [22] (continuous line) and a symmetric distribution as given by the Goldhaber formula [23] (dashed line).

Experimental details.—A primary ^{56}Fe beam at an energy of $E/A = 500$ MeV was provided by the SIS-18 accelerator at GSI, Darmstadt, Germany. The ^{56}Fe ions impinged on a 662 mg/cm^2 ^{9}Be target. The reaction products of interest were selected and identified in flight on an event-by-event basis by the fragment separator (FRS) [18]. The FRS was optimized for the transmission of bare ^{54}Fe ions. The identification of the fragments was done by magnetic rigidity and energy loss measurements [19]. The transmitted and identified ions were slowed down in a variable thickness aluminum degrader and finally implanted in a passive plastic stopper. A total of 6.8×10^6 ^{54}Fe nuclei were identified. The delayed γ rays correlated with the implanted ions were detected with the advanced gamma tracking array (AGATA) [20]. The stopper was positioned 15 cm downstream from the nominal center of AGATA in order to increase detection efficiency [21].

The use of the thin production target ensured that the energy straggling in the target is minimal and, consequently, the momentum distribution of the fragments is

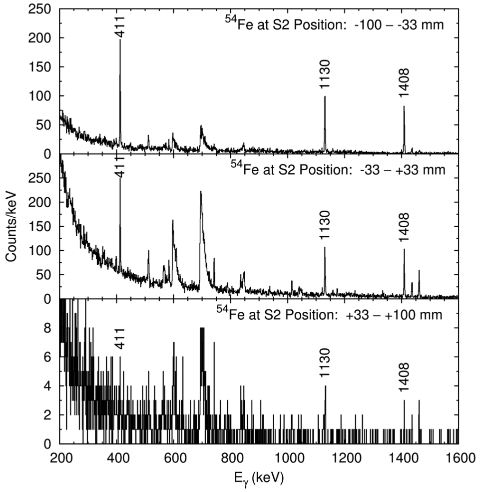

FIG. 2. Delayed ($\Delta t = 117$–1960 ns) γ-ray spectrum associated with ^{54}Fe. The three panels correspond to ^{54}Fe ions with different parallel momentum ranges. (top) $\Delta p = -750$, -247 MeV$/c$ (9.8×10^5 ^{54}Fe ions); (middle) $\Delta p = -247$, $+247$ MeV$/c$ (55.8×10^5 ions); (bottom) $\Delta p = +247$, $+750$ MeV$/c$ (1.64×10^5 ions).

determined by the reaction mechanism. The FRS was operated in achromatic mode with open slits, resulting in 100% optical transmission for the centred ^{54}Fe ions.

Results.—The parallel momentum distribution of fragments can be deduced from their magnetic rigidity, that is from their physical distribution at the dispersive focal plane at the middle of the fragment separator. The parallel momentum distribution of the ^{54}Fe fragments is shown in Fig. 1.

The delayed γ-ray spectrum associated with ^{54}Fe is shown in Fig. 2. Several γ rays are observed, which originate from the decay of the well known $T_{1/2} = 364(7)$ ns $I^\pi = 10^+$ isomeric (metastable) state [24,25].

The isomeric ratio, IR, is defined as the probability that in the reaction a nucleus is produced in an isomeric state. It can be determined experimentally as $\mathrm{IR} = Y/N_{\mathrm{imp}}FG$, where N_{imp} is the number of implanted ions, and Y is the isomeric yield. F and G are correction factors for the in-flight isomer decay losses and the finite detection time of the γ radiation, respectively. The isomeric yield is given by $Y = N_\gamma/\epsilon_{\mathrm{eff}} b_\gamma$, where N_γ is the number of counts in the γ-ray line depopulating the isomer, b_γ is the absolute γ-ray branching ratio, and ϵ_{eff} is the γ-ray detection efficiency. For more details see, e.g., Ref. [19].

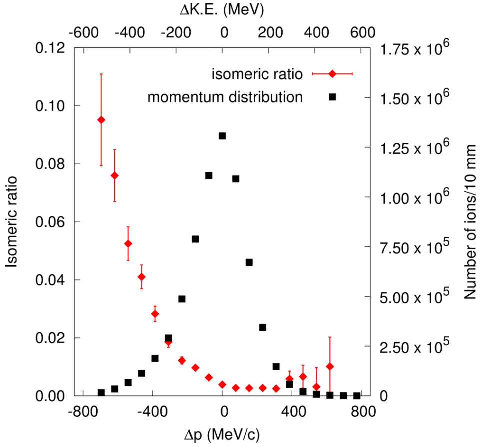

FIG. 3. Isomeric ratio of the 10^+ isomeric state in ^{54}Fe as a function of momentum transfer and corresponding kinetic energy loss (upper X axis). The measured parallel momentum distribution of the ^{54}Fe ions is also shown.

The isomeric ratio of the 10^+ isomer in ^{54}Fe was determined as a weighted average from the γ rays at 411, 1130, 1408, and 3431 keV. Its overall value is quite small at 0.77(6)%. Its dependence on the transferred momentum in the reaction is shown in Fig. 3. To investigate its momentum dependence, only the statistical errors on N_γ are shown. The systematic errors, dominated by the absolute efficiency and the loss of ^{54}Fe ions after identification due to reactions (estimated to be 20%), are around 10%, and affect all data points in the same way. The isomeric ratio is close to zero in the center of the distribution and at positive momentum transfer to the fragment. However, it is sizable, in the order of several percent, at negative momentum transfer. The isomeric ratio increases with the amount of transferred parallel momentum.

Discussion.—In relativistic energy fragmentation the parallel momentum distribution is well understood, and it is determined by the removed nucleons. In the case of two particle removal, its width is connected to the angular momentum of the removed nucleon pair [26]. At high bombarding energies, such as in the present case, it is expected to be symmetrical [27,28] around the zero momentum transfer. At lower energies there is a low momentum tail, understood as a contribution from deep-inelastic reactions. The size of the tail is dependent on the bombarding energy and it is larger at lower energies. The momentum distribution can be reproduced with the so called "universal parametrization," using parameters obtained from experiments [22].

As Fig. 1 shows, the experimental distribution measured here for ^{54}Fe is close to symmetric, but there is an additional contribution, a tail, at negative momentum transfer. The tail is rather large for $E/A = 500$ MeV bombarding energy. The aforementioned universal parametrization predicts a very small tail, and so it is not able to reproduce the measured momentum distribution (see Fig. 1).

In fragmentation reactions, by removing two neutrons from the primary ^{56}Fe beam, only two-neutron states can be populated in ^{54}Fe. This is always the case, independently of whether it is a direct two-neutron removal reaction or a neutron removal followed by the evaporation of a neutron, or even two consequent reactions in the thin target (~0.5% of the events). The ground state of ^{56}Fe has zero angular momentum (spin). However, the valence space does not contain enough angular momentum for two holes to create a state with spin $I = 10\hbar$. Modern shell-model calculations include the full pf shell, accounting for protons and neutrons up to $N = Z = 40$. Therefore, the maximum spin of two-neutron states is $I^{\pi} = 6^{+}$ from the $\nu f_{7/2}^{-2}$ two-hole configuration. $I^{\pi} = 10^{+}$ can be obtained first with two neutrons in the $\nu h_{11/2}$ orbital. This is in the upper part of the $N = 50$–82 shell, and it is expected to be essentially empty. The $h_{11/2}^{2}$ component of the isomer can be estimated from the proton decay of the analog 10^{+} state in the mirror nucleus ^{54}Ni, and it is in the order of 10^{-6} [29]. Consequently, they play no significant role in the structure of the 10^{+} isomer, and the production of this state requires at least four unpaired particles [29]. Therefore, it cannot be populated by fragmentation of ^{56}Fe. The mechanism of populating the 10^{+} isomer in ^{54}Fe from ^{56}Fe at relativistic energies has to be more complex.

The fragmentation and additional components of the relativistic energy reaction reaction can be disentangled by considering that fragmentation has essentially a symmetric momentum distribution. The momentum distribution of ^{54}Fe nuclei produced in additional reactions is shown in Fig. 4. It was obtained by subtracting the distribution of the universal parametrization (shown in Fig. 1) from the measured distribution. The large error bars are related to the uncertainty on where the middle of the measured distribution really is. An uncertainty of 1 mm was considered. As only the additional, nonfragmentation, reactions can produce the 10^{+} isomer, the isomeric ratio is recalculated, and it is given on the same figure.

The nonfragmentation events show a maximum, at around momentum transfer $\Delta p \sim -400$ MeV/c, corresponding to ~ -300 MeV kinetic energy shift. The isomeric ratio increases at high momentum transfer. At the low momentum transfer side, the accuracy is not enough to distinguish between a raising or flat behavior. Independently of whether the measured ion distribution is compared to the universal parametrization (as shown in Fig. 4), the symmetric distribution of the Goldhaber formula or the measured positive-momentum side of the distribution, the same picture is obtained.

In the simple abrasion-ablation picture of the fragmentation, no products with more neutrons or protons than the projectile can be produced. However, experiments show that this happens even at very high, $E/A = 1$ GeV, bombarding energy where the deep-inelastic reactions are negligible [6]. For example, $Z = 83$ Bi isotopes [30] and $N = 127$ isotones [31] were produced from ^{208}Pb projectiles. There are two different mechanisms at play here: (i) quasielastic collisions where a proton (neutron) takes over the total kinetic energy of a neutron (proton), and (ii) excitation of a proton (neutron) into a $\Delta(1232)$-resonance state and its subsequent decay into a neutron (proton) via pion emission. The first mechanism does not modify the momentum of the fragment, while the second one reduces it due to the escaping pion, providing a way to disentangle the two processes experimentally [30,32]. Both of these processes can result in a reaction product with higher number of protons (or neutrons) than the initial ion. Therefore, we refer to these as nonfragmentation reactions. The charge pickup cross section is in reasonable agreement with the prediction of the intranuclear cascade model [33], which accounts for Δ production and its decay via pion emission. However, the population of individual excited states cannot be predicted in that model because the nuclear structure is treated in a rather rudimentary way—no shell structure is considered.

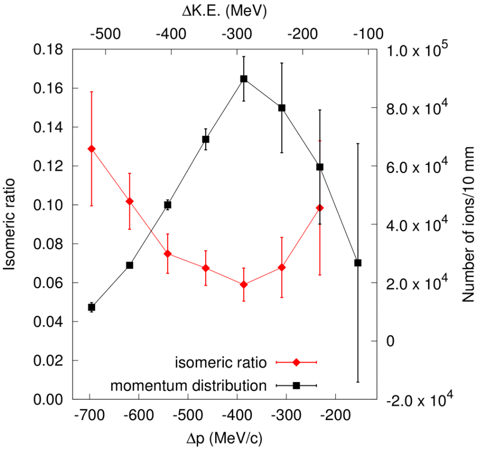

FIG. 4. Isomeric ratio of the "nonfragmentation" part of the reaction, after the pure fragmentation events are removed, as a function of momentum transfer. The momentum distribution of the nonfragmentation events is also shown. The upper scale shows the corresponding kinetic energy shift.

In addition to fragmentation, ^{54}Fe ($Z = 26$) can be produced also via the above processes, from ^{55}Co and ^{56}Co ($Z = 27$) prefragments. We note that the charge pickup reaction cross section is energy dependent [30] and it is at its highest at energies around $E/A = 500$ MeV, the energy used in the present experiment. All processes identified to populate the nucleus ^{54}Fe are illustrated in Fig. 5. The ones which involve excitation of the $\Delta(1232)$

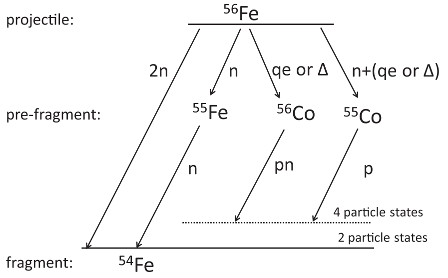

FIG. 5. Different reaction mechanisms populating ^{54}Fe from a relativistic energy collision of ^{56}Fe. Only those proceeding through the ^{55,56}Co prefragments can populate four particle states. The ones involving the Δ(1232) resonance result in a decreased momentum of the fragment. *qe* stands for quasielastic reaction.

resonance produce fragments with lower momentum, so they can readily account for the observed tail in the distribution. Also, while the main fragmentation process cannot populate four-particle states, the ones going through the ^{55,56}Co prefragments can.

The ^{55,56}Co prefragments can either decay via γ transitions to form ^{55,56}Co fragments or evaporate particles. In the latter case, proton evaporation, leading to iron isotopes, is favored as the proton separation energy is smaller by a factor of about 2 than the neutron separation energy in this neutron-deficient region of the nuclidic chart. The production cross section for both ^{55}Co and ^{56}Co is calculated within the intranuclear cascade model [13,33] to be around 3–4 mb, and we might assume a similar population probability of ^{54}Fe from both ^{55}Co and ^{56}Co. The ^{54}Fe production cross section from fragmentation is calculated to be 29.5 mb by the intranuclear cascade model [13,33], in good agreement with the 27.9 mb of the EPAX 3.1a parametrization [34]. The measured experimental ratio of momentum tail and symmetric momentum distribution of ^{54}Fe is ≈7–10%, in qualitative agreement with the above estimates. The average energy removed by the pion from the nucleus is around 300 MeV [6,30,35]. This value is in agreement with the measured energy loss of the fragment (see the secondary horizontal axis on Fig. 4).

It was previously observed that the population of high angular momentum states, $I > 15\hbar$, is higher than expected from fragmentation models [17,36,37]. However, the models do not consider nucleonic excitations. As shown in the present example, excitations of the Δ resonance (and possibly other higher-lying resonances) and its subsequent decay can produce additional angular momentum in the final fragment. This might account for the increased population of high-angular momenta states even in nuclei where there are enough valence nucleons from the start.

Conclusions.—The $I^{\pi} = 10^{+}$ isomeric state of ^{54}Fe was populated in the fragmentation of a ^{56}Fe beam at an energy of $E/A = 500$ MeV. This state has a four-nucleon configuration. Therefore, it cannot be populated by two neutron removal reactions. The isomer was populated in the low-energy tail of the ^{54}Fe distribution. The population of the isomer can be explained by considering inner excitations of a neutron, the Δ resonance. Other, higher-lying resonances might also play a role. The removed pion accounts for the lower kinetic energy, while in the process additional valence nucleons are created, contributing to the four-nucleon nature of the isomeric state.

The present result opens up the possibility to study the final nuclear states following the decay of in-medium Δ(1232) and other higher-lying resonances in relativistic energy heavy-ion collisions. The resonance production as well as the quantum state of the resulting nucleon after pion emission is expected to depend on the projectile as well as its energy. The existence of a large number of metastable states [38,39] allows the extension of the present work to other regions of the nuclidic chart. Experiments focusing on nuclei with the same atomic mass as the projectile are the most promising as these allow the direct investigation of the process, without the interference caused by additional neutron or proton emission.

We thank the GSI accelerator staff for their excellent work. Fruitful discussions with J. A. Tostevin, E. C. Simpson, and P. M. Walker are acknowledged. This work is supported by the STFC(UK), the Swedish Research Council, the German BMBF under Grants No. 05P15RD FN1, No. 05P12RDFN8, MINECO, Spain, under FPA2014-57196-C5, Generalitat Valenciana, Spain, under No. PROMETEOII/2014/019 and by the FEDER funds of the European Commission. This work has been supported by the European Community FP7–Capacities, ENSAR Contract No. 262010.

[1] L. W. Alvarez and F. Bloch, Phys. Rev. **57**, 111 (1940).
[2] R. Frisch and O. Stern, Z. Phys. **85**, 4 (1933).
[3] M. Gell-Mann, Phys. Lett. **8**, 214 (1964).
[4] G. Zweig, Developments in the Quark Theory of Hadrons **1**, 22 (1980).
[5] J. Beringer *et al.* (Particle Data Group), Phys. Rev. D **86**, 010001 (2012).
[6] D. Bachelier *et al.*, Phys. Lett. B **172**, 23 (1986).
[7] Y. Ichigawa *et al.*, Nat. Phys. **8**, 918 (2012).
[8] C. B. Hinke *et al.*, Nature (London) **486**, 341 (2012).
[9] D. Steppenbeck *et al.*, Nature (London) **502**, 207 (2013).
[10] M. Thoenessen and B. M. Sherill, Nature (London) **473**, 25 (2011).
[11] R. Bernas, E. Gradsztajn, H. Reeves, and E. Schatzman, Ann. Phys. (N.Y.) **44**, 426 (1967).
[12] J. J. Gaimard and K. H. Schmidt, Nucl. Phys. **A531**, 709 (1991).

[13] A. Boudard, J. Cugnon, J.-C. David, S. Leray, and D. Mancusi, Phys. Rev. C **87**, 014606 (2013).
[14] R. Grzywacz *et al.*, Phys. Lett. B **355**, 439 (1995).
[15] M. Pfützner *et al.*, Phys. Lett. B **444**, 32 (1998).
[16] Zs. Podolyák *et al.*, Phys. Lett. B **491**, 225 (2000).
[17] Zs. Podolyák *et al.*, Phys. Lett. B **672**, 116 (2009).
[18] H. Geissel *et al.*, Nucl. Instrum. Methods Phys. Res., Sect. B **70**, 286 (1992).
[19] M. Pfützner *et al.*, Phys. Rev. C **65**, 064604 (2002).
[20] S. Akkoyun *et al.*, Nucl. Instrum. Methods Phys. Res., Sect. A **668**, 26 (2012).
[21] N. Lalović *et al.*, Nucl. Instrum. Methods Phys. Res., Sect. A **806**, 258 (2016).
[22] O. Tarasov, Nucl. Phys. **A734**, 536 (2004).
[23] A. S. Goldhaber, Phys. Lett. B **53**, 306 (1974).
[24] D. Yan and J. Huo, Nucl. Data Sheets **121**, 1 (2014).
[25] E. Dafni, J. W. Noé, M. H. Rafailovich, and G. D. Sprouse, Phys. Lett. B **78**, 1 (1978).
[26] E. C. Simpson, J. A. Tostevin, D. Bazin, and A. Gade, Phys. Rev. C **79**, 064621 (2009).
[27] E. C. Simpson, J. A. Tostevin, Zs. Podolyák, P. H. Regan, and S. J. Steer, Phys. Rev. C **82**, 037602 (2010).
[28] E. C. Simpson, J. A. Tostevin, Zs. Podolyák, P. H. Regan, and S. J. Steer, Phys. Rev. C **80**, 064608 (2009).
[29] D. Rudolph *et al.*, Phys. Rev. C **78**, 021301(R) (2008).
[30] A. Kelić *et al.*, Phys. Rev. C **70**, 064608 (2004).
[31] A. I. Morales *et al.*, Phys. Rev. C **84**, 011601(R) (2011).
[32] C. Gaarde, Annu. Rev. Nucl. Part. Sci. **41**, 187 (1991).
[33] D. Mancusi, A. Boudard, J. Cugnon, J.-C. David, P. Kaitaniemi, and S. Leray, Phys. Rev. C **90**, 054602 (2014).
[34] K. Sümmerer, Phys. Rev. C **86**, 014601 (2012).
[35] T. Udagawa, P. Oltmanns, F. Osterfeld, and S. W. Hong, Phys. Rev. C **49**, 3162 (1994).
[36] M. Bowry *et al.*, Phys. Rev. C **88**, 024611 (2013).
[37] A. M. Denis-Bacelar *et al.*, Phys. Lett. B **723**, 302 (2013).
[38] P. M. Walker and G. D. Dracoulis, Nature (London) **399**, 35 (1999).
[39] A. K. Jain, B. Maheshwari, S. Garg, M. Patial, and B. Singh, Nucl. Data Sheets **128**, 1 (2015).

Paper V

Study of Isomeric States in ^{198,200,202,206}Pb and ^{206}Hg Populated in Fragmentation Reactions

N Lalović[1,2], D Rudolph[1], Zs Podolyák[3], L G Sarmiento[1], E C Simpson[4], T Alexander[3],M L Cortés[5,2]‡, J Gerl[2], P Golubev[1], F Ameil[2], T Arici[6,2], Ch Bauer[5], D Bazzacco[7], M A Bentley[8], P Boutachkov[5], M Bowry[3], C Fahlander[1], A Gadea[9], J Gellanki[1], A Givechev[5], N Goel[2], M Górska[2], A Gottardo[7], E Gregor[2], G Guastalla[5,2], T Habermann[2], M Hackstein[10], A Jungclaus[11], I Kojouharov[2], S Kumar[12], N Kurz[2], M Lettmann[5], C Lizarazo[2], C Louchart[13], E Merchán[5,2],C Michelagnoli[7]§, Th Moeller[5], K Moschner[10], Z Patel[3], N Pietralla[5], S Pietri[2], D Ralet[5,2]‖, M Reese[5], P H Regan[3], P Reiter[10], H Schaffner[2], P Singh[5,2], C Stahl[5], R Stegmann[5], O Stezowski[14], J Taprogge[11]¶, P Thöle[10], A Wendt[10],O Wieland[15], E Wilson[3], R Wood[3], H-J Wollersheim[2] and the AGATA Collaboration

[1]Department of Physics, Lund University, S-22100 Lund, Sweden
[2]GSI Helmholtzzentrum für Schwerionenforschung, D-64291 Darmstadt, Germany
[3]Department of Physics, University of Surrey, Guildford, GU2 XH, United Kingdom
[4]Department of Nuclear Physics, Australian National University, Canberra, 2601, Australia
[5]Institut für Kernphysik, Technische Universität Darmstadt, D-64289 Darmstadt, Germany
[6]Justus-Liebig-Universität Giessen, D-35392 Giessen, Germany
[7]INFN Sezione di Padova and Dipartimento di Fisica, Università di Padova, I-35131 Padova, Italy
[8]Department of Physics, University of York, Heslington, York YO10 5DD, United Kingdom
[9]Instituto de Fisica Corpuscular, CSIC-Universitat de Valencia, E-46920 Valencia, Spain
[10]Institut für Kernphysik, Universität zu Köln, D-50937 Köln, Germany
[11]Instituto de Estructura de la Materia, CSIC, E-28006 Madrid, Spain
[12]University of Delhi, Delhi 110007, India
[13]CEA, Centre de Saclay, IRFU/Service de Physique Nuclaire, F-91191 Gif-sur-Yvette, France
[14]Université de Lyon, CNRS-IN2P3, Institut de Physique Nuclaire de Lyon, F-69622 Villeurbanne, France
[15]INFN Sezione di Milano, I-20133 Milano, Italy

E-mail: `Natasa.Lalovic@nuclear.lu.se`

---

‡ Present address: RIKEN Nishina Center, Wako, Saitama, Japan
§ Present address: ILL Grenoble
‖ Present address: CSNSM Orsay
¶ Present address: RIKEN Nishina Center, Wako, Saitama, Japan

Abstract. Isomeric states in isotopes in the vicinity of doubly-magic ^{208}Pb were populated following reactions of a relativistic ^{208}Pb primary beam impinging on a Be fragmentation target. Secondary beams of ^{198,200,202,206}Pb and ^{206}Hg were isotopically separated and implanted in a passive stopper positioned in the focal plane of the GSI Fragment Separator. Delayed γ rays were detected with the Advanced GAmma Tracking Array (AGATA). Decay schemes were re-evaluated and interpreted with shell-model calculations. The momentum-dependent population of isomeric states in the two-nucleon hole nuclei ^{206}Pb/^{206}Hg was found to differ from the population of multi neutron-hole isomeric states in ^{198,200,202}Pb.

PACS numbers: 29.30.Kv, 25.70.Mn, 24.50.+g, 23.20.-g, 21.60.Cs, 27.80.+w

Submitted to: *J. Phys. G: Nucl. Part. Phys.*
Keywords: Gamma-ray spectroscopy, relativistic projectile fragmentation, direct reactions, isomeric decays, electromagnetic transitions, nuclear shell model.

1. Introduction

Isomeric states in nuclei continue to be valuable experimental sources for probing nuclear structure models at or beyond the line of β stability [1]. The abundance of isomeric states is usually high near the doubly-magic cornerstones of the nuclidic chart. Thus, they are of specific relevance for probing nuclear interactions within the framework of the spherical shell model, since their origin often relates to spin-aligned couplings of a limited number of unpaired particles just above, or unpaired holes just below a filled proton and/or neutron shell. The residual interactions lead to reduced phase space for electromagnetic decay, let it be in terms of decay energy or spin difference between initial and final state. The consequence are delayed electromagnetic decays, preferably observed in terms of delayed γ-ray cascades.

For the majority of cases, and in particular those far away from the line of β stability, the preparation of pure isotopic samples is highly beneficial, to say the least. Starting in the late 1990's (see, e.g., Refs. [2, 3, 4]), secondary beams from fragmentation facilities, which provide event-by-event isotopic identification, were combined with increasingly efficient γ-ray detector arrays. A prime example was the *Rare Isotope Spectroscopic INvestigations at GSI* (RISING) campaign: The combination of primary beam energies up to $E/A = 1$ GeV, the GSI Fragment Separator (FRS) [5], and the RISING germanium-detector array [6, 7] gave rise to numerous exciting discoveries of isomeric states near any heavy doubly-magic nucleus (see, for example, Refs. [8, 9, 10]), including the heaviest known one, namely ^{208}Pb (see, for instance, Refs. [11, 12]). More recently, the RISING scheme was successfully re-established with the EURICA array behind the Big-RIPS separator at RIBF, RIKEN, Japan [13].

Besides plain observation of isomeric states by means of γ-ray spectroscopy, their population via a number of possible reaction mechanisms turned into a research subject of its own right (see, e.g. [14, 15]). This includes persistence of spin alignment throughout the reaction and separation stages [16] as well as the possibility for nuclear g-factor measurements (see, e.g., Ref. [17]). The most recent highlight invokes reaction paths via the nucleonic Δ-resonance to explain the observed number of nuclei populated in a given isomeric state ('isomeric ratio') and their momentum dependence [18]. In general, few-nucleon hole states with respect to a doubly-magic core, such as ^{206}Pb or ^{206}Hg, provide the hitherto best probes to be addressed by theoretical nuclear reaction models for isomer production [19, 20].

The present study was conducted within the framework of the PreSPEC-AGATA campaign at GSI [21]. It focuses on both electromagnetic decay sequences and (different) population mechanisms of isomeric states in multi neutron-hole residues ^{198,200,202}Pb, in contrast to isomeric states produced in the two-nucleon hole pair ^{206}Pb/^{206}Hg. The experimental details are provided in Sec. 2, and the experimental results presented in Sec. 3. Section 4 sees both the shell-model interpretation of the spectroscopic results, thereby probing several shell-model parametrizations, and a theoretical assessment of the observed (fragmentation) reaction pattern. The article concludes with a brief summary.

2. Experimental approach

The method of correlating γ radiation from isomeric states with a given isotope via the production of rare isotopes by fragmentation reactions followed by separation, event-by-event identification, and implantation of the residues in the focus of a Ge-detector array has been proven to be very effective and to provide clean spectroscopic conditions even for heavy nuclei (see, for instance, Refs. [11, 12]).

The experiment builds upon a ^{208}Pb heavy-ion beam accelerated to 1 GeV/u by the UNILAC-SIS accelerator complex at the GSI Helmholtzzentrum für Schwerionenforschung at Darmstadt, Germany. The primary beam impinged on a 2.5 g/cm^2 Be target at the entrance of the FRS [5]. This initiates few-nucleon knockout and fragmentation reactions into the isotopes of interest, namely ^{198,200,202,206}Pb [22] and ^{206}Hg [23, 24]. For each isotope, primary beam intensities and spill lengths were adjusted to match the rate capabilities of the FRS detectors, ranging from $6 \cdot 10^7$ ^{208}Pb particles per 10-s spill for ^{206}Pb ions at the beginning of the experiment to $1.2 \cdot 10^9$ particles per 4-s spill for ^{206}Hg or ^{198}Pb toward the end of the experiment.

Following the established FRS calibration procedure [25] of the standard ion identification detectors of the FRS [5] with a low-intensity primary beam, FRS magnet settings for the various isotopes of interest were checked and optimized one by one. All secondary beams were set to reach the secondary target and stopper located at the FRS final focus, S4, with 160 MeV/u. Such secondary beam energies enable the efficient transport and event-by-event identification of fully stripped Pb^{82+} and Hg^{80+} ions. Since these ions are close in mass A and proton number Z to the primary beam, the beam purity of the secondary beams is predicted and measured to be rather high, ranging from about 90% for ^{198}Pb up to some 98% for ^{206}Pb. In turn, H-like and He-like primary beam particles needed to be suppressed by ±10 mm and ±20 mm slits in x direction perpendicular to the beam direction at the first, S1, and intermediate, S2, FRS focal plane, respectively. These slits are mandatory to keep the particle rate for the position, tracking, and time-of-flight start detectors at S2 manageable.

At the final focal plane, S4, the standard FRS time-of-flight stop scintillator, two time projection chambers for beam tracking, and two multi-sampling ionization chambers (MUSIC) [5] allow for event-by-event identification of each incoming ion in combination with signals from the S2 detectors. The ions then enter the PreSPEC-AGATA secondary target vacuum chamber. This chamber comprises a LYCCA [29] time-of-flight scintillator, a 32-strip by 32-strip, 0.31 mm thick LYCCA double-sided Si strip detector (target DSSSD) and secondary target ladders at the nominal 23.5 cm distance and a close position (15 cm downstream) with respect to the γ-ray spectrometer AGATA [26]. For the isomer data discussed here, a 10-mm thick piece of hard plastic was used at the close position to stop the secondary ions. For in-beam experiments following the isomer runs, the plastic stopper was removed, and a 400 mg/cm^2 gold foil placed at the nominal target position, with tertiary ions identified and stopped in the LYCCA array [29] some 3 m downstream the PreSPEC-AGATA chamber [21]. Note, however, that detailed numerical knowledge on isomeric ratios is a mandatory prerequisite for any subsequent derivation of reduced transition probabilities, $B(E2; 2+ \rightarrow 0^+)$, from Coulomb excitation.

The AGATA sub-array encompassed 17 electrically segmented HPGe crystals. Energy threshold for recording γ-ray data was restricted to ~ 50 keV. Data acquisition trigger for measurement of isomers requested a particle detected in the last plastic scintillator of the FRS [27]. The rate of validated triggers was in the range from 1.0 kHz to 1.9 kHz. Thereafter, data was recorded by means of two individual data acquisition systems for FRS (and LYCCA) as well as AGATA. Correlation between the two data streams was performed in the offline analysis, merging events within a 20 μs time window [22]. This value poses an upper limit for recording the delayed decay data, due to design of the subsequent Coulomb-excitation measurement.

3. Analysis and results

During the offline data processing, raw data from AGATA crystals in form of digitally recorded waveforms was refined by means of energy calibration, cross-talk correction, time alignment and eventual compensation for up to two absent segment signals. Details of the corresponding procedures are presented in Refs. [22, 30]. An algorithm demonstrating the underlying principle of AGATA, Pulse Shape Analysis (PSA) [31], is performed already on-line. However, various refinement in data treatment are applied at different stages of the data flow (see, e.g., Appendix A in Ref. [28]). Therefore, the PSA is performed offline once more to ensure the validity of corrections applied to the raw data.

The event-by-event ion identification follows standard FRS procedures. Here it is done by a two-dimensional selection in velocity $\beta = v/c$, which comprises mass, A, and proton number, Z. The latter is based on the energy-loss measurements in the two MUSICs, *and* affirmed by the energy-loss information from the target DSSSD. This ensures that the number of ions passing this condition equals the number of selected secondary beam particles implanted in the plastic stopper.

The isomeric ratio, R_{exp} represents a number of nuclei produced in a certain isomeric state out of all nuclei produced in a primary reaction. Deriving isomeric ratios from experimental data is summarized by:

$$R_{exp} = \frac{\frac{N_\gamma}{\epsilon_{abs} b_t}(1+\alpha_{tot})}{N_{imp}F} \cdot 100 \tag{1}$$

The numerator is a measure of the effective number of γ-ray decays following the deexcitation of the particular isomeric state. N_γ is determined by the integral of the delayed γ-ray peak, ϵ_{abs} is the absolute efficiency of the AGATA sub-array [28], and b_t is the branching ratio for the observed γ-ray transition. For internal conversion coefficients, α_{tot}, BRICC [32] was consulted. The denominator represents the number of identified ions, N_{imp}, corrected by the factor F, as a property of the experimental set-up. Several individual correction factors, f_1 - f_4, contribute to $F = f_1 \cdot f_2 \cdot f_3 \cdot f_4$.

- f_1 corrects for those time intervals when AGATA is unresponsive to the emitted γ rays due to the fast continuous radiation [33].
- f_2 corrects for the portion of ions populated in the isomeric state of interest which might decay in flight, i.e. from the production target to the final focal plane.
- f_3 takes into account the exact time limits characterizing time window for the delayed γ-ray spectra.
- f_4 accounts for the fraction of implanted ions that did not undergo tertiary nuclear reactions in the plastic stopper.

More details of an applied procedure to calculate isomeric ratios are given in Ref. [22].

In the beginning of the correlation analysis, γ-ray spectra were inspected for previously implanted ^{198,200,202,206}Pb as well as ^{206}Hg nuclei. Different generic ranges for the correlation time period after the implantation have been investigated, focusing on isomeric γ decay in the few-tenths of nanosecond to few-microsecond regimes. In the process of the analysis it was found sufficient to use AGATA in its so-called 'core common' mode [28].

The following subsections summarize the spectroscopic results and derived isomeric ratios isotope by isotope. The numerical results are summarized in Table 1, which lists the observed isomeric states, their main characteristics, and their isomeric ratios.

3.1. Isomeric States in ^{206}Hg

Isomeric decays of two previously reported states [34, 36, 35] were observed in the current experiment: an $I^\pi = 10^+$ level with $T_{1/2} = 92(8)$ ns and an $I^\pi = 5^-$ level with $T_{1/2} = 2.15(21)$ μs. Previously published values were extracted from a deep-inelastic reaction [35] and a projectile fragmentation experiment [36] similar to the one described here. The former has been experimentally exploited for population of yrast isomeric states, though not being isotopically clean to the same extent as the fragmentation reaction.

After applying software requirements to the time-energy correlation matrices, delayed γ-ray spectra for the two states of interest are singled out. They are displayed in Fig 1. Different time ranges, addressing different half-lives of the two isomeric states, were used to produce these spectra as energy projections from the time-energy matrix. The quantities relevant for the isomeric-ratio calculation regarding delayed γ data are indicated in Fig. 1: γ transition energies, exact time ranges, and deduced half-lives.

The half-life values from this measurement agree with already published information and amount to $T_{1/2} = 106(15)$ ns for $I^\pi = 10^+$ and $T_{1/2} = 2.08(4)$ μs for $I^\pi = 5^-$ state, respectively. The two relevant decay curves are shown as insets in Fig. 1. It is important to emphasize that the intention of this study was not a dedicated half-life determination. Thus the experimental conditions were not strictly adjusted for such a measurement. Despite that, the newly obtained values are not only comparable and consistent, but sometimes superior to previously published values. This leads to updated adopted weighted average values. For ^{206}Hg, they become $T_{1/2} = 108(6)$ ns for the $I^\pi = 10^+$ isomer and $T_{1/2} = 2.09(3)$ μs for the $I^\pi = 5^-$ isomer, respectively. These values are used in Fig. 2.

Due to the very different half-lives of the two states, the isomeric-ratio determination was not hampered by the fact that the lower-lying isomer depends on the feeding from the higher-lying one. As stated in Table 1, the isomeric ratio of the 10^+ state, which amounts to 3.5(2) %, is subtracted from the value for the 5^- state, yielding 29.7(13) % for the latter.

3.2. Isomeric States in ^{206}Pb

In ^{206}Pb two previously known isomeric states [34, 37, 38, 39] are observed in the present work: an $I^\pi = 12^+$ level with $T_{1/2} = 202(4)$ ns and an $I^\pi = 7^-$ level with $T_{1/2} = 125(2)$ μs. As seen in Fig. 3, in this work the half-life for the 12^+ state was the only one determined, $T_{1/2} = 203(28)$ ns. The one of the 7^- state is too long for the specifications of the current measurement. The new adopted value of the 12^+ state half-life is given in the partial level scheme of ^{206}Pb in Fig. 4. The resulting isomeric ratios are 1.3(2) % and 22.4(16) % for $I^\pi = 12^+$ and $I^\pi = 7^-$, respectively.

3.3. Isomeric States in ^{202}Pb

In the case of ^{202}Pb, three isomeric states have been studied, namely an $I^{\pi} = 19^{-}$ with $T_{1/2} = 107(3)$ ns, an $I^{\pi} = 16^{+}$ with $T_{1/2} = 110(5)$ ns, and an $I^{\pi} = 7^{-}$ with $T_{1/2} = 65.4(2)$ ns. In addition to these states, another very long-lived isomeric state has previously been published [40, 41] – an $I^{\pi} = 9^{-}$ with $T_{1/2} = 3.54(2)$ h. Given that the time of flight of the selected ions from the entrance to the FRS to the final focal plane is $\sim$ 300 ns, and considering the limited time window for delay measurements described here, γ-ray transition depopulating this 9^{-} yrast state cannot be observed.

The analysis of ^{202}Pb revealed weak presence of γ transitions originating from somewhat lighter Pb isotopes. To ensure that the identification selection only singles out ions of ^{202}Pb, those weak delayed contaminant lines were separated. They were correlated back with entries in the two-dimensional selection they stem from. However, a recognizable pattern in the corresponding β versus Z histogram was missing. Subsequently, subtracting such a histogram from the one before the contaminant removal had no effect on the final γ spectrum. The seemingly contaminating transitions were thus attributed to residues of tertiary neutron knockout in the stopper [42].

3.4. Isomeric States in ^{200}Pb

Isomeric decays of three previously reported states have been observed: an $I^{\pi} = (19^{-})$ with $T_{1/2} = 87(18)$ ns, an $I^{\pi} = (12^{+})$ with $T_{1/2} = 195(8)$ ns, and an $I^{\pi} = (9^{-})$ with $T_{1/2} = 476(12)$ ns. The (9^{-}) isomer was implicitly observed, due to the fact that it was fed from the states above.

The level scheme of ^{200}Pb in Fig. 8 suggests that the four isomeric states actually represent a 'decay chain'. Therefore, the half-life analysis of the $I^{\pi} = 9^{-}$ level accounted for the feeding from the decays of preceding isomeric states. Hence, its half-life was extracted using the Bateman equation [43] for four exponential decays of a chain [22]. The resulting value of half-life agrees very well with all individual literature values listed in [44] except for one value measured by Fant *et al* [41]. We emphasize the irreproducibility of the latter, note that Ref. [41] does not provide a decay curve, and thus this data point was excluded from the weighted average calculation to obtain the new adopted value of $T_{1/2} = 482(11)$ ns.

3.5. Isomeric States in ^{198}Pb

Much as in the case of ^{200}Pb, the level scheme of ^{198}Pb (see Fig. 10) suggests four isomeric states [45, 46] in a decay chain. We have measured half-lives of $I^{\pi} = (12)^{+}$ level with $T_{1/2} = 212(5)$ ns and $I^{\pi} = (7)^{-}$ with $T_{1/2} = 4.12(10)$ μs. The latter is a result of the fitting routine incorporating four successive exponential decays [43], similarly to Sec. 3.4. The existence of such a long-lived isomeric state with an associated $E2$ multipolarity of the $(7)^{-} \rightarrow (5)^{-}$ γ transition has not been discussed very elaborately in literature. The reader is referred to Sec. 4 for an interpretation based on the current work.

It is important to note that the 90-keV γ-ray of the $(9)^{-} \rightarrow (7)^{-}$ transition cannot be observed due to a large conversion coefficient, preventing the associated half-life to be determined. The half-life analysis regarding the $(7)^{-}$ state relied on the half-life value of the $(9)^{-}$ isomer extracted from a conversion electron measurement performed by Sun *et al* [47].

4. Discussion

To interpret the refined and new results on isomeric states and isomeric ratios described in Sec. 3, shell-model calculations have been performed. They rely on the code NuShellX [48, 49]. The calculations typically fix ^{208}Pb as the doubly-magic core, and two interactions were probed:

- Poppelier and Glaudemans derived a particle-hole interaction around ^{208}Pb stretching in principle from $Z = 58$ to $Z = 114$ and from $N = 100$ to $N = 164$ [50]. In tables and figures, this interaction has a header 'pbpop' [48]. With ^{208}Pb as closed core, the Pb isotopes of interest are subject to a model space comprising neutron holes in the $1i_{13/2}$, $3p_{3/2}$, $2f_{5/2}$, and $3p_{1/2}$ orbitals. This is the present 'default' for the 'pbpop' interaction. For the heavier Pb isotopes the computational limits allow for probing two-particle two-hole, '2p-2h', excitations across the $Z = 82$ gap by allowing up to two holes in the $1h_{11/2}$ orbital and up to two particles in either of the $1h_{9/2}$ or $2f_{7/2}$ orbitals. At variance, to approach ^{198}Pb with the calculations, it is necessary to retain at least ten neutrons in the high-j $1i_{13/2}$ orbital, 'pbpop-10'. One relevant constraint is that NuShellX is not yet optimized for large dimensions in either pure proton or pure neutron configurations, as in the case for Pb isotopes [51].
- The recommended [48] interaction for nuclei located 'South-West' from ^{208}Pb in the chart of nuclides is denoted 'khhe' [52]. It is adopted from an early Kuo-Herling interaction [53] and updated according to Ref. [54]. A more recent adjustment of several two-body matrix elements (TBME) is proposed in Ref. [55] and applied to excited states in ^{204}Tl [56] and ^{204}Hg [57], respectively. Here we start with the 'default' interaction, covering all neutron orbitals between $N = 82$ and $N = 126$, namely $1h_{9/2}$, $2f_{7/2}$, $1i_{13/2}$, $3p_{3/2}$, $2f_{5/2}$, and $3p_{1/2}$. Calculations in the unrestricted neutron space are feasible for ^{206,204}Pb and for some low-lying states in ^{202}Pb. Thereafter, various truncation schemes were systematically tested to achieve the possibility to predict excited states in ^{198,200}Pb in a controlled manner [22]. Here, we refer to the subset
  - 'tr-9', which allows for at most one neutron hole each in the $1h_{9/2}$ and $2f_{7/2}$ orbitals;
  - 'tr-f', which implies full occupation off the $1h_{9/2}$ and $2f_{7/2}$ orbitals and thus forms the same model space as 'pbpop-default';
  - 'tr-f10', which in addition requires at least ten neutrons in the high-j $1i_{13/2}$ orbital (cf. 'pbpop-10');
  - 'tr-f10M', for which the diagonal 0^+ two-body matrix-elements of the remaining $1i_{13/2}$, $3p_{3/2}$, $2f_{5/2}$, and $3p_{1/2}$ orbitals are systematically lowered according to $(N - 126) \cdot 50$ keV to handle missing contributions from pair fluctuations;
  - 'tr-f10M' ', which stretches the predicted excitation schemes by a factor 1.1, thereby accounting for some over-binding of excited states.

  The effects of these 'khhe' truncations and compensations will be detailed in the discussion of the ^{206,204}Pb predictions, displayed in Figs. 12 and 13.

Predicted $E2$ and $M1$ transition rates use standard effective charges, $e_{eff,p} = 1.5$ and $e_{eff,n} = 0.5$, and g factors of the free proton and neutron, respectively.

Finally, note that due to the quickly increasing dimensions the number of systematic large-scale shell-model surveys in the four quadrants around ^{208}Pb remains rather scarce [58, 59]. None of them tackles lighter Pb isotopes such as ^{198,200}Pb, for which particular numerical issues exist as large numbers of pure neutron configurations are concerned [51].

4.1. Decay Schemes

To establish a truncation scheme which allows shell-model calculations for ^{200}Pb and ^{198}Pb, a number of options were considered and tested on the well-known and computationally easy isotopes ^{206}Pb and ^{204}Pb. The relevant observed and predicted yrast sequences are shown in Figs. 12 and 13, respectively. Some $B(E2; 2^+ \rightarrow 0^+)$ values are presented and compared in Table 2.

As expected, both 'default' calculations reproduce the observed decay schemes very well, and in particular the (relative) position of the known isomeric states. In fact, one important message from the two figures is that the various truncations hardly affect the sequence of the yrast states. This implies that predicted spin-gap isomers persist. For instance, the 7^- in ^{206}Pb (> 90 % ${i_{13/2}}^{-1} \otimes {p_{1/2}}^{-1}$) and the 9^- in ^{204}Pb ($\approx$ 60-70 % ${i_{13/2}}^{-1} \otimes {f_{5/2}}^{-1}$), are present in any of the parametrizations. The 12^+ isomer in ^{206}Pb finds its explanation in the presence of a compressed high-spin ${i_{13/2}}^{-2}$ multiplet, which leaves the alternatives of a low-energy $E2$ or slow $E3$ decay. In ^{204}Pb there is the observed 325-keV, $12^+ \rightarrow 11^-$ $E1$ alternative, in line with the predictions.

The 'tr-9' and 'tr-f;tr-f10' truncations on the 'khhe'-side lead to a compression of low-energy states, since more and more isoscalar 0^+ pair fluctuations are suppressed. This can be reasonably well compensated for by increasing the attraction of the relevant TBME as defined above ('tr-f10M'), and subsequently stretching the whole decay scheme ('tr-f10M' '). For ^{204}Pb, the predictive power of the 'tr-f10M' ' truncation is essentially indistinguishable from its 'default'. In case of ^{206}Pb, the position of the yrast 6^+ state is a significant difference between these two parametrizations, but this is simply due to the fact that 'default' handles it as an almost pure (92 %) ${h_{9/2}}^{-1} \otimes {f_{7/2}}^{-1}$ configuration. Closing those two orbitals (cf. 'pbpop'), however, implies that this option falls outside the configuration space.

Since the truncations hardly affect the effective number of partitions in ^{206}Pb, there is hardly any effect observed on the calculated reduced transition rates. In fact, only by opening the $Z = 82$ shell (cf. 'pbpop 2p-2h') the predicted strengths approach the measured values for both ^{206}Pb and ^{204}Pb. Here one can note that the average occupation number of protons in the shells above $Z = 82$ is on the level of only 0.1. Hence, energetics are only mildly modified, and improved if anything, when comparing the 'default' and '2p-2h' predictions for the 'pbpop' interaction.

Due to the current technical limitations indicated earlier [51], for ^{202}Pb only the 0^+, 2^+, and 4^+ sequence can be diagonalized for the 'khhe default' parametrization. Similarly, trying to calculate $B(E2; 2^+ \rightarrow 0^+)$ transition strengths fails for any of the 'pbpop' parameter sets, while it is possible to diagonalize very large dimensions even for 'pbpop 2p-2h'.

The comparison between the isomer-related experimental yrast sequence and the predictions for ^{202}Pb is shown in Fig. 14. The 9^- spin-gap isomer (main configuration ${i_{13/2}}^{-1} \otimes f_{5/2}$) is reproduced by all calculations, in agreement with experiment. However, the energy gap between the yrast 7^- (${i_{13/2}}^{-1} \otimes {f_{5/2}}^{1}$) and 5^- (${i_{13/2}}^{-1} \otimes {p_{3/2}}^{-1}$) states is predicted somewhat smaller than observed, a pattern that persists toward the lighter Pb isotopes, though on the 'pbpop' side, the inclusion of 2p-2h proton excitations improves the situation for ^{202}Pb.

Due to the existence and prediction of an 11^- level ($i_{13/2}{}^{-1} \otimes (fp)^3$) below the 12^+ level ($i_{13/2}{}^{-2}$), the latter is neither found nor predicted isomeric, similar to ^{204}Pb. The predicted compressed $14^+/16^+$ and $17^-/19^-$ multiplets readily explain the observed high-spin isomers in ^{202}Pb. Finally one can note that 'tr-f10M', provides a very good description, despite its artificial compression. Similarly, hardly any effect is seen when restricting the number of neutrons to at least ten in the $i_{13/2}$ orbital for 'pbpop-10'. The sequence of states and the position of the isomers is reproduced in any case.

Figure 15 provides the comparison between experiment and theory for ^{200}Pb. Technically, a 'khhe default' treatment is no longer possible. Therefore, the 'khhe' calculations are normalized to the 9^- isomer. In terms of nuclear structure, the situation in ^{200}Pb is very much alike the one in ^{202}Pb, with two differences: there is no 11^- level (predicted) below the 12^+ state, i.e. the latter is isomeric, in line with the observations. Secondly, while the 7^- and 9^- yrast states once more form a nearly degenerate multiplet, their sequence is changed in experiment and 'khhe' predictions. In turn, the somewhat more distant 5^- state is better reproduced on the 'pbpop' side. The $14^+/16^+$ and $17^-/19^-$ multiplets are described by both interactions, though somewhat better for 'khhe' compared with 'pbpop' parametrizations. The latter are too compressed, essentially due to the more schematic origin. Of course, this may be accounted for by adjusting selected TBME, but this is beyond the scope of this work, as the focus lies in the basic understanding of the medium-spin yrast sequence and the nature of the isomeric states. In this respect, the 'khhe' 'tr-f10M' ' version is found to describe experiment very well.

Computational limits imply that calculations for ^{198}Pb are feasible only for a limited number of states for 'pbpop', and 'pbpop-10' as well as 'tr-f10M' '. They are compared to the proposed experimental decay scheme following Ref. [45]. Note that starting with the 1823-keV state, the experimental spin values are tentative. Focusing on the energetics, both predictions are in line with the observed level sequence, while the $2^+/4^+$, $5^-/7^-/9^-$, and $10^+/12^+$ multiplets are more compressed compared with experiment. At least for 'tr-f10M' ', the predicted 12^+-9^- distance is considerably smaller than observed, a feature that has not been obvious for the heavier Pb isotopes.

However, the major puzzle in this part of the ^{198}Pb decay scheme is the evaluated lifetime of the $(7)^-$ level at 2141 keV: $T_{1/2} = 4.12(10)$ μs. With $E_\gamma = 318$ keV, this yields a tiny reduced transition strength of $B(E2) \approx 0.04$ e^{2}fm^4. At variance, both rather constrained calculations, which do not account for any proton excitations across $Z = 82$ either, call for $B(E2; 7^- \rightarrow 5^-)$ values of 1.1 ('pbpop-10') and 3.4 e^{2}fm^4 ('tr-f10M' '), respectively, i.e. almost two orders of magnitude larger. This inconsistency clearly deserves further, more detailed investigations, both theoretically and experimentally. In fact, already in Refs. [46, 47] the problem was noticed, and a solution suggested based on another 7^- state, supposedly decaying by a hitherto unobserved low-energy transition. Theoretically, such an additional level is likely to be present, though not an yrast 7^-. While the latter is expected about 200 keV above the yrast 7^- state, a 6^-, 8^-, and 9^- multiplet is predicted within < 10 keV excitation energy, and just above the yrast 7^- state. Such a proximity of the even-spin negative parity 6^- and 8^- states to their odd-spin counterparts is neither observed nor predicted for any of the heavier Pb isotopes.

4.2. Isomeric Ratios

NuShellX shell-model predictions complemented with nuclear reaction theory are used to assess the isomeric ratios observed for the two-particle hole nuclei ^{206}Hg and ^{206}Pb [19, 20]. A case study of the former is found in Ref. [19], thus the focus in this article is on ^{206}Pb.

The theoretical predictions assume a direct removal of two neutrons from ^{208}Pb and result in calculated isomeric ratios of 11.2 % and 2.3 % for 7^- and 12^+ state, respectively. Yet, there is a certain probability for a one neutron removal followed by the evaporation of a second one. The calculations do not consider such a scenario. The case study of ^{206}Hg [19] concludes that the direct removal of two protons from ^{208}Pb is the dominant mechanism to produce ^{206}Hg. In case of proton emission, unlike neutron emission, there is a Coulomb barrier to be surpassed, which ensures higher probability of a direct one-step process. Hence, ^{206}Pb might be populated more also in the two step mechanism. This applies especially to the $I^\pi = 7^-$ state. For instance, if one neutron is directly removed from $i_{13/2}$ subshell and then another neutron with a smaller value of angular momentum is evaporated, negative-parity states above the 7^- might be populated as well. This explains the rather high isomeric ratio value for the 7^- isomer.

The predictions of the nucleon removal reaction theory may also benefit from another observable, i.e. the longitudinal momentum of the fragment. Experimentally deduced relationship between this observable and the isomeric ratio is displayed in Fig. 11. It is clear that the results for ^{206}Pb and ^{198}Pb are different, presumably due to the reaction mechanism involved. However, a more comprehensive comparison would require detailed calculations of the presented dependency. Up till now, the predictions of the nucleon removal reaction theory for the ^{198}Pb are missing.

5. Summary

Isomeric states have been experimentally and theoretically studied in a series of Pb isotopes. A number of experimental observables have been improved, while by and large consistent with previous isomer studies of Pb isotopes of interest. A shell-model truncation scheme applicable toward ^{198,200}Pb has been developed and successfully tested along the isomer-dominated medium-spin yrast sequences of ^{198,200,202,204,206}Pb. Isomeric ratios have been systematically derived for ^{198,200,202,206}Pb and ^{206}Hg, the latter comparable with previous values.

Acknowledgments

The authors gratefully acknowledge the outstanding work of the GSI accelerator and ion-source crews in providing the experiment with the envisaged high beam intensities. Discussions with B.A. Brown and H. Grawe are highly appreciated and gratefully acknowledged. This work is supported by the European Community FP7-Capacities, contract ENSAR No. 262010 and by the Swedish Research Council (VR 2010-147 and VR 2013-4271). This work has also been supported by the BMBF the LOEWE center HIC for FAIR, and by the UK Science and Facilities Research Council.

References

[1] Walker P and Dracoulis G 1999 *Nature* (London) **399** 35
[2] Grzywacz R *et al* 1995 *Phys. Lett.* B **355** 439
[3] M. Pfützner *et al* 1998 *Phys. Lett.* B **444** 32
[4] Podolyk Zs *et al* 2000 *Phys. Lett.* B **491** 225
[5] Geissel H *et al* 1992 *Nucl. Instrum. Methods* B **70** 286
[6] Pietri S *et al* 2007 *Nucl. Instrum. Methods* B **261** 1079
[7] Regan P H *et al* 2007 *Nucl. Phys.* A **787** 491c
[8] Rudolph D *et al* 2008 *Phys. Rev.* C **78** 021301(R)
[9] Nara Singh B S *et al* 2011 *Phys. Rev. Lett.* **107** 172502
[10] Jungclaus A *et al* 2007 *Phys. Rev. Lett.* **99** 132501
[11] Steer S J *et al* 2008 *Phys. Rev.* C **78** 061302(R)
[12] Gottardo A *et al* 2013 *Phys. Lett.* B **725** 292
[13] Watanabe H 2016 *EPJ Web of Conferences* **123** 02007
[14] Podolyk Zs *et al* 2009 *Phys. Lett.* B **672** 116
[15] Denis Bacelar *et al* 2013 *Phys. Lett.* B **723** 302
[16] Schmidt-Ott W-D *et al* 1994 *Z. Phys.* A **350**, 215
[17] Kmiecik M *et al* 2010 *Eur. Phys. J.* A **45** 153
[18] Podolyk Zs *et al* 2016 *Phys. Rev. Lett.* **117** 222302
[19] Simpson E C, Tostevin J A, Podolyk Zs, Regan P H and Steer S J 2009 *Phys. Rev.* C **80** 064608
[20] Simpson E C, Tostevin J A, Podolyk Zs, Regan P H and Steer S J 2010 *Phys. Rev.* C **82** 037602
[21] Pietralla N *et al* 2014 *EPJ Web of Conferences* **66** 02083
[22] Lalović N 2017 *PhD thesis* Lund University
[23] Alexander T *et al* 2015 *Acta Phys. Pol.* **46** 601
[24] Alexander T 2015 *PhD thesis* University of Surrey
[25] Pfützner M *et al* 2002 *Phys. Rev.* C **65** 064604
[26] Akkoyun S *et al* 2012 *Nucl. Instrum. Methods* **A668** 26
[27] Ralet D *et al* 2015 *Nucl. Instrum. Methods* **A786** 32
[28] Lalović N *et al* 2016 *Nucl. Instrum. Methods* **A806** 258
[29] Golubev P *et al* 2013 *Nucl. Instrum. Methods* **A723** 55
[30] Lalović N *et al* 2015 *EPJ Web of Conferences* **93** 07007
[31] Venturelli R and Bazzacco D 2004 *LNL Annual Report* **2004** 220
[32] Kibèdi T, Burrows T W, Trzhaskovskaya M B, Davidson P M and Nestor Jr C W, 2008 *Nucl. Instrum. Methods* **A589** 202
[33] Podolyák Zs. *et al* 2003 *Nucl. Phys. A* **722** C273
[34] Kondev F G 2008 *Nuclear Data Sheets* **109** 1527
[35] Fornal B *et al* 2001 *Phys. Rev. Lett.* **87** 212501
[36] Steer S J *et al* 2011 *Phys. Rev.* C **84** 044313
[37] Draper J E, McDonald R J and King N S P 1977 *Phys. Rev.* C **16** 1594
[38] Stenzel Ch, Grawe H, Haas H, Mahnke H-E and Maier K H 1983 *Nucl. Phys.* A **411** 248
[39] Poletti A R, Dracoulis G D, Byrne A P, Stuchberry A E, Fabricius B, Kibèdi T and Davidson P M 1994 *Nucl. Phys.* A **580** 43
[40] Zhu S and Kondev F G 2008 *Nuclear Data Sheets* **109** 699
[41] Fant B, Weckström T, Jain H C, Norlin L O, Rensfelt K-G, Carle P and Rosengård U 1987 *Nucl. Phys.* A **475** 338
[42] Rudolph D *et al* 2008 *Eur. Phys. J.* A **36** 131
[43] Bateman H 1910 *Proc Cambridge Philos Soc* **15** 423
[44] Kondev F G and Lalkovski S 2007 *Nuclear Data Sheets* **108** 1471
[45] Xiaolong H and Mengxiao K 2016 *Nuclear Data Sheets* **133** 221
[46] Stenzel C, Grawe H, Haas H, Mahnke H-E and Maier K H 1985 *Z. Phys.* A **322** 83
[47] Sun X, Rosengård U, Grawe H, Haas H, Kluge H, Kuhnert A, and Maier K H 1989 *Z. Phys.* A **333** 281
[48] Brown B A and Rae W D M 2014 *Nuclear Data Sheets* **120** 115
[49] Brown B A 2001 *Prog. Part. Nucl. Phys.* **47** 517
[50] Poppelier N A F M and Glaudemans P W M 1988 *Z. Phys.* A **329** 275
[51] Brown B A 2017 priv. comm.
[52] Warburton E K and Brown B A 1991 *Phys. Rev.* C **43** 602
[53] McGrory J B and Kuo T T S 1975 *Nucl. Phys.* A **247** 283
[54] Rydström L, Blomqvist J, Liotta R J and Pomar C 1990 *Nucl. Phys.* A **512** 217
[55] Szpak B *et al* 2011 *Phys. Rev.* C **83** 064315

[56] Broda R *et al* 2011 *Phys. Rev.* C **84** 014330
[57] Wrzesiński J *et al* 2015 *Phys. Rev.* C **92** 044327
[58] Caurier E, Rejmund M and Grawe H 2003 *Phys. Rev.* C **67** 054310
[59] Teruya E, Higashiyama K and Yoshinaga N 2016 *Phys. Rev.* C **93** 064327
[60] Chiara C J and Kondev F G 2010 *Nuclear Data Sheets* **111** 141

Figure captions

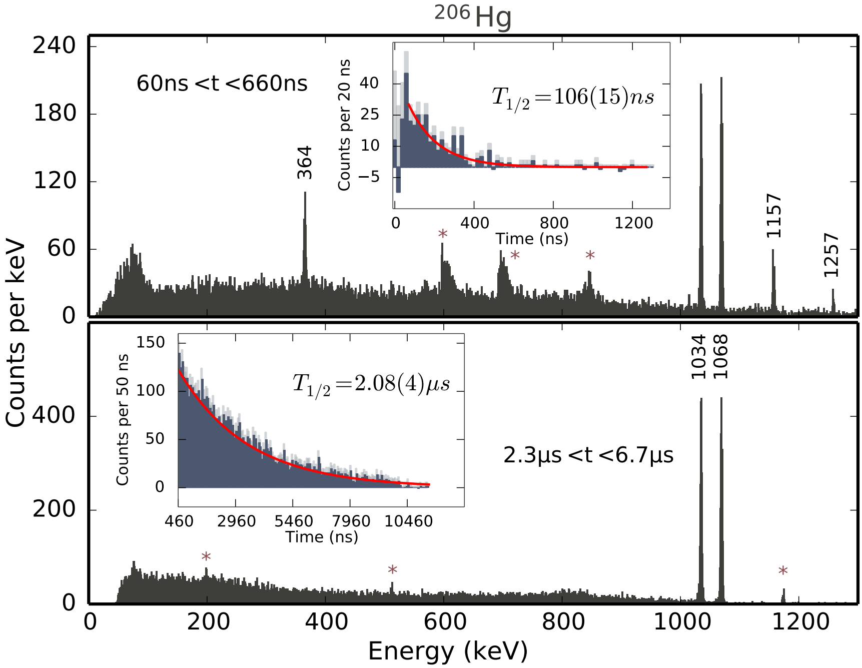

Figure 1. Delayed γ-ray spectra recorded after the implantation of ^{206}Hg ions. The peaks labelled with their energies in keV represent the transitions used to measure half-lives, whereas known background contributions are indicated by stars (*). The two panels show relevant transitions following the decay of the $I^{\pi} = 10^{+}$ isomeric state (upper panel) and those originating from the $I^{\pi} = 5^{-}$ state (lower panel). The two spectra are obtained for different time ranges: (*top*) $\Delta t = 600$ ns; (*bottom*) $\Delta t = 4.4$ μs. The insets show the decay curves of the two isomers: (*top*) as a result of the transitions at 1157 and 1257 keV; (*bottom*) as a result of the transitions at 1034 and 1068 keV. The experimental data are plotted as solid histograms and the light grey areas mark the experimental uncertainties. The solid line (red) is obtained from the least-squares fitting procedure of the exponential decay.

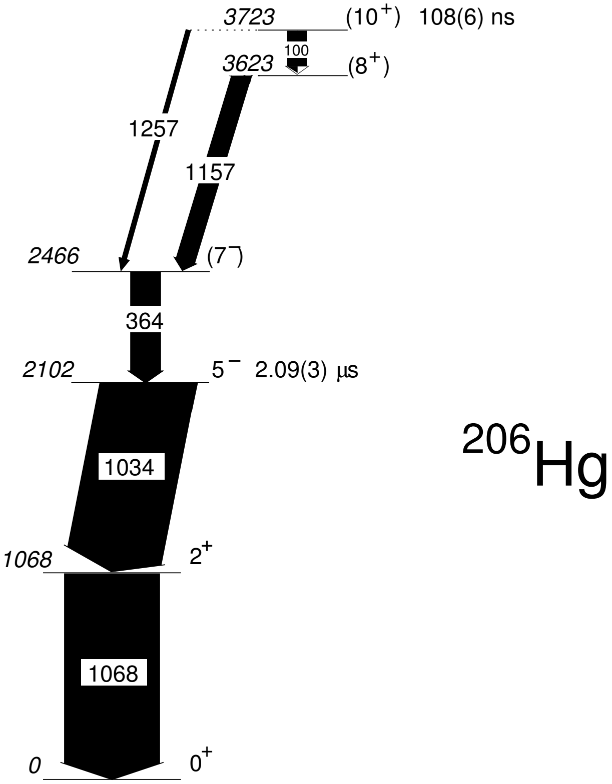

Figure 2. Partial decay scheme of two isomeric states in ^{206}Hg measured in the present work. Half-life values are the adopted values from this analysis and previous experiments. The widths of the arrows correspond to the relative yield observed in the present isomer study (cf. table 1).

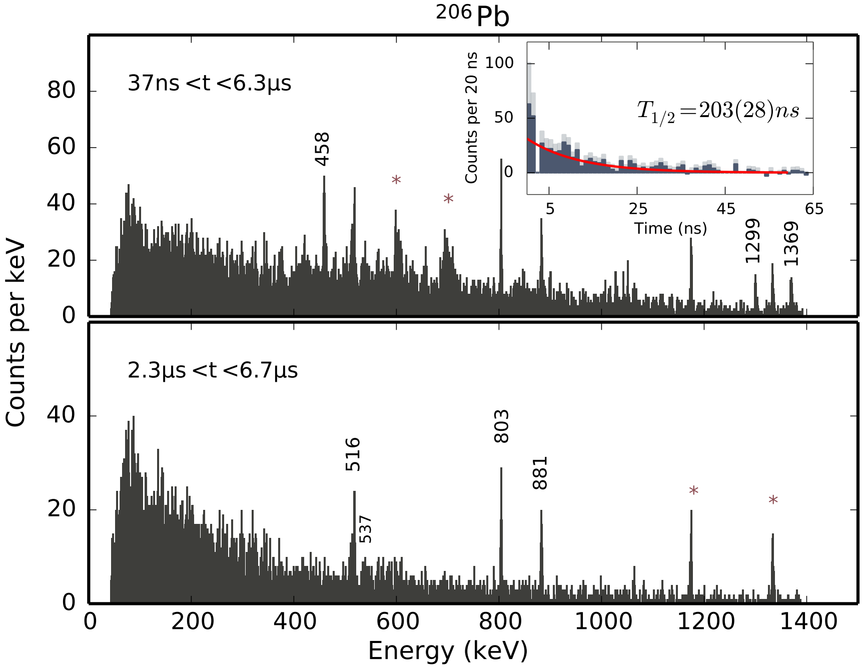

Figure 3. Delayed γ-ray spectra recorded after the implantation of ^{206}Pb ions. The two panels show relevant transitions following the decay of the $I^{\pi} = 12^{+}$ isomeric state (upper panel) and those originating from the $I^{\pi} = 7^{-}$ state (lower panel). The two spectra are obtained for different time ranges: (*top*) $\Delta t \approx 6$ μs; (*bottom*) $\Delta t = 4.4$ μs. The transitions relevant for the present analysis are labelled with energies in keV, whereas the known background contributions are indicated by stars (*). The inset shows the decay curve of the $I^{\pi} = 12^{+}$ isomer as a result of the transitions at 458, 1299, and 1369 keV; The experimental data are plotted as solid histograms and the light grey area marks the experimental uncertainties. The solid line (red) is obtained from the least-squares fitting procedure of the exponential decay.

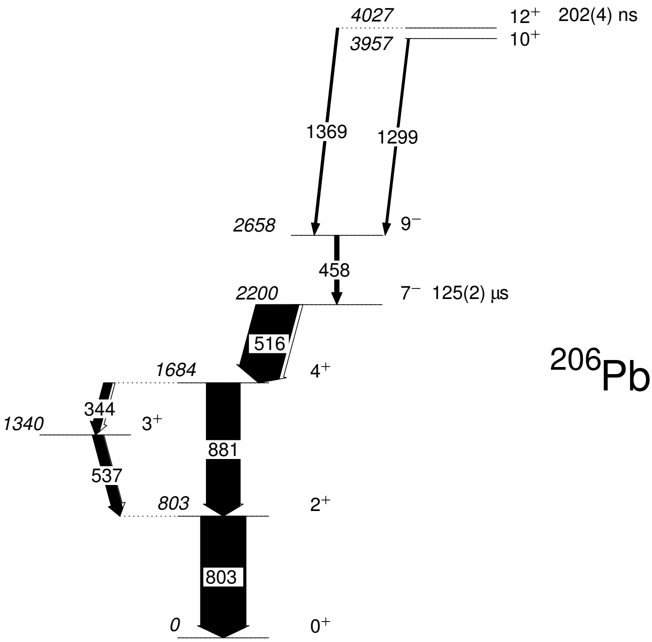

Figure 4. Partial decay scheme of two isomeric states in ^{206}Pb measured in the present work. Half-life values are the adopted values from this analysis and previous experiments. The widths of the arrows correspond to the relative yield observed in the present isomer study (cf. table 1).

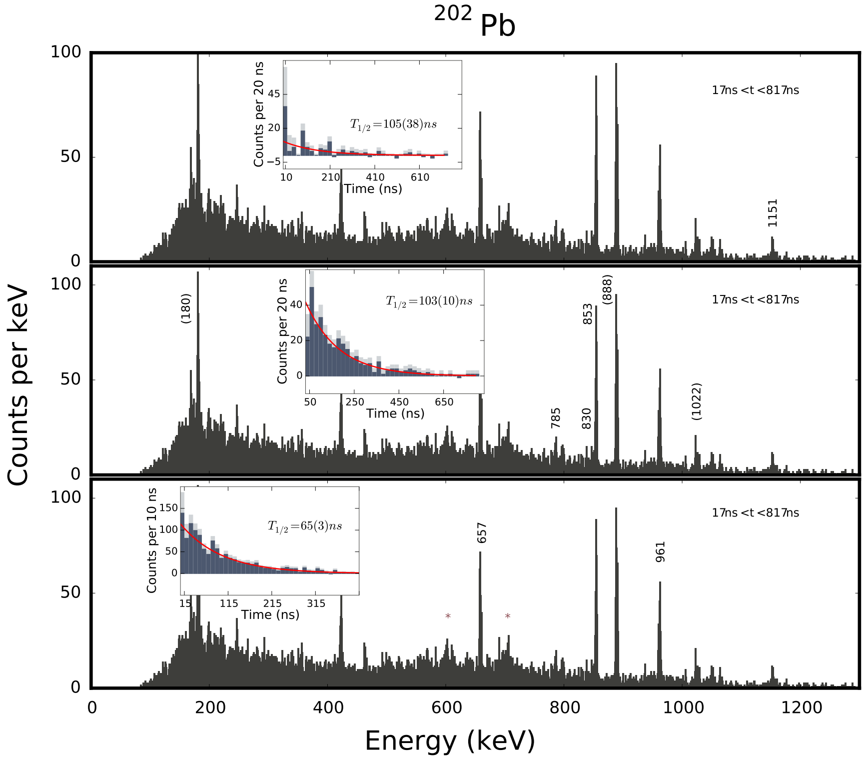

Figure 5. Delayed γ-ray spectra recorded after the implantation of ^{202}Pb ions. The three panels show relevant transitions following the decays of the $I^{\pi} = 19^{-}$ isomeric state (upper panel), $I^{\pi} = 16^{+}$ (middle panel) and those originating from the $I^{\pi} = 7^{-}$ state (lower panel). All three spectra are obtained for the same time range, $\Delta t = 800$ ns. The transitions relevant for the present analysis are labelled with energies in keV, whereas the known background contributions are indicated by stars (*). The insets show the decay curves of the isomers: (*top*) $I^{\pi} = 19^{-}$ as a result of the transitions at 1151 and 797 keV; (*middle*) $I^{\pi} = 16^{+}$ as a result of the transition at 853 keV; (*bottom*) $I^{\pi} = 7^{-}$ as a result of the transitions at 657, 422 and 961 keV. The experimental data are plotted as solid histograms and the light grey areas mark the experimental uncertainties. The solid lines (red) are obtained from the least-squares fitting procedure of the exponential decay.

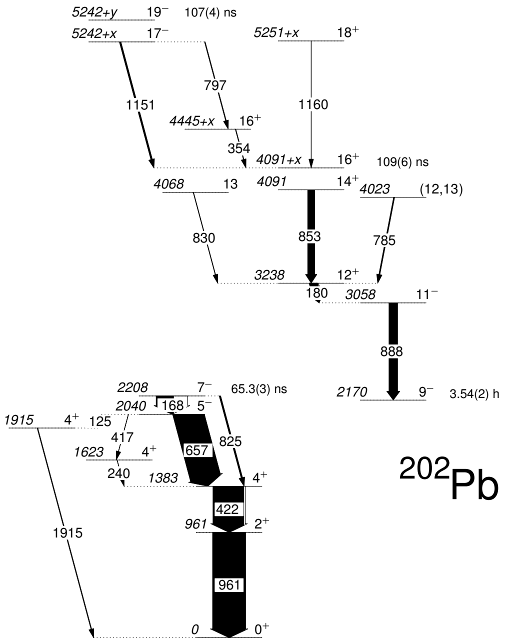

Figure 6. Partial decay scheme of three isomeric states in ^{202}Pb measured in the present work. Half-life values are the adopted values from this analysis and previous experiments. The widths of the arrows correspond to the relative yield obsered in the present isomer study (cf. table 1).

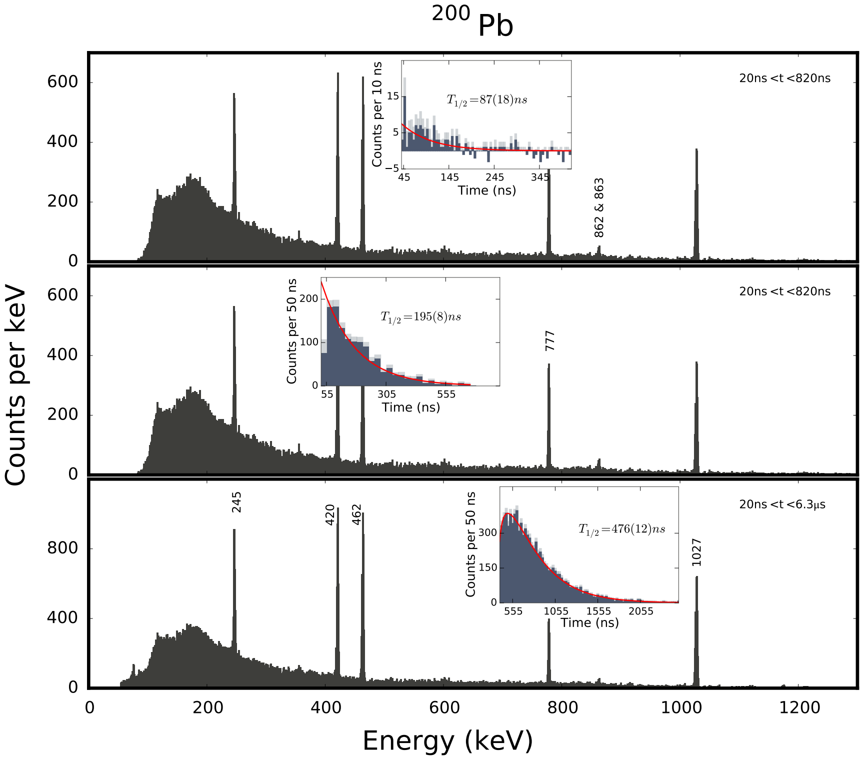

Figure 7. Delayed γ-ray spectra recorded after the implantation of ^{200}Pb ions. The three panels show relevant transitions following the decays of the $I^{\pi} = 19^{-}$ isomeric state (upper panel), $I^{\pi} = 12^{+}$ (middle panel) and those originating from the $I^{\pi} = 9^{-}$ state (lower panel). The first two spectra are obtained for the same time range, $\Delta t = 800$ ns, whereas the time range for the third one (*bottom*) is $\Delta t = 6.3$ μs. The transitions relevant for the present analysis are labelled with energies in keV, The insets show the decay curves of the isomers: (*top*) $I^{\pi} = 19^{-}$ as a result of the 862/863-keV doublet; (*middle*) $I^{\pi} = 12^{+}$ as a result of the transition at 777 keV; (*bottom*) $I^{\pi} = 9^{-}$ as a result of the transitions at 420, 462, and 1027 keV. The experimental data are plotted as solid histograms and the light grey areas mark the experimental uncertainties. The solid lines (red) are obtained from the least-squares fitting procedure of the exponential decay.

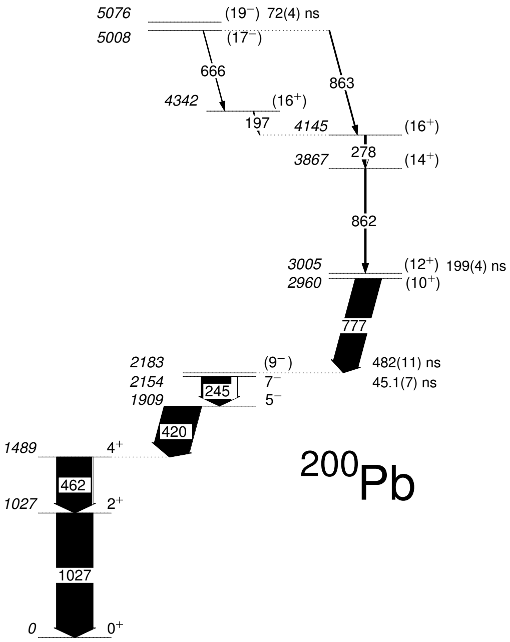

Figure 8. Partial decay scheme of isomeric states in ^{200}Pb measured in the present work. Half-life values are the adopted values from this analysis and previous experiments. The widths of the arrows correspond to the relative yield observed in the present isomer study (cf. table 1).

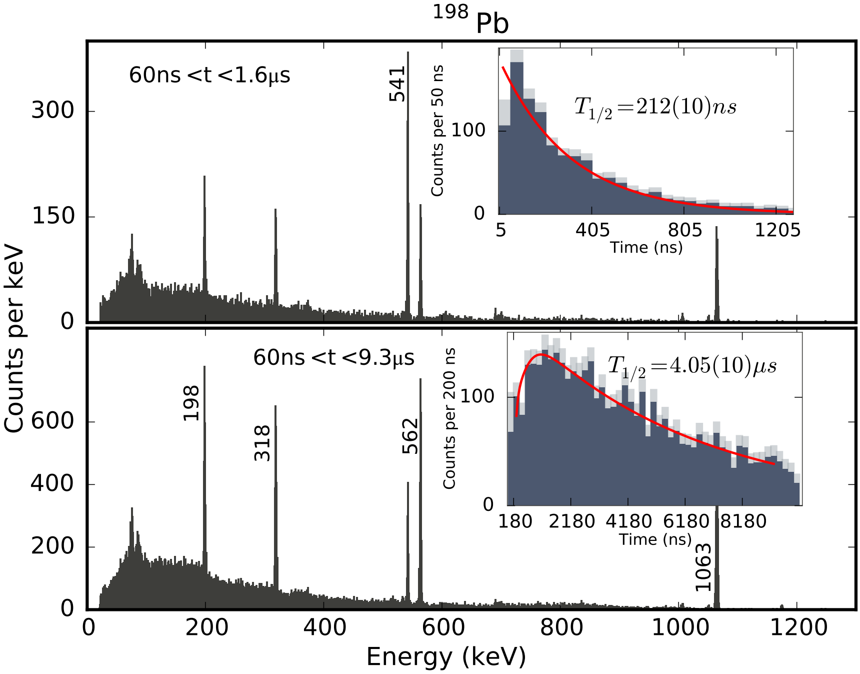

Figure 9. Delayed γ-ray spectra recorded after the implantation of ^{198}Pb ions. The two panels show relevant transitions following the decay of the $I^{\pi} = 12^{+}$ isomeric state (upper panel) and those originating in the $I^{\pi} = 7^{-}$ state (lower panel). The two spectra are obtained for different time ranges: (*top*) $\Delta t = 1.54$ μs; (*bottom*) $\Delta t = 9.24$ μs. The transitions relevant for the present analysis are labelled with energies in keV. The inset shows the decay curves of the two isomers: (*top*) as a result of the transition at 541 keV; (*bottom*) as a result of the transitions at 562 and 1063 keV. The experimental data are plotted as solid histograms and the light grey area marks the experimental uncertainties. The solid line (red) is obtained from the least-squares fitting procedure of the exponential decay.

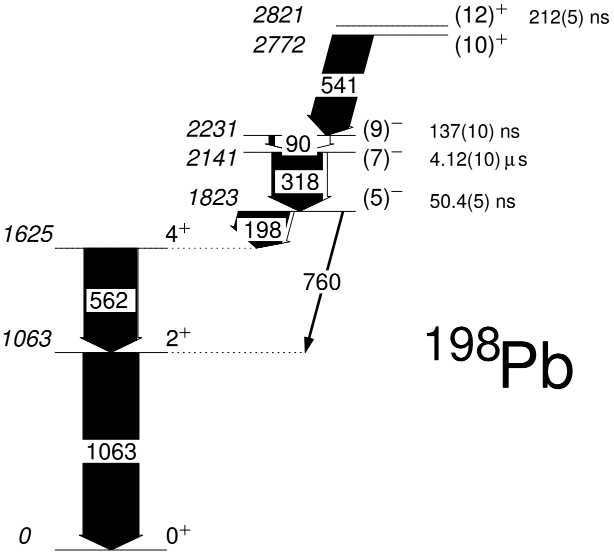

Figure 10. Partial decay scheme of isomeric states in ^{198}Pb measured in the present work. Half-life values are the adopted values from this analysis and previous experiments. The widths of the arrows correspond to the relative yield observed in the present isomer study (cf. table 1).

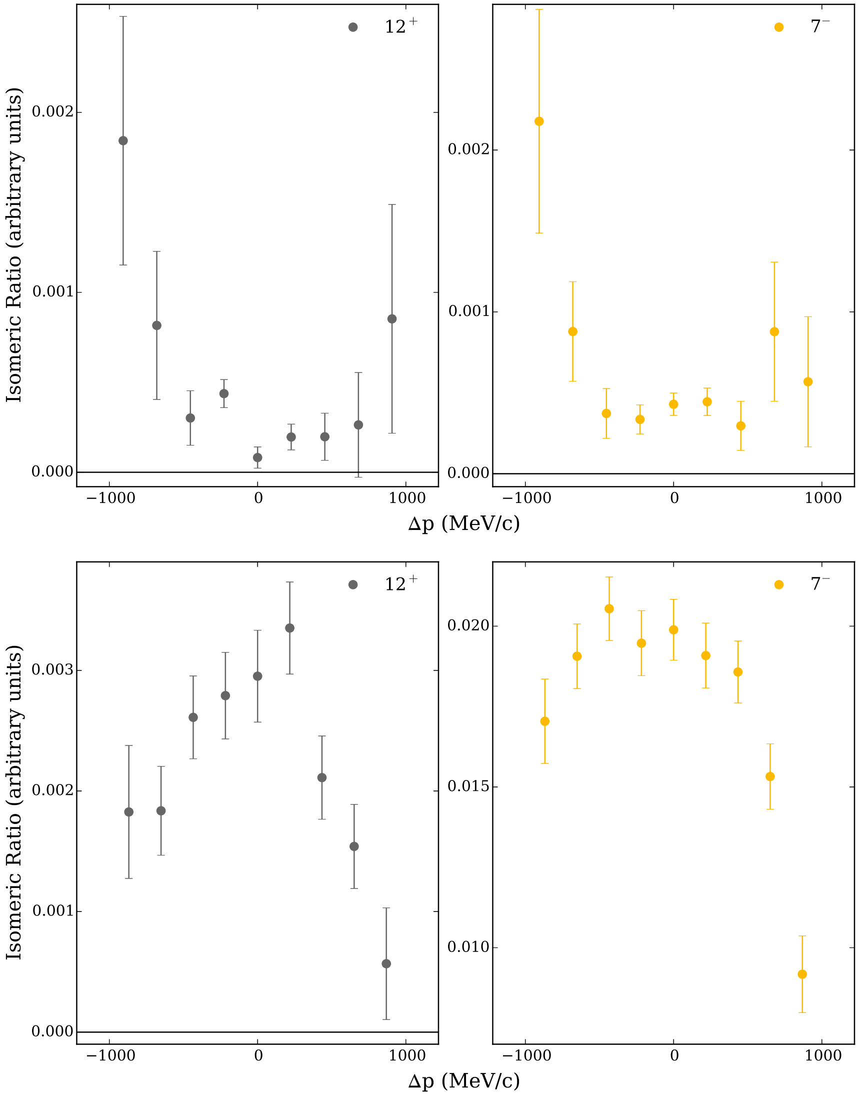

Figure 11. Isomeric ratios of the 12^+ (left column) and 7^- (right column) isomeric states in ^{206}Pb (top row) and ^{198}Pb (bottom row) as function of the position measurement of the ions at the intermediate focal plane of the fragment separator. Horizontal lines denote the value of zero isomeric ratio.

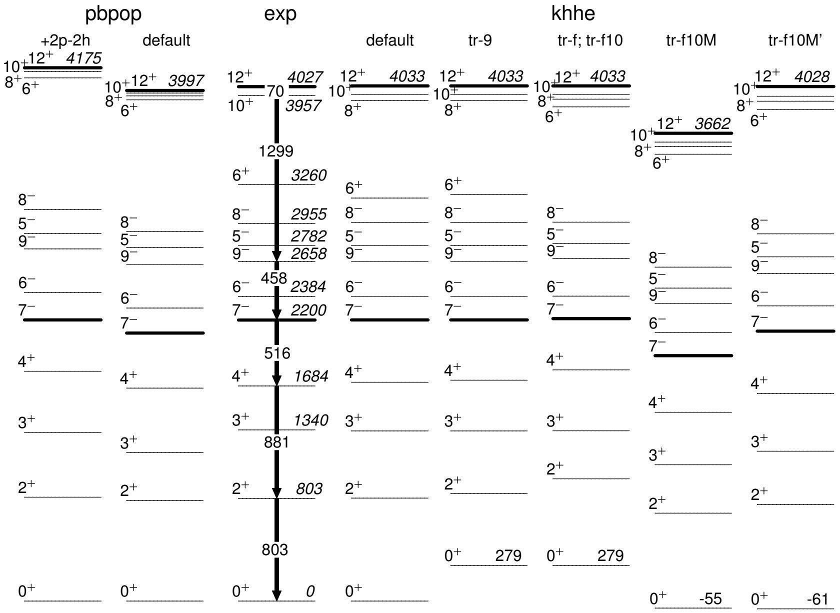

Figure 12. Comparison between evaluated ('exp') [34] and predicted ('pbpop', 'khhe') decay schemes of ^{206}Pb starting from the 12^{+} isomer. Isomeric states are indicated by thick horizontal lines. All states are labelled with spin and parity, selected ones also with their excitation energy in keV. The main experimental γ-ray cascade is included for reference. Both 'pbpop' and the 'khhe default' calculations are normalized to the 0^{+} ground state, the other 'khhe' schemes are presented relative to the 'default' ground state.

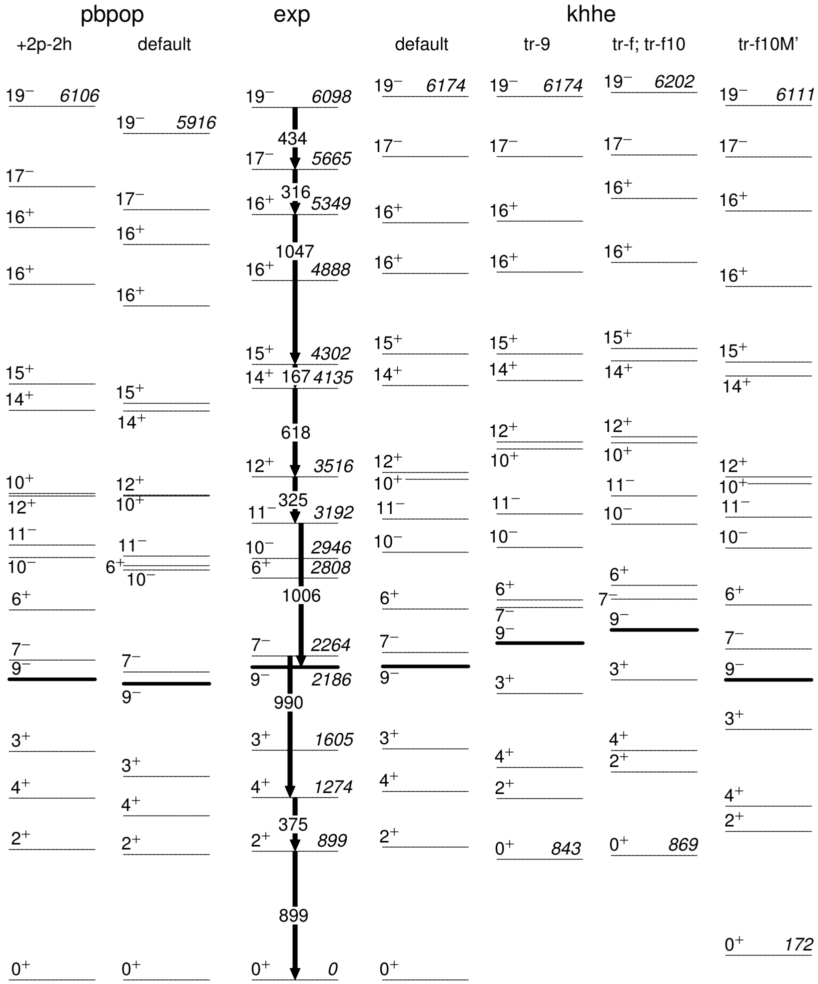

Figure 13. Comparison between evaluated ('exp') [60] and predicted ('pbpop', 'khhe') decay schemes of ^{204}Pb starting from the 19^- isomer. Isomeric states are indicated by thick horizontal lines. All states are labelled with spin and parity, selected ones also with their excitation energy in keV. The main experimental γ-ray cascade is included for reference. Both 'pbpop' and the 'khhe default' calculations are normalized to the 0^+ ground state, the other 'khhe' schemes are presented relative to the 'default' ground state.

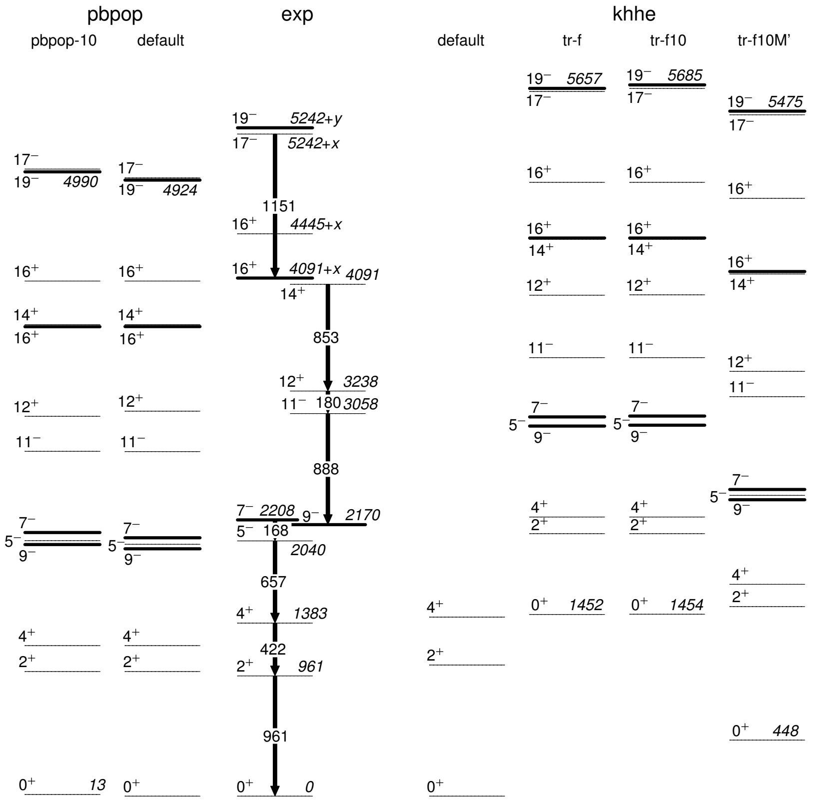

Figure 14. Comparison between evaluated ('exp') [40] and predicted ('pbpop', 'khhe') decay schemes of ^{202}Pb starting from the 19^- isomer. Isomeric states are indicated by thick horizontal lines. All states are labelled with spin and parity, selected ones also with their excitation energy in keV. The main experimental γ-ray cascade is included for reference. The two 'default' calculations are normalized to the 0^+ ground state, the other schemes are presented relative to their respective 'default' ground state.

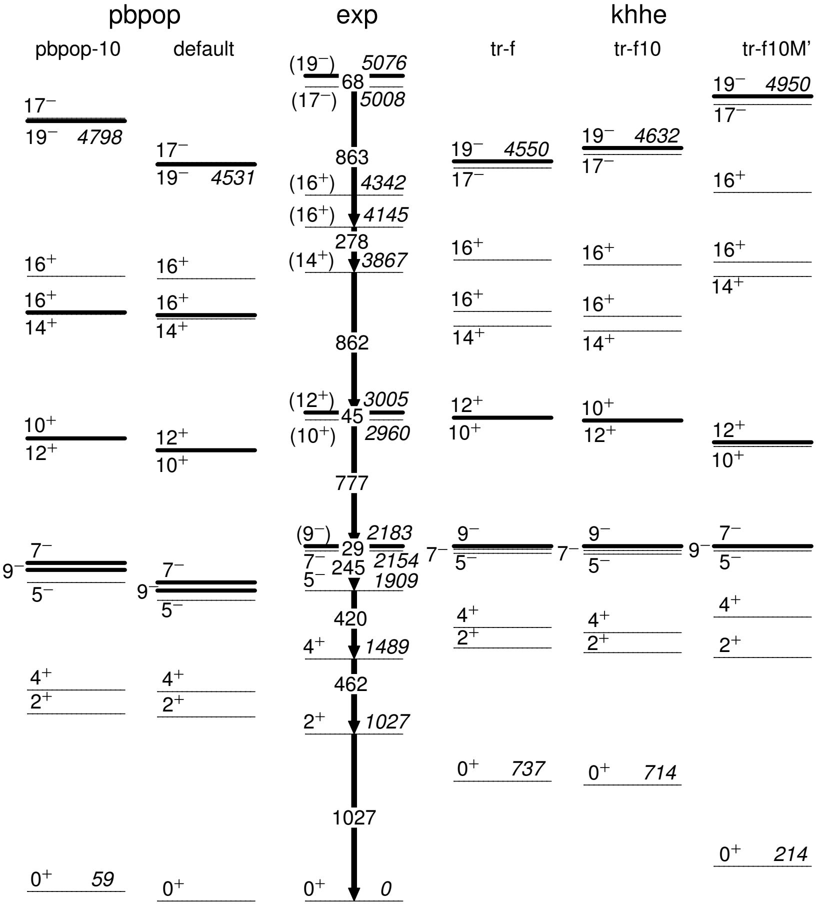

Figure 15. Comparison between evaluated ('exp') [44] and predicted ('pbpop', 'khhe') decay schemes of ^{200}Pb starting from the 19^- isomer. Isomeric states are indicated by thick horizontal lines. All states are labelled with spin and parity, selected ones also with their excitation energy in keV. The main experimental γ-ray cascade is included for reference. The 'pbpop default' calculation is normalized to the 0^+ ground state, 'pbpop-10' is presented relative to that. All 'khhe' decay schemes are normalized to the experimental 9^- isomer.

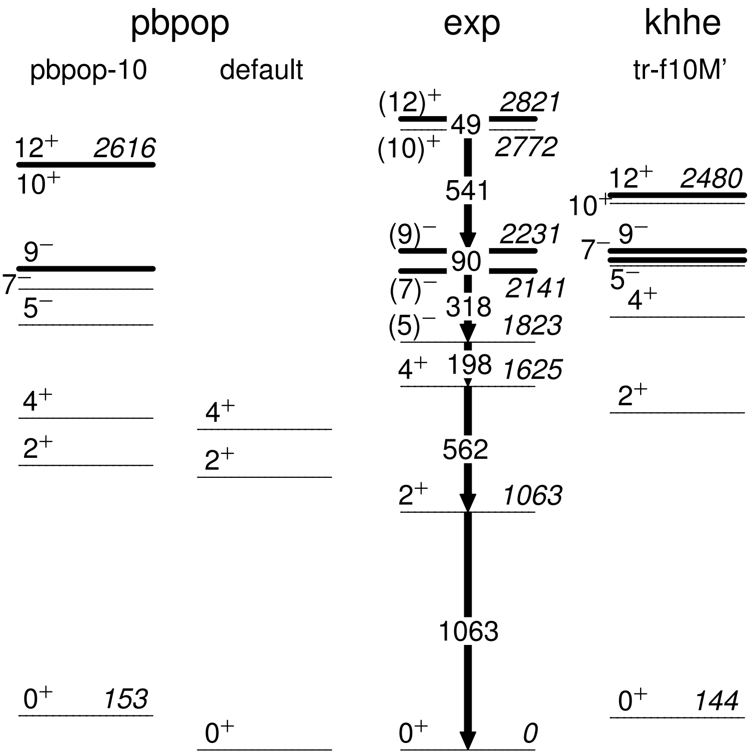

Figure 16. Comparison between evaluated ('exp') [45] and predicted ('pbpop', 'khhe') decay schemes of ^{198}Pb starting from the $(12)^+$ isomer. Isomeric states are indicated by thick horizontal lines. All states are labelled with spin and parity, selected ones also with their excitation energy in keV. The main experimental γ-ray cascade is included for reference. The 'pbpop default' calculation is normalized to the 0^+ ground state, 'pbpop-10' is presented relative to that, and the 'khhe tr-f10M" decay scheme is normalized to the experimental $(9)^-$ isomer.

Tables and table captions

Table 1. Summary of quantities relevant for the observed isomeric states. Isotope, spin and parity, I^π, half-live values, $T_{1/2}$, from the present analysis and adopted, associated γ rays, E_γ, and isomeric ratios, R_{exp}, are listed. For the corresponding decay schemes, see Figs. 2, 4, 6, 8, and 10.

	I^π ($\hbar$)	$T_{1/2}$ present	$T_{1/2}$ adopted	E_γ (keV)	R_{exp} (%)
^{206}Hg	10^+	106(15) ns	108(6) ns	1257	4.4(6)
				1157	3.2(3)
				364	3.5(4)
				weighted average:	3.5(2)
^{206}Hg	5^-	2.08(4) μs	2.09(3) μs	1034	34.2(18)
				1068	32.4(18)
				weighted average:	29.7(13)[a]
^{206}Pb	12^+	203(28) ns	202(3) ns	1369	1.3(3)
				1299	1.2(3)
				458	1.5(3)
				weighted average:	1.3(2)
^{206}Pb	7^-		125(2) μs	516	21.0(27)
				881	26.4(32)
				537	21.9(71)
				803	24.9(27)
				weighted average:	22.4(16)[b]
^{202}Pb	19^-	105(48) ns	107(4) ns	1160	0.6(4)
				797	1.0(4)
				1151	0.5(1)
				weighted average:	0.5(1)
^{202}Pb	16^+	103(10) ns	109(6) ns	853	2.6(3)
				831	3.6(20)
				785	2.6(9)
				weighted average:	2.2(3)[C]
^{202}Pb	7^-	64.5(3) ns	65.3(3) ns	657	9.5(13)
				422	8.3(11)
				961	9.3(12)
				weighted average:	9.0(7)
^{200}Pb	(19^-)	87(18) ns	72(4) ns	666	0.6(5)
				862[d]	0.8(2)
				weighted average:	0.8(2)
^{200}Pb	(12^+)	195(8) ns	199(4) ns	777	14.2(7)
				weighted average:	13.4(8)[c]

	I^{π} ($\hbar$)	$T_{1/2}$ present	adopted	E_{γ} (keV)	R_{exp} (%)
^{200}Pb	(9^-)	476(10) ns	482(11) ns	245	35.7(16)
				420	33.9(15)
				462	32.0(14)
				1027	31.0(14)
				weighted average:	19.5(10)[b]
^{198}Pb	(12^+)	212(10) ns	212(5) ns	541	18.5(10)
^{198}Pb	(7^-)	4.05(10) μs	4.12(10) μs	318	45.4(21)
				562	44.9(21)
				1063	45.0(20)
				weighted average:	26.6(16)[b]

[a] Corrected for feeding from the $I^{\pi} = 10^+$ state.

[b] Corrected for feeding from the $I^{\pi} = 12^+$ state.

[c] Corrected for feeding from the $I^{\pi} = 19^-$ state.

[d] Corresponds to 862/863-keV doublet [44].

Table 2. Experimental (exp) and calculated (khhe; pbpop) reduced transition strengths, $B(E2; 2^+ \rightarrow 0^+)$ (e^2fm^4), for ^{206}Pb and ^{204}Pb.

	exp	khhe				pbpop	
	[34, 60]	default	tr-9	tr-f10	tr-f10M	default	+2p-2h
^{206}Pb	204(6)	57	55	50	50	65	168
^{204}Pb	335(4)	91	61	50	55	84	222

Printed by Media-Tryck, Lund 2017 NORDIC ECOLABEL, 3041 0903

LUND
UNIVERSITY

Faculty of Science
Department of Physics

ISBN 978-91-7753-287-3
LUNFD6 / (NFFR - 1040) / 1 - 85 (2017)